Parameter Identification for Dispersive Dielectrics Using Pulsed Microwave Interrogating Signals and Acoustic Wave Induced Reflections in Two and Three Dimensions

H. T. Banks[†] and V. A. Bokil[‡]

Center for Research in Scientific Computation
North Carolina State University
Raleigh, N.C. 27695-8205

July 2004

[†]email: htbanks@ncsu.edu
[‡]email: vabokil@ncsu.edu

1. REPORT DATE **JUL 2004**	2. REPORT TYPE	3. DATES COVERED **00-00-2004 to 00-00-2004**

4. TITLE AND SUBTITLE **Parameter Identification for Dispersive Dielectrics Using Pulsed microwave Interrogating Signals and Acoustic Wave Induced Reflections in Two and Three Dimensions**		5a. CONTRACT NUMBER
		5b. GRANT NUMBER
		5c. PROGRAM ELEMENT NUMBER
6. AUTHOR(S)		5d. PROJECT NUMBER
		5e. TASK NUMBER
		5f. WORK UNIT NUMBER
7. PERFORMING ORGANIZATION NAME(S) AND ADDRESS(ES) **North Carolina State University,Center for Research in Scientific Computation,Raleigh,NC,27695-8205**		8. PERFORMING ORGANIZATION REPORT NUMBER
9. SPONSORING/MONITORING AGENCY NAME(S) AND ADDRESS(ES)		10. SPONSOR/MONITOR'S ACRONYM(S)
		11. SPONSOR/MONITOR'S REPORT NUMBER(S)

12. DISTRIBUTION/AVAILABILITY STATEMENT **Approved for public release; distribution unlimited**

13. SUPPLEMENTARY NOTES

14. ABSTRACT **see report**

15. SUBJECT TERMS

16. SECURITY CLASSIFICATION OF:			17. LIMITATION OF ABSTRACT	18. NUMBER OF PAGES **120**	19a. NAME OF RESPONSIBLE PERSON
a. REPORT **unclassified**	b. ABSTRACT **unclassified**	c. THIS PAGE **unclassified**			

Abstract

In this report we consider an electromagnetic interrogation technique for identifying the dielectric parameters of a Debye medium in two and three dimensions. These parameters include the dielectric permittivity, the conductivity and the relaxation time of the Debye medium. In this technique a travelling acoustic pressure wave that is generated in the Debye medium is used as a virtual reflector for an interrogating microwave electromagnetic pulse that is generated in free space and impinges on a planar interface that separates air and the Debye medium. The reflections of the microwave pulse from the air-Debye interface and from the acoustic pressure wave are recorded at an antenna that is located in air. These reflections comprise the data that is used in an inverse problem to estimate the dielectric parameters of the Debye medium. We assume that the dielectric parameters of the Debye medium are locally pressure dependent. A model for acoustic pressure dependence of the material constitutive parameters in Maxwell's equations is presented. As a first approximation, we assume that the Debye dielectric parameters are affine functions of pressure. We present a time domain formulation that is solved using finite differences in time and in space using the finite difference time domain method (FDTD). Perfectly matched layer (PML) absorbing boundary conditions are used to absorb outgoing waves at the finite boundaries of the computational domain and prevent excessive spurious reflections from reentering the domain and contaminating the data that is collected at the antenna placed in air.

Using the method of least squares for the parameter identification problem we solve an inverse problem by using two different algorithms; the gradient based Levenberg-Marquardt method, and the gradient free, simplex based Nelder-Mead method. We solve inverse problems to construct estimates for two or more dielectric parameters. Finally we use statistical error analysis to construct confidence intervals for all the presented estimates. These confidence intervals are a probabilistic statement about the procedure that we have used to construct estimates of the various parameters. Thus we naturally combine the deterministic nature of our problem with uncertainty aspects of estimates.

1 Introduction

The study of transient electromagetic waves in lossy dispersive dielectrics is of great interest due to the numerous applications of this subject to many different problems [AMP94, APM89]. These include microwave imaging for medical applications in which one seeks to investigate the internal structure of an object (the human body) by means of electromagnetic fields at microwave frequencies (300 MHz - 30 GHz). This is done for example, to detect cancer or other anomalies by studying changes in the electrical properties of tissues [FMS03]. These include the dielectric properties such as permittivity, the conductivity and the relaxation time for the Debye medium. One generates the electrical property distributions in the body (*Microwave maps*) with the hope that such properties of different bodily tissues are related to their physiological state. With such noninvasive interrogating techniques one can study properties and defects in biological tissues with very little discomfort to the subjects. Other potential applications for such interrogation techniques are nondestructive damage detection in aircraft and spacecraft where very high frequency electromagnetic pulses can be used to detect the location and width of any cracks that may be present [BGW03]. Additional applications are found in mine, ordinance and camouflage surveillance, and subsurface and atmospheric environmental modeling [BBL00].

Another important technique employed in noninvasive interrogation of objects is the use of ultrasonic waves in industrial and medical applications. The interaction of electromagnetic and sound waves in matter has been widely studied in acoustooptics [And67, Kor97]. Brillouin first showed that electromagnetic and sound waves can interact in a medium and influence each others propagation dynamics [Bri60]. The response of the atomic electrons in a material medium to the applied electric field results in a polarization of the material with a resulting index of refraction that is a function of the density in the material. Consequently, the material density fluctuations produced by a sound wave induce perturbations in the index of refraction. Thus an electromagnetic wave transmitted through the medium will be modulated by the sound wave, and scattering and reflection will occur. Conversely, a spatial variation of the electromagnetic field intensity and the corresponding electromagnetic stress lead to a volume force distribution in the medium. This is called electrostriction, and can lead to sound generation. This mutual interaction between light and sound may also lead to instabilities and wave amplification [MI68].

The work in this paper is based on ideas underlying the techniques formulated in [BBL00] and [ABR02]. In [BBL00], the authors present an electromagnetic interrogation technique for general dispersive media backed by either a perfect conducting wall to reflect the electromagnetic waves, or by using standing acoustic waves as *virtual reflectors*. In [ABR02], this work was extended to using travelling waves as acoustic reflectors. In both cases the techniques were demonstrated in one dimension by assuming plane electromagnetic waves impinging at normal incidence on slabs of dispersive media. In [BB03] a multidimensional version of the electromagnetic in-

terrogation problem is presented for dispersive media backed by perfect conductor walls and the FDTD method is utilized [Taf95, Taf98]. However, as we have noted above, the object of interrogation may not be backed by perfect conductor walls in many important applications, and hence one needs to have another type of accessible interface which will reflect the propagating electromagnetic pulses. It is therefore of great importance to ascertain (computationally and experimentally) whether the interrogation ideas of [ABR02] using acoustic pressure waves as virtual reflectors can be effective in multidimensional settings. The goal of this paper is the investigation of computational and statistical aspects of this methodology. At present we are also trying to validate these proposed techniques by testing the ideas in this paper in an experimental setup. Our group has built an antenna that we are using to study the acoustooptical interaction in agar-agar in which the sound waves are produced by means of a transducer [ABK04]. In such a setup, as well as in many applications one cannot assume normally incident plane waves impinging on the agar, and hence one needs to consider the more general case of oblique incidence. This motivates the study of an electromagnetic interrogation technique using the acoustooptical interaction to study dielectic properties of dispersive media in multidimensions.

We begin with Maxwell's equations for a first order dispersive (Debye) media with Ohmic conductivity and incorporate a model that describes the electromagnetic/acoustic interaction. Our model features modulation of the material polarization by the pressure wave and thus the behaviour of the electromagnetic pulse. This approach is based on ideas found in [MI68]. We incorporate a pressure dependent Debye model for orientational polarization into Maxwell's equations. We model the propagation of a non-harmonic pulse from a finite antenna source in free space impinging obliquely on a planar interface into the Debye medium. We use the finite difference time domain method (FDTD) [Taf95] to discretize Maxwell's equations and to compute the components of the electric field in the case where the signal and the dielectric parameters are independent of the y variable. Figure 1 depicts the antenna and the Debye dielectric slab geometry that we will model in our problem with the infinite dielectric slab perpendicular to the z-axis and uniform in the y-direction and finite in the x-direction lying in the region $-\infty \leq y \leq \infty, x_1 \leq x \leq x_2$. An alternating current along the x-direction of the antenna located at $z = z_c$ then produces an electric field that is uniform in y with nontrivial components E_x and E_z depending on (t, x, z). When propagated in the xz-plane, this results in oblique incident waves on the dielectric surface in the xy-plane at $z = z_1$. (In [BF95] the authors use Fourier-series in the frequency domain to compute the propagation of a time harmonic pulse train of plane waves that enter a dielectric across a planar boundary at oblique incidence. They showed that precursors are excited by short rise time pulses at oblique incidence. However, the use of Fourier series restricts this approach to harmonic pulses.) The oblique waves impinge on the planar interface that separates air and the Debye medium at $z = z_1$ where they undergo partial transmission and partial reflection. A reflected wave travels back to the antenna at

4

$z = z_c$ and is recorded. The transmitted part of the wave travels through the Debye medium and intercepts an acoustic pressure wave that is generated in the dielectric medium. Here the microwave pulse undergoes partial transmission and reflection. The reflected wave travels back through the Debye medium, undergoes a secondary reflection/transmission at the air-Debye interface and is then recorded at the antenna. Thus the antenna records three pieces of information; the input source, the reflection of the electromagnetic pulse from the air-Debye interface and the reflection from the pressure wave region. This data is recorded at the center of the antenna and will be used in an inverse problem to estimate the dielectric properties of the Debye medium. We note that the acoustic wave speed is many orders of magnitude smaller than the speed of light. Thus the acoustic pressure wave is almost stationary relative to the microwave pulse. In this report, we have assumed that the acoustic pressure wave is specified *a priori* and hence we assume that the pressure wave is not modified by the electromagnetic wave. This leads to a much simplified electromagnetic/acoustic interaction model. The dynamic interaction between the two and the appropriateness of this simplifying assumption are currently being investigated and will be the topic of a future report.

An important computational issue in modeling two or three dimensional wave propagation is the construction of a finite computational domain and appropriate boundary conditions for terminating this domain in order to numerically simulate an essentially unbounded domain problem. We surround the domain of interest by perfectly matched absorbing layers (PML's), thus producing a finite computational domain. The original PML formulation is due to J. P. Berenger [Ber94] and was based on a split form of Maxwell's equations in which all the fields themselves were split into orthogonal subcomponents. This formulation was appropriately called the split field form. Many different variations of the split field PML are now available in the literature. Most of these different formulations, though equivalent to the split field PML, do not involve the splitting of the fields or splitting of Maxwell's equations. The PML formulation that we use in this report is based on the anisotropic (uniaxial) formulation that was first proposed by Sacks *et. al.* [SKLL95].

We first present numerical results for the forward problem for two different test cases. The relaxation times of the Debye media in these two test cases differ by many orders of magnitude. We perform a sensitivity analysis in each test case to determine which parameters are most likely to be accurately estimated in an inverse problem. We also determine which of the pressure dependent parameters are the most significant in each of the test cases. As we shall see, the significant difference in the orders of magnitude of the relaxation times for the two test cases produces inverse problems with very different estimation properties.

We next discuss a parameter estimation problem in which we estimate model parameters for the two different Debye media from simulated data. We formulate our inverse problem using the method of least squares. We compare two different algorithms in solving the parameter estimation problems; the Levenberg-Marquardt

method, which is a gradient based algorithm, and the Nelder-Mead method, which is based on simplices and is gradient free. For the first test case, these two algorithms produce similar results. However, in the second test case, we see the presence of many local minima and the Nelder-Mead algorithm converges to a local minima instead of the global minimum.

We also consider uncertainty in estimates due to data uncertainty. We present a model for generating noisy data that we use in our inverse problems to simulate experimental settings in which noise enters into the problem in a natural fashion. We then discuss a statistical error methodology to analyze the results of the inverse problems based on noisy data. This statistical error analysis is used to obtain confidence intervals for all the parameters estimated in the inverse problem. These intervals indicate the level of confidence that can be associated with estimates obtained with our methodology.

2 Model formulation: The forward problem

We consider Maxwell's equations which govern the electric field $\mathbf{E}$ and the magnetic field $\mathbf{H}$ in a domain Ω with charge density ρ. Thus we consider the system

$$
\begin{cases}
\text{(i)} & \dfrac{\partial \mathbf{D}}{\partial t} + \mathbf{J} - \nabla \times \mathbf{H} = 0, \ \text{in } (0,T) \times \Omega, \\[2mm]
\text{(ii)} & \dfrac{\partial \mathbf{B}}{\partial t} + \nabla \times \mathbf{E} = 0, \ \text{in } (0,T) \times \Omega, \\[2mm]
\text{(iii)} & \nabla \cdot \mathbf{D} = \rho, \ \text{in } (0,T) \times \Omega, \\[2mm]
\text{(iv)} & \nabla \cdot \mathbf{B} = 0, \ \text{in } (0,T) \times \Omega, \\[2mm]
\text{(v)} & \mathbf{E} \times \mathbf{n} = 0, \ \text{on } (0,T) \times \partial\Omega, \\[2mm]
\text{(vi)} & \mathbf{E}(0,\mathbf{x}) = 0, \quad \mathbf{H}(0,\mathbf{x}) = 0, \ \text{in } \Omega.
\end{cases}
\tag{1}
$$

The fields $\mathbf{D}, \mathbf{B}$ are the electric and magnetic flux densities respectively. All the fields in (1) are functions of position $\mathbf{r} = (x,y,z)$ and time t. We have $\mathbf{J} = \mathbf{J}_c + \mathbf{J}_s$, where $\mathbf{J}_c$ is a conduction current density and $\mathbf{J}_s$ is the source current density. We assume only free space (actually the antenna in our example) can have a source current, and $\mathbf{J}_c$ is only found in the dielectric material. The condition (1, v) is a perfectly conducting boundary condition on the computational domain which we will replace with absorbing conditions in the sequel. With perfect conductor conditions, the computational boundary acts like a hard wall to impinging electromagnetic waves causing spurious reflections that would contaminate the data that we wish to use in our inverse problems.

Constitutive relations which relate the electric and magnetic fluxes $\mathbf{D}, \mathbf{B}$ and the electric current $\mathbf{J_c}$ to the electric and magnetic fields $\mathbf{E}, \mathbf{H}$ are added to these equations to make the system fully determined and to describe the response of a material to the

electromagnetic fields. In free space, these constitutive relations are $\mathbf{D} = \epsilon_0 \mathbf{E}$, and $\mathbf{B} = \mu_0 \mathbf{H}$, where ϵ_0 and μ_0 are the permittivity and the permeability of free space, respectively, and are constant [Jac99]. In general there are different possible forms for these constitutive relationships. In a frequency domain formulation of Maxwell's equations, these are usually converted to linear relationships between the dependent and independent quantities with frequency dependent coefficient parameters. We will consider the case of a dielectric in which magnetic effects are negligible, and we assume that Ohm's law governs the electric conductivity. Thus, within the dielectric medium we have constitutive relations that relate the flux densities $\mathbf{D}, \mathbf{B}$ to the electric and magnetic fields, respectively. We have

$$
\begin{cases}
\text{(i)} & \mathbf{D} = \epsilon_0 \mathbf{E} + \mathbf{P} I_D, \\
\text{(ii)} & \mathbf{B} = \mu_0 \mathbf{H}, \\
\text{(iii)} & \mathbf{J}_c = \sigma \mathbf{E} I_D,
\end{cases}
\tag{2}
$$

In (2), I_D denotes the indicator function on the Debye medium. Thus, $\mathbf{J}_c = 0$ in air. The quantity $\mathbf{P}$ is called the electric polarization. It is equal to zero in air and is nonzero in the dielectric. Electric polarization may be defined as the electric field induced disturbance of the charge distribution in a region. This polarization may have an instantaneous component as well as ones that do not occur instantaneously; the latter usually have associated time constants called the relaxation times which are denoted by τ. We let the instantaneous component of the polarization to be related to the electric field by means of a dielectric constant $\epsilon_0 \chi$ and denote the remainder of the electric polarization as $\mathbf{P}_{\mathrm{R}}$. We have

$$
\mathbf{P} = \mathbf{P}_{\mathrm{I}} + \mathbf{P}_{\mathrm{R}} = \epsilon_0 \chi \mathbf{E} + \mathbf{P}_{\mathrm{R}},
\tag{3}
$$

and hence the constitutive law (2, i) becomes

$$
\mathbf{D} = \epsilon_0 \epsilon_r \mathbf{E} + \mathbf{P}_{\mathrm{R}},
\tag{4}
$$

where $\epsilon_r = (1 + \chi)$ is the relative permittivity of the dielectric medium.

To describe the behaviour of the media's macroscopic electric polarization $\mathbf{P}_{\mathrm{R}}$, we employ a general integral equation model in which the polarization explicitly depends on the past history of the electric field. This model is sufficiently general to include microscopic polarization mechanisms such as dipole or orientational polarization(Debye), as well as ionic and electronic polarization(Lorentz), and other frequency dependent polarization mechanisms [And67] as well as multiples of such mechanisms represented by a distribution of the associated time constants (e.g., see [BG04]). The resulting constitutive law can be given in terms of a polarization or displacement susceptibility kernel g as

$$
\mathbf{P}_{\mathrm{R}}(t, x, z) = \int_0^t g(t - s, x, z) \mathbf{E}(s, x, z) ds,
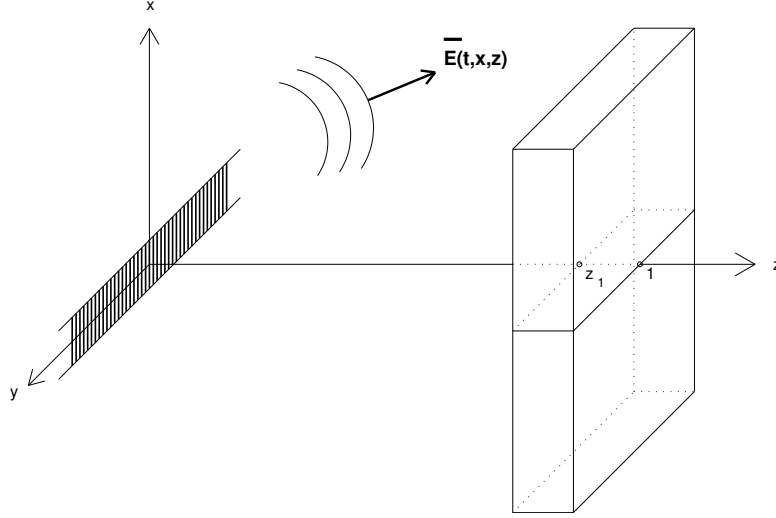\tag{5}
$$

Figure 1: Antenna and dielectric slab configuration.

which, in the case (Debye) of interest to us here, can be written as

$$g(t) = \mathrm{e}^{-t/\tau} \frac{\epsilon_0 (\epsilon_s - \epsilon_\infty)}{\tau}. \tag{6}$$

Such a Debye model can be represented in differential form as

$$\tau \dot{\mathbf{P}}_\mathrm{R} + \mathbf{P}_\mathrm{R} = \epsilon_0 (\epsilon_s - \epsilon_\infty) \mathbf{E},$$
$$\mathbf{D} = \epsilon_0 \epsilon_\infty \mathbf{E} + \mathbf{P}_\mathrm{R}, \tag{7}$$

inside the dielectric, whereas $\mathbf{P}_\mathrm{R} = 0$, $\epsilon_\infty = 1$ in air, and $\epsilon_\infty = \epsilon_r$ in the dielectric. We will henceforth denote $\mathbf{P}_\mathrm{R}$ by $\mathbf{P}$. In equations (5) and (7), the parameters ϵ_s and ϵ_∞ denote the static relative permittivity, and the value of permittivity for an extremely high($\approx \infty$) frequency field, respectively. The quantity ϵ_∞ is called the infinite frequency permittivity. Biological cells and tissues display very high values of the dielectric constants at low frequencies, and these values decrease in almost distinct steps as the excitation frequency is increased. This frequency dependence of permittivity is called dielectric dispersion and permits identification and investigation of a number of completely different underlying mechanisms. This property of dielectric materials makes the problem of parameter identification an important as well as very useful topic for investigation.

We will modify system (1) and the constitutive laws (2) by performing a change of variables that renders the system in a form that is convenient for analysis and computation. From (1, i) we have

$$\frac{\partial}{\partial t} \left(\mathbf{D} + \int_0^t \mathbf{J}_c(s, \mathbf{x}) \, \mathrm{d}s \right) - \nabla \times \mathbf{H} = -\mathbf{J}_s, \text{ in } (0, T) \times \Omega. \tag{8}$$

8

Next, we define the new variable

$$\widetilde{\mathbf{D}}(t, \mathbf{x}) = \mathbf{D}(t, \mathbf{x}) + \int_0^t \mathbf{J}_c(s, \mathbf{x}) \, \mathrm{ds}. \tag{9}$$

Using definition (9) in (8) and (1) we obtain the modified system

$$\begin{cases} \text{(i)} & \dfrac{\partial \widetilde{\mathbf{D}}}{\partial t} - \nabla \times \mathbf{H} = -\mathbf{J}_s \text{ in } (0, T) \times \Omega, \\[2mm] \text{(ii)} & \dfrac{\partial \mathbf{B}}{\partial t} + \nabla \times \mathbf{E} = 0 \text{ in } (0, T) \times \Omega, \\[2mm] \text{(iii)} & \nabla \cdot \widetilde{\mathbf{D}} = 0 \text{ in } (0, T) \times \Omega, \\[2mm] \text{(iv)} & \nabla \cdot \mathbf{B} = 0 \text{ in } (0, T) \times \Omega, \\[2mm] \text{(v)} & \mathbf{E} \times \mathbf{n} = 0 \text{ on } (0, T) \times \partial\Omega, \\[2mm] \text{(vi)} & \mathbf{E}(0, \mathbf{x}) = \mathbf{0}, \ \mathbf{H}(0, \mathbf{x}) = \mathbf{0} \text{ in } \Omega. \end{cases} \tag{10}$$

We will henceforth drop the ˜ symbol on $\mathbf{D}$. We note that equation (10, iii) follows from the continuity equation $\frac{\partial \rho}{\partial t} + \nabla \cdot \mathbf{J} = 0$, the assumption that $\rho(0) = 0$, and the assumption that $\nabla \cdot \mathbf{J}_s = 0$ (in the sense of distributions). The modified constitutive laws (2) after substitution of Ohm's law and (9) are

$$\begin{cases} \text{(i)} & \mathbf{D}(t, \mathbf{x}) = \epsilon_0 \epsilon_\infty(\mathbf{x}) \mathbf{E}(t, \mathbf{x}) + \mathbf{P}_{\mathrm{R}} + \int_0^t \sigma(\mathbf{x}) \mathbf{E}(s, \mathbf{x}) \, \mathrm{ds}, \\[2mm] \text{(ii)} & \mathbf{B} = \mu_0 \mathbf{H}, \end{cases} \tag{11}$$

with $\mathbf{P}_{\mathrm{R}}$, the solution of

$$\tau \dot{\mathbf{P}}_{\mathrm{R}} + \mathbf{P}_{\mathrm{R}} = \epsilon_0 (\epsilon_s - \epsilon_\infty) \mathbf{E}. \tag{12}$$

3 An anisotropic perfectly matched layer absorbing medium

In one dimension exact absorbing boundary conditions can be constructed for terminating a computational domain. In two and three dimensions, however, there are no exact absorbing boundary conditions available. In such a case we can either use approximate absorbing boundary conditions of some finite order (usually one or two), or we can surround our computational domain by absorbing layers. In this report we use the second approach and construct perfectly matched layers [Ber94] surrounding the domain of interest. These layers have been demonstrated to have many orders of magnitude better absorbing capabilities than the approximate absorbing boundary conditions [Taf98]. In this section we will first construct PML's that can be matched

to free space and then we will explain how this construction can be generalized to the case of a Debye medium.

The source current $\mathbf{J}_s$ is zero inside the PML regions. So we will neglect $\mathbf{J}_s$ in this section. We model the PMLs as lossy regions by adding artificial loss terms to Maxwell's equations. This approach is based on using anisotropic material properties to describe the absorbing layer [SKLL95, Ged96, Rap95]. We start with Maxwell's equations in the most general form

$$\begin{cases} \dfrac{\partial \mathbf{D}}{\partial t} = \nabla \times \mathbf{H} - \mathbf{J}_e, \\[2mm] \dfrac{\partial \mathbf{B}}{\partial t} = -\nabla \times \mathbf{E} - \mathbf{J}_m, \\[2mm] \nabla \cdot \mathbf{D} = 0, \\[2mm] \nabla \cdot \mathbf{B} = 0, \end{cases} \tag{13}$$

where $\mathbf{J}_e$ and $\mathbf{J}_m$ are electric and magnetic conductivities, respectively. Inside the computational domain we will have $\mathbf{J}_e = \mathbf{J}_c$ and $\mathbf{J}_m = 0$. We will derive a PML model in the frequency domain and then transform the corresponding equations to the time domain by taking the inverse Fourier transforms of the frequency domain equations. To this end, we consider the time-harmonic form of Maxwell's equations (13) given by

$$\begin{cases} \mathrm{j}\omega\hat{\mathbf{D}} = \nabla \times \hat{\mathbf{H}} - \hat{\mathbf{J}}_e, \\[2mm] \mathrm{j}\omega\hat{\mathbf{B}} = -\nabla \times \hat{\mathbf{E}} - \hat{\mathbf{J}}_m, \\[2mm] \nabla \cdot \hat{\mathbf{B}} = 0, \\[2mm] \nabla \cdot \hat{\mathbf{D}} = 0, \end{cases} \tag{14}$$

where for every field vector $\mathbf{V}$, $\hat{\mathbf{V}}$ denotes its Fourier transform. We then have the constitutive laws

$$\begin{cases} \hat{\mathbf{B}} = [\mu]\hat{\mathbf{H}}, \\[2mm] \hat{\mathbf{D}} = [\epsilon]\hat{\mathbf{E}}, \\[2mm] \hat{\mathbf{J}}_m = [\sigma_M]\hat{\mathbf{H}}, \\[2mm] \hat{\mathbf{J}}_e = [\sigma_E]\hat{\mathbf{E}}. \end{cases} \tag{15}$$

In (15) the square brackets indicate a tensor quantity. Thus we allow for anisotropy in our media by permitting the material parameters to be tensors. Note that when the density of electric and magnetic charge carriers in the medium is uniform throughout space, then $\nabla \cdot \hat{\mathbf{J}}_e = 0$ and $\nabla \cdot \hat{\mathbf{J}}_m = 0$. We define the new tensors

$$\begin{cases} [\bar{\mu}] = [\mu] + \dfrac{[\sigma_M]}{\mathrm{j}\omega}, \\[3mm] [\bar{\epsilon}] = [\epsilon] + \dfrac{[\sigma_E]}{\mathrm{j}\omega}. \end{cases} \tag{16}$$

Using the definitions (16) we define two new constitutive laws that are equivalent to (15), given by

$$
\begin{cases}
\hat{\mathbf{B}}_{\text{new}} = [\bar{\mu}]\hat{\mathbf{H}}, \\[2mm]
\hat{\mathbf{D}}_{\text{new}} = [\bar{\epsilon}]\hat{\mathbf{E}}.
\end{cases} \tag{17}
$$

Using (17) in (14), we can write Maxwell's equations in time-harmonic form as

$$
\begin{cases}
\mathrm{j}\omega\hat{\mathbf{D}}_{\text{new}} = \nabla\times\hat{\mathbf{H}}, \\[2mm]
\mathrm{j}\omega\hat{\mathbf{B}}_{\text{new}} = -\nabla\times\hat{\mathbf{E}}, \\[2mm]
\nabla\cdot\hat{\mathbf{D}}_{\text{new}} = 0, \\[2mm]
\nabla\cdot\hat{\mathbf{B}}_{\text{new}} = 0.
\end{cases} \tag{18}
$$

The split-field PML introduced by Berenger [Ber94] is a hypothetical medium based on a mathematical model. In [MP95] Mittra and Pekel showed that Berenger's PML was equivalent to Maxwell's equations with a diagonally anisotropic tensor appearing in the constitutive relations for **D** and **B**. For a single interface, the anisotropic medium is *uniaxial* and is composed of both the electric and magnetic permittivity tensors. This uniaxial PML (UPML) formulation performs as well as the original split-field PML while avoiding the nonphysical field splitting. As will be shown below, by properly defining a general constitutive tensor $[S]$, we can use the UPML in the interior working volume as well as the absorbing layer. This tensor provides a lossless isotropic medium in the primary computation zone, and individual UPML absorbers adjacent to the outer lattice boundary planes for mitigation of spurious wave reflections. The fields excited within the UPML are also plane wave in nature and satisfy Maxwell's curl equations. The derivation of the PML properties of the tensor constitutive laws is also done directly by Sacks *et al.* in [SKLL95] and by Gedney in [Ged96]. We follow the derivation by Sacks *et al.* here. We begin by considering planar electromagnetic waves in free space incident upon a PML half space. Starting with the impedance matching assumption, i.e., the impedance of the layer must match that of free space: $\epsilon_0^{-1}\mu_0 = [\bar{\epsilon}]^{-1}[\bar{\mu}]$ we have

$$
\frac{[\bar{\epsilon}]}{\epsilon_0} = \frac{[\bar{\mu}]}{\mu_0} = [S] = \mathrm{diag}\{a_1, a_1, a_3\}. \tag{19}
$$

Hence, the constitutive parameters inside the PML layer are $[\bar{\epsilon}] = \epsilon_0[S]$ and $[\bar{\mu}] = \mu_0[S]$, where $[S]$ is a diagonal tensor. We next consider plane wave solutions of the form

$$
\mathbf{V}(\mathbf{x}, t) = \hat{\mathbf{V}}(\mathbf{x})\exp(\mathrm{j}(\omega t - \mathbf{k}\cdot\mathbf{x})), \tag{20}
$$

for all field vectors **V**, to the time-harmonic Maxwell's equations with the diagonally anisotropic tensor, where $\mathbf{k} = (k_x, k_y, k_z)$ is the wave vector of the planar electromagnetic wave and $\mathbf{x} = (x, y, z)$. The dispersion relation for waves in the PML are found

11

to be

$$\frac{k_x^2}{a_2 a_3} + \frac{k_y^2}{a_1 a_3} + \frac{k_z^2}{a_1 a_2} = k_0^2 \equiv \omega^2 \mu_0 \epsilon_0 \equiv \frac{\omega^2}{c_0^2}. \tag{21}$$

where, c_0 is the speed of light in free space.

To further explain our UPML formulation, we may, without loss of generality, consider a PML layer which fills the positive x half-space and plane waves with wave vectors in the xz- plane ($k_y = 0$). Let θ_i be the angle of incidence of the plane wave measured from the normal to the surface $x = 0$. The standard phase and magnitude matching arguments at the interface yield the following generalization of Snell's law

$$\sqrt{a_1 a_3} \sin \theta_t = \sin \theta_i, \tag{22}$$

where θ_t is the angle of the transmitted plane wave. Matching the magnitudes of the electric and magnetic fields at the interface, $x = 0$, we obtain the following values of the reflection coefficients for the TE and the TM modes

$$\begin{cases} R^{TE} = \dfrac{\cos \theta_i - \sqrt{\dfrac{a_3}{a_2}} \cos \theta_t}{\cos \theta_i + \sqrt{\dfrac{a_3}{a_2}} \cos \theta_t} \\[4ex] R^{TM} = \dfrac{\sqrt{\dfrac{a_3}{a_2}} \cos \theta_t - \cos \theta_i}{\cos \theta_i + \sqrt{\dfrac{a_3}{a_2}} \cos \theta_t} \end{cases} \tag{23}$$

From (23) we can see, that by choosing $a_3 = a_2 = a$ and $\sqrt{a_1 a_3} = 1$, the interface is completely reflectionless for any frequency, angle of incidence, and polarization. Using (17) and (19), we thus find the constitutive laws for the perfectly matched layer are

$$\begin{cases} \hat{\mathbf{D}}_{\text{new}} = \epsilon_0 [S] \hat{\mathbf{E}}, \\ \hat{\mathbf{B}}_{\text{new}} = \mu_0 [S] \hat{\mathbf{H}}, \end{cases} \tag{24}$$

where the tensor $[S]$ is

$$[S] = \begin{bmatrix} a^{-1} & 0 & 0 \\ 0 & a & 0 \\ 0 & 0 & a \end{bmatrix}. \tag{25}$$

The perfectly matched layer is therefore characterized by the single complex number a. Taking it to be the constant $a = \gamma - \mathrm{j}\beta$, and substituting into the dispersion relation (21), we obtain the following expression for the electric field inside of the PML

$$\hat{\mathbf{E}}(x, y, z) = \hat{\mathbf{E}}_0 \exp(-k_0 \beta \cos \theta_t x) \exp(-\mathrm{j} k_0 (\gamma \cos \theta_t x + \sin \theta_t z)) \exp(\mathrm{j}\omega t). \tag{26}$$

Hence we can see that γ determines the wavelength of the wave in the PML and for $\beta > 0$, the wave is attenuated according to the distance of travel in the x direction.

Remark 1 *To match the anisotropic PML along a planar boundary to a dispersive isotropic half-space, we will need to modify the above construction for the phasor-domain constitutive relation*

$$\hat{\mathbf{D}} = \epsilon_0 \epsilon_r(\omega) \hat{\mathbf{E}}, \tag{27}$$

where $\epsilon_r(\omega)$ is the frequency dependent relative permittivity of the Debye medium, which will be defined in a standard manner in (40) below.

3.1 Implementation of the uniaxial PML

To apply the perfectly matched layer to electromagnetic computations, we replace the half infinite layer by a layer of finite depth backed with a more conventional boundary condition, such as a perfect electric conductor (PEC). This truncation of the layer will lead to reflections generated at the PEC surface, which can propagate back through the layer to re-enter the computational region. In this case, the reflection coefficient R, is now a function of the angle of incidence θ, the depth of the PML δ, as well as the parameter a in (25). Thus, this parameter a for the PML is chosen in order for the attenuation of waves in the PML to be sufficient so that the waves striking the PEC surface are negligible in magnitude. Perfectly matched layers are then placed near each edge (or face in the 3D case) of the computational domain where a non-reflecting condition is desired. This leads to overlapping PML regions in the corners of the domain. As shown in [SKLL95], the correct form of the tensor which appears in the constitutive laws for these regions is the product

$$[S] = [S]_x [S]_y [S]_z, \tag{28}$$

where component $[S]_\alpha$ in the product (28) is responsible for attenuation in the α direction, for $\alpha = x, y, z$ (see Figure 2). All three of the component tensors in (28) are diagonal and have the forms

$$[S]_x = \begin{bmatrix} s_x^{-1} & 0 & 0 \\ 0 & s_x & 0 \\ 0 & 0 & s_x \end{bmatrix}; [S]_y = \begin{bmatrix} s_y & 0 & 0 \\ 0 & s_y^{-1} & 0 \\ 0 & 0 & s_y \end{bmatrix}; [S]_z = \begin{bmatrix} s_z & 0 & 0 \\ 0 & s_z & 0 \\ 0 & 0 & s_z^{-1} \end{bmatrix}. \tag{29}$$

In the above s_x, s_y, s_z are analogous to the complex valued parameter a encountered in the Section 3 analysis of the single PML layer. Thus, s_α governs the attenuation of the electromagnetic waves in the α direction for $\alpha = x, y, z$. When designing PML's for implementation, it is important to choose the parameters s_α so that the resulting frequency domain equations can be easily converted back into the time domain. The simplest of these [Ged96] which we employ here, is

$$s_\alpha = 1 + \frac{\sigma_\alpha}{j\omega\epsilon_0}, \quad \text{where} \quad \sigma_\alpha \geq 0, \quad \alpha = x, y, z. \tag{30}$$
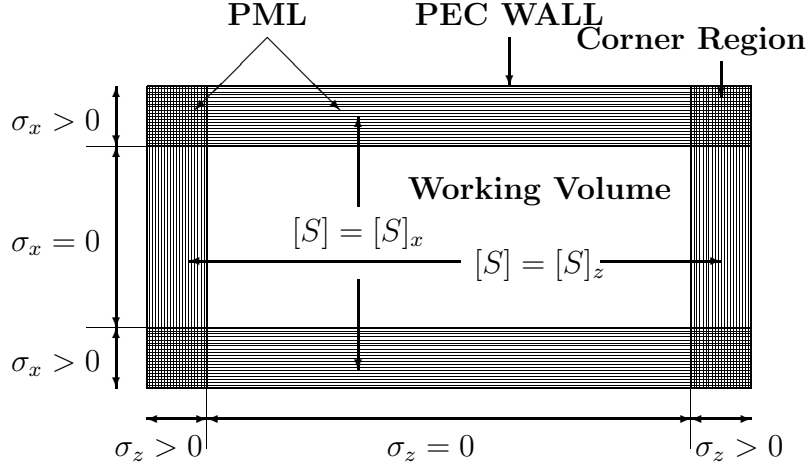
Figure 2: PML layers surrounding the domain of interest. In the corner regions of the PML, both σ_x and σ_z are positive and the tensor $[S]$ is the product $[S]_x[S]_z$. In the remaining regions only one of σ_z (left and right PML's) or σ_x (top and bottom PML's) are nonzero and positive. The tensor $[S]$, is thus either $[S]_x$ or $[S]_z$ respectively. The PML is truncated by a perfect electric conductor (PEC).

The PML interface represents a discontinuity in the conductivities σ_α. To reduce the numerical reflections caused by these discontinuous conductivities, the σ_α are chosen to be functions of the variable α (e.g., σ_x is taken to be a function of x in the $[S]_x$ component of the PML tensor). A choice of these functions so that $\sigma_\alpha = 0$, i.e., $s_\alpha = 1$ at the interface yields the PML a continuous extension of the medium being matched and reduces numerical reflections at the interface. If one increases the value of σ_α with depth in the layer, one obtains greater overall attenuation while minimizing the numerical reflections. Gedney [Ged96] suggests a conductivity profile

$$\sigma_\alpha(\alpha) = \frac{\sigma_{\max}|\alpha - \alpha_0|^m}{\delta^m}; \quad \alpha = x, y, z. \tag{31}$$

where δ is the depth of the layer, $\alpha = \alpha_0$ is the interface between the PML and the computational domain, and m is the order of the polynomial variation. Gedney remarks that values of m between 3 and 4 are believed to be optimal. For the conductivity profile (31), the PML parameters can be determined for given values of m, δ, and the desired reflection coefficient at normal incidence R_0, as

$$\sigma_{\max} \approx \frac{(m + 1)\ln(1/R_0)}{2\eta_I \delta}, \tag{32}$$

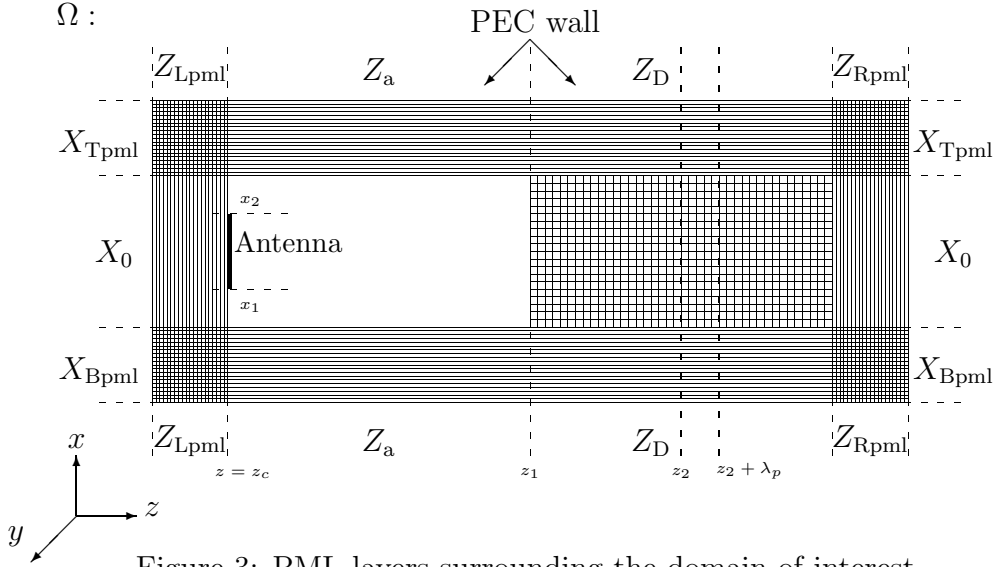η_I being the characteristic wave impedance of the PML. Emperical testing suggests

Figure 3: PML layers surrounding the domain of interest.

that, for a broad range of problems, an optimal value of σ_{max} is given by

$$\sigma_{\mathrm{opt}} \approx \frac{m+1}{150\pi\Delta_\alpha\sqrt{\epsilon_r}}, \tag{33}$$

where Δ_α is the space increment in the α direction and ϵ_r is the relative permittivity of the material being modeled. In the case of free space $\epsilon_r = 1$. Since we desire to match the PML to both free space as well as the Debye medium, we will use ϵ_r to be the average value

$$\epsilon_r = \frac{1}{2}\left(1 + \epsilon_\infty\right). \tag{34}$$

3.2   Reduction to two dimensions

From the time-harmonic Maxwell's curl equations in the PML (18) and (24), Ampere's and Faraday's laws can be written in the most general form as

$$\begin{cases} \mathrm{j}\omega\mu_0[S]\hat{\mathbf{H}} = -\nabla\times\hat{\mathbf{E}}, \ (\text{Faraday's Law}) \\ \mathrm{j}\omega[S]\hat{\mathbf{D}} = \nabla\times\hat{\mathbf{H}} - \mathbf{J}_s, \ (\text{Ampere's Law}) \end{cases} \tag{35}$$

In (35), $[S]$ is the diagonal tensor defined via (28), (29) and (30). In the presence of this diagonal tensor, a plane wave is purely transmitted into the uniaxial medium. The tensor $[S]$ is no longer uniaxial by strict definition, but rather is anisotropic. However, the anisotropic PML is still referenced as uniaxial since it is uniaxial in the nonoverlapping PML regions. Let $\Omega = X \times Z$ denote the computational domain along with the absorbing layers. We partition the interval X into disjoint closed

15

intervals as $X = X_{\mathrm{Bpml}} \cup X_0 \cup X_{\mathrm{Tpml}}$ and the interval Z into disjoint closed intervals as $Z_{\mathrm{Lpml}} \cup Z_{\mathrm{a}} \cup Z_{\mathrm{D}} \cup Z_{\mathrm{Rpml}}$, as seen in Figure 3. The computational domain of interest is the region $X_0 \times \{Z_{\mathrm{a}} \cup Z_{\mathrm{D}}\}$, where $X_0 \times Z_{\mathrm{a}}$ denotes air and $X_0 \times Z_{\mathrm{D}}$ denotes the Debye medium. The buffer region $\mathcal{D} \setminus (X_0 \times \{Z_{\mathrm{a}} \cup Z_{\mathrm{D}}\})$ contains the absorbing layers (PML's). The PML's are backed by a perfect conductor where the boundary condition $\mathbf{n} \times \mathbf{E} = 0$ is used. We construct perfectly matched layers in regions where $(x, z) \in (X_{\mathrm{Bpml}} \cup X_{\mathrm{Tpml}}) \times (Z_{\mathrm{Lpml}} \cup Z_{\mathrm{Rpml}})$. To obtain a two-dimensional model, we make the assumption that the signal and the dielectric parameters are independent of the y variable. Also, an alternating current along the x direction, as in (54), then produces an electric field that is uniform in y with nontrivial components E_x and E_z depending on (t, x, z) which, when propagated in the xz plane result in oblique incident waves on the dielectric surface in the xy plane at $z = z_c$. With these assumptions, Maxwell's equations reduces to a two dimensional system for solutions involving the E_x and E_z components for the electric field and the component H_y for the magnetic field, which is refered to as the TE_y mode. In this case, we have $\sigma_y = 0$ and $s_y = 1$ in the UPML. From (11, i) and (7) expressed in the frequency domain we have the constitutive relation

$$\hat{\mathbf{D}} = \epsilon_0 \left(\epsilon_\infty + \frac{\epsilon_s - \epsilon_\infty}{1 + \mathrm{j}\omega\tau} + \frac{\sigma}{\mathrm{j}\omega\epsilon_0} \right) \mathbf{E}. \tag{36}$$

Rescaling the electric field as

$$\hat{\tilde{E}} = \sqrt{\frac{\epsilon_0}{\mu_0}} \hat{\mathbf{E}}, \tag{37}$$

we can write the time-harmonic frequency domain Maxwell's equations (35) in the uniaxial medium as

$$
\begin{cases}
\text{(i)} \quad \mathrm{j}\omega \left(1 + \frac{\sigma_z(z)}{\mathrm{j}\omega\epsilon_0} \right) \left(1 + \frac{\sigma_x(x)}{\mathrm{j}\omega\epsilon_0} \right)^{-1} \hat{\tilde{D}}_x = -c_0 \left(\frac{\partial \hat{H}_y}{\partial z} + \mathbf{J}_s \cdot \hat{\mathbf{x}} \right), \\[2mm]
\text{(ii)} \quad \mathrm{j}\omega \left(1 + \frac{\sigma_x(x)}{\mathrm{j}\omega\epsilon_0} \right) \left(1 + \frac{\sigma_z(z)}{\mathrm{j}\omega\epsilon_0} \right)^{-1} \hat{\tilde{D}}_z = c_0 \frac{\partial \hat{H}_y}{\partial x}, \\[2mm]
\text{(iii)} \quad \mathrm{j}\omega \left(1 + \frac{\sigma_x(x)}{\mathrm{j}\omega\epsilon_0} \right) \left(1 + \frac{\sigma_z(z)}{\mathrm{j}\omega\epsilon_0} \right) \hat{H}_y = c_0 \left(\frac{\partial \hat{E}_z}{\partial x} - \frac{\partial \hat{E}_x}{\partial z} \right).
\end{cases} \tag{38}
$$

In the above $c_0 = 3.0 \times 10^8$ m/s is the speed of light in vacuum and $\hat{\tilde{\mathbf{D}}} = (\hat{\tilde{D}}_x, \hat{\tilde{D}}_z)^T$ is defined as

$$\hat{\tilde{\mathbf{D}}} = \epsilon_r^* \cdot \hat{\tilde{\mathbf{E}}}, \tag{39}$$

with

$$\epsilon_r^* = \epsilon_\infty + \frac{\epsilon_s - \epsilon_\infty}{1 + \mathrm{j}\omega\tau} + \frac{\sigma}{\mathrm{j}\omega\epsilon_0}. \tag{40}$$

To avoid a computationally intensive implementation, we define suitable constitutive relationships that facilitate the decoupling of the frequency dependent terms [Taf98].

To this end, we introduce the fields

$$
\left\{
\begin{array}{l}
\hat{D}_x^* = s_x^{-1}\hat{\tilde{D}}_x, \\[2ex]
\hat{D}_z^* = s_z^{-1}\hat{\tilde{D}}_z, \\[2ex]
\hat{H}_y^* = s_z\hat{H}_y.
\end{array}
\right.
\tag{41}
$$

Again, dropping the ˜ symbol on $\mathbf{D}$ and transforming the frequency domain equations to the time domain, we obtain the system

$$
\left\{
\begin{array}{ll}
\text{(i)} & \partial_t H_y^* + \dfrac{\sigma_x(x)}{\epsilon_0}H_y^* = c_0\left(\dfrac{\partial E_z}{\partial x} - \dfrac{\partial E_x}{\partial z}\right), \\[2ex]
\text{(ii)} & \partial_t H_y + \dfrac{\sigma_z(z)}{\epsilon_0}H_y = \partial_t H_y^*, \\[2ex]
\text{(iii)} & \partial_t D_x^* + \dfrac{\sigma_z(z)}{\epsilon_0}D_x^* = -c_0\left(\dfrac{\partial H_y}{\partial z} + \mathbf{J}_s \cdot \hat{\mathbf{x}}\right), \\[2ex]
\text{(iv)} & \partial_t D_x = \partial_t D_x^* + \dfrac{\sigma_x(x)}{\epsilon_0}D_x^*, \\[2ex]
\text{(v)} & \partial_t D_z^* + \dfrac{\sigma_x(x)}{\epsilon_0}D_z^* = c_0\dfrac{\partial H_y}{\partial x}, \\[2ex]
\text{(vi)} & \partial_t D_z = \partial_t D_z^* + \dfrac{\sigma_z(z)}{\epsilon_0}D_z^*,
\end{array}
\right.
\tag{42}
$$

with

$$
\mathbf{D}(t) = \epsilon_\infty \mathbf{E}(t) + \mathbf{P}(t) + \mathbf{C}(t),
\tag{43}
$$

where $\mathbf{D} = (D_x, D_z)^T$, and inside of the dielectric the polarization $\mathbf{P} = (P_x, P_z)^T$ satisfies

$$
\tau\dot{\mathbf{P}} + \mathbf{P} = (\epsilon_s - \epsilon_\infty)\mathbf{E},
\tag{44}
$$

while the conductivity term $\mathbf{C} = (C_x, C_y)^T$ satisfies

$$
\dot{\mathbf{C}} = (\sigma/\epsilon_0)\mathbf{E}.
\tag{45}
$$

inside of the dielectric. Outside the dielectric we have $\mathbf{P} = \mathbf{C} = \mathbf{0}$. We will assume zero initial conditions for all the fields.

3.3   Pressure dependence of polarization

We consider a pressure dependent Debye model for orientational polarization first developed in [ABR02]. We assume that the material dependent parameters in the differential equation (44) for the Debye medium depend on pressure p, i.e.,

$$
\tau(p)\dot{\mathbf{P}} + \mathbf{P} = (\epsilon_s(p) - \epsilon_\infty(p))\mathbf{E}.
\tag{46}
$$

We suppose as a first approximation that each of the pressure dependent parameters can be prepresented as a mean value plus a perturbation that is proportional to the pressure

$$
\left\{
\begin{array}{ll}
\text{(i)} & \tau(p) = \tau_0 + \kappa_\tau p, \\[2mm]
\text{(ii)} & \epsilon_s(p) = \epsilon_{s,0} + \kappa_s p, \\[2mm]
\text{(iii)} & \epsilon_\infty(p) = \epsilon_{\infty,0} + \kappa_\infty p.
\end{array}
\right.
\tag{47}
$$

This can be considered as a truncation after the first-order terms of power series expansion of these functions of p. Thus (44) is written as

$$
(\tau_0 + \kappa_\tau p)\dot{\mathbf{P}} + \mathbf{P} = ((\epsilon_{s,0} - \epsilon_{\infty,0}) + (\kappa_s - \kappa_\infty)p)\mathbf{E}.
\tag{48}
$$

This model features modulation of the material polarization by the pressure wave and thus the behaviour of the electromagnetic pulse. We will assume that the acoustic pressure wave is specified *a priori*. The pressure p will be assumed to have the form

$$
p(t, z) = I_{(z_2, z_2 + \lambda_p)} \sin\left(\omega_p[t + \frac{z - z_2}{c_p}]\right),
\tag{49}
$$

where $z_2 \in Z_\mathrm{D}$ with $z_1 < z_2$. The terms ω_p, λ_p and c_p denote the acoustic frequency, wavelength and speed respectively. We note that outside the pressure region, the pressure coefficients κ_τ, κ_s and κ_∞ are all zero and

$$
\tau = \tau_0, \quad \epsilon_s = \epsilon_{s,0}, \quad \epsilon_\infty = \epsilon_{\infty,0}.
\tag{50}
$$

From (43)

$$
\left\{
\begin{array}{ll}
\text{(i)} & D_x(t) = (\epsilon_{\infty,0} + \kappa_\infty p)E_x(t) + P_x(t) + C_x(t), \\[1mm]
\text{(ii)} & D_z(t) = (\epsilon_{\infty,0} + \kappa_\infty p)E_z(t) + P_z(t) + C_z(t),
\end{array}
\right.
\tag{51}
$$

with

$$
\left\{
\begin{array}{ll}
\text{(i)} & (\tau_0 + \kappa_\tau p)\dot{P}_x + P_x = ((\epsilon_{s,0} - \epsilon_{\infty,0}) + (\kappa_s - \kappa_\infty)p)E_x, \\[1mm]
\text{(ii)} & (\tau_0 + \kappa_\tau p)\dot{P}_z + P_z = ((\epsilon_{s,0} - \epsilon_{\infty,0}) + (\kappa_s - \kappa_\infty)p)E_z,
\end{array}
\right.
\tag{52}
$$

and

$$
\left\{
\begin{array}{ll}
\text{(i)} & \dot{C}_x = (\sigma/\epsilon_0)E_x, \\[1mm]
\text{(ii)} & \dot{C}_z = (\sigma/\epsilon_0)E_z.
\end{array}
\right.
\tag{53}
$$

3.4 Source term

The source term $\mathbf{J}_s$ will model an infinite (in the y direction) antenna strip, finite in the x direction (between x_1 and x_2), lying in the $z = z_c$ plane in free space, and we assume the signal is polarized with oscillations in the xz plane only, with uniformity

in the y direction (see again Figure 1). We therefore take

$$\mathbf{J}_s(t, x, z) = I_{(x_1, x_2)}(x)\delta(z - z_c)\sin(\omega_c(t - 3t_0))\exp\left(-\left[\frac{t - 3t_0}{t_0}\right]^2\right)\hat{\mathbf{x}},$$

$$(54)$$

$$t_0 = \frac{2}{\omega_d - \omega_c}, \quad \omega_c = 2\pi f_c \text{ rad/sec}.$$

where $I_{(x_1, x_2)}$ is the indicator function on the interval $(x_1, x_2) \in X_0$, $\delta(z - z_c)$ is the Dirac measure centered at $z = z_c$, and $\hat{\mathbf{x}}$ is the unit vector in the x direction. The Fourier spectrum of this pulse has even symmetry about the frequency f_c. The pulse is centered at time step $3t_0$ and has a $1/e$ characteristic decay of t_0 time-steps [Taf95]. We will specify the values of all the different quantities involved in (54) when we define the particular problems that we will solve. The source (54) radiates numerical waves having time waveforms corresponding to the source function. In the discretized model, described below the radiated numerical wave will propagate to the Debye medium and undergo partial transmission and partial reflection, and time stepping can be continued until all transients decay.

3.5   Space and time discretization

We will use the FDTD algorithm [Taf95] to discretize Maxwell's equations. The FDTD algorithm uses forward differences to approximate the time and spatial derivatives. The FDTD technique rigorously enforces the vector field boundary conditions at interfaces of dissimilar media at the time scale of a small fraction of the impinging pulse width or carrier period. This approach is very general and permits accurate modeling of a broad variety of materials ranging from living human tissue to radar absorbers to optical glass. The system of equations (42) can be discretized on the standard Yee lattice. The domain Ω is divided into square cells of length $h = \Delta x = \Delta z$, h being the spatial increment. The degrees of freedom on an element are shown in Figure 4. The electric field degrees of freedom are at the midpoints of edges of the squares and the magnetic degrees of freedom are at the centers of cells. The time interval over which time stepping is done is divided into subintervals of equal size using the time increment Δt. We perform normal leapfrogging in time and the loss terms are averaged in time. This leads to an explicit time stepping scheme. In this case, a stability condition (CFL) has to be satisfied [Taf95] in order to obtain a well posed computational scheme. The time step Δt and the spactial increment h for the FD-TD scheme in non-dispersive dielectics are related by the condition

$$\eta_{\mathrm{CN}} = \frac{c_0 \Delta t}{h} < \frac{1}{\sqrt{2}} \tag{55}$$

The number η_{CN} is called the Courant number. We fix the value of $\eta_{\mathrm{CN}} = 1/2$. In [Pet94], the author established that several extensions of the FD-TD for Debye
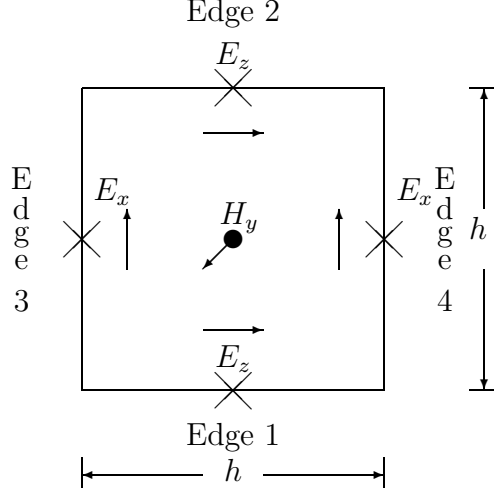
Figure 4: Degrees of freedom of **E** and **H** on a rectangle.

media satisfy the stability restriction of the standard FD-TD scheme in nondispersive dielectrics. He has also shown that the extensions do not preserve the non-dissipative character of the standard FD-TD scheme. The extended difference systems are more dispersive than the standard FD-TD, and their accuracy depends strongly on how well the chosen timestep resolves the shortest timescale in the problem regardless of whether it is the incident pulse timescale, the medium relaxation timescale, or the medium resonance timescale.

For any field variable V, we use the notation $V_{l,m}^r = V(r\Delta t, lh, mh)$, where $r, l, m \in \mathbb{N}$ or $r = r_0 \pm 1/2, l = l_0 \pm 1/2, m = m_0 \pm 1/2$, with $r_0, l_0, m_0 \in \mathbb{N}$. With the degrees of freedom as shown in Figure 4, the Maxwell curl equations are discretized as follows. Given the values of the electric field at time $n\Delta t$ and the values of the magnetic field at time $(n-1/2)\Delta t$, we then evaluate the magnetic field at time $(n+1/2)\Delta t$ and the electric field at time $(n+1)\Delta t$. We have for $H_y^* = H^*$

$$\frac{H^*|_{i+1/2,k+1/2}^{n+1/2} - H^*|_{i+1/2,k+1/2}^{n-1/2}}{\Delta t} + \frac{\sigma_x(i+1/2)}{\epsilon_0}\left(\frac{H^*|_{i+1/2,k+1/2}^{n+1/2} + H^*|_{i+1/2,k+1/2}^{n-1/2}}{2}\right)$$
$$= c_0\left(\frac{E_z|_{i+1,k+1/2}^n - E_z|_{i,k+1/2}^n}{\Delta x}\right) - c_0\left(\frac{E_x|_{i+1/2,k+1}^n - E_x|_{i+1/2,k}^n}{\Delta z}\right).$$

$$(56)$$

20

Solving (56) for $H^*|_{i+1/2,k+1/2}^{n+1/2}$ we have the update equation

$$H^*|_{i+1/2,k+1/2}^{n+1/2} = \left(\frac{2\epsilon_0 - \sigma_x(i+1/2)\Delta t}{2\epsilon_0 + \sigma_x(i+1/2)\Delta t}\right) H^*|_{i+1/2,k+1/2}^{n-1/2} + \left(\frac{2\epsilon_0 c_0 \Delta t}{2\epsilon_0 + \sigma_x(i+1/2)\Delta t}\right) \times$$
$$\left(\frac{E_z|_{i+1,k+1/2}^n - E_z|_{i,k+1/2}^n}{\Delta x} - \frac{E_x|_{i+1/2,k+1}^n - E_x|_{i+1/2,k}^n}{\Delta z}\right).$$

(57)

Similarly we discretize the update equations for the other field variables in (42). The update equation for $H_y = H$ is

$$H|_{i+1/2,k+1/2}^{n+1/2} = \left(\frac{2\epsilon_0 - \sigma_z(k+1/2)\Delta t}{2\epsilon_0 + \sigma_z(k+1/2)\Delta t}\right) H|_{i+1/2,k+1/2}^{n-1/2}$$
$$+ \left(\frac{2\epsilon_0}{2\epsilon_0 + \sigma_z(k+1/2)\Delta t}\right) \times \left(H^*|_{i+1/2,k+1/2}^{n+1/2} - H^*|_{i+1/2,k+1/2}^{n-1/2}\right).$$

(58)

The update equation for D_x^* is

$$D_x^*|_{i+1/2,k}^{n+1} = \left(\frac{2\epsilon_0 - \sigma_z(k)\Delta t}{2\epsilon_0 + \sigma_z(k)\Delta t}\right) D_x^*|_{i+1/2,k}^n$$
$$- \left(\frac{2\epsilon_0 c_0 \Delta t}{2\epsilon_0 + \sigma_z(k)\Delta t}\right) \times \left(\frac{H_y|_{i+1/2,k+1/2}^{n+1/2} - H_y|_{i+1/2,k-1/2}^{n+1/2}}{\Delta z} + J_{s,i+1/2,k}^n\right),$$

(59)

where the electromagnetic input source is chosen to have the form $\mathbf{J}_{s,i+1/2,k}^n = J_{s,i+1/2,k}^n \hat{\mathbf{x}}$. The update equation for D_x is

$$D_x|_{i+1/2,k}^{n+1} = D_x|_{i+1/2,k}^n + \left(\frac{2\epsilon_0 + \sigma_x(i+1/2)\Delta t}{2\epsilon_0}\right) D_x^*|_{i+1/2,k}^{n+1}$$
$$+ \left(\frac{2\epsilon_0 - \sigma_x(i+1/2)\Delta t}{2\epsilon_0}\right) D_x^*|_{i+1/2,k}^n.$$

(60)

The update equation for D_z^* is

$$D_z^*|_{i,k+1/2}^{n+1} = \left(\frac{2\epsilon_0 - \sigma_x(i)\Delta t}{2\epsilon_0 + \sigma_x(i)\Delta t}\right) D_z^*|_{i,k+1/2}^n$$
$$+ \left(\frac{2\epsilon_0 c_0 \Delta t}{2\epsilon_0 + \sigma_x(i)\Delta t}\right) \times \left(\frac{H_y|_{i+1/2,k+1/2}^{n+1/2} - H_y|_{i-1/2,k+1/2}^{n+1/2}}{\Delta x}\right).$$

(61)

Finally the update equation for D_z is

$$D_z|_{i,k+1/2}^{n+1} = D_z|_{i,k+1/2}^n + \left(\frac{2\epsilon_0 + \sigma_z(k+1/2)\Delta t}{2\epsilon_0}\right) D_z^*|_{i,k+1/2}^{n+1}$$
$$+ \left(\frac{2\epsilon_0 - \sigma_z(k+1/2)\Delta t}{2\epsilon_0}\right) D_z^*|_{i,k+1/2}^n.$$

(62)

For the update of E_x and E_z we will combine equations (51)-(53). From (53) we have the update for C_x and C_z as

$$
\begin{cases}
C_x|^{n+1} = C_x|^n + \left(\dfrac{\sigma \Delta t}{2\epsilon_0}\right)\left(E_x|^{n+1} + E_x|^n\right), \\[2mm]
C_z|^{n+1} = C_z|^n + \left(\dfrac{\sigma \Delta t}{2\epsilon_0}\right)\left(E_z|^{n+1} + E_z|^n\right).
\end{cases}
\tag{63}
$$

From (52) we have the update for P_x as

$$
\begin{aligned}
P_x|^{n+1} = {}& \left(1 + \frac{\Delta t}{2(\tau_0 + \kappa_\tau p^{n+1})}\right)^{-1}\left(1 - \frac{\Delta t}{2(\tau_0 + \kappa_\tau p^n)}\right)P_x|^n \\
& + \left(1 + \frac{\Delta t}{2(\tau_0 + \kappa_\tau p^{n+1})}\right)^{-1}\left(\frac{\Delta t((\epsilon_{s,0} - \epsilon_{\infty,0}) + (\kappa_s - \kappa_\infty)p^n)}{2(\tau_0 + \kappa_\tau p^n)}\right)E_x|^n \\
& + \left(1 + \frac{\Delta t}{2(\tau_0 + \kappa_\tau p^{n+1})}\right)^{-1}\left(\frac{\Delta t((\epsilon_{s,0} - \epsilon_{\infty,0}) + (\kappa_s - \kappa_\infty)p^{n+1})}{2(\tau_0 + \kappa_\tau p^{n+1})}\right)E_x|^{n+1}.
\end{aligned}
\tag{64}
$$

Similarly, from (52) we have the update for P_z as

$$
\begin{aligned}
P_z|^{n+1} = {}& \left(1 + \frac{\Delta t}{2(\tau_0 + \kappa_\tau p^{n+1})}\right)^{-1}\left(1 - \frac{\Delta t}{2(\tau_0 + \kappa_\tau p^n)}\right)P_z|^n \\
& + \left(1 + \frac{\Delta t}{2(\tau_0 + \kappa_\tau p^{n+1})}\right)^{-1}\left(\frac{\Delta t((\epsilon_{s,0} - \epsilon_{\infty,0}) + (\kappa_s - \kappa_\infty)p^n)}{2(\tau_0 + \kappa_\tau p^n)}\right)E_z|^n \\
& + \left(1 + \frac{\Delta t}{2(\tau_0 + \kappa_\tau p^{n+1})}\right)^{-1}\left(\frac{\Delta t((\epsilon_{s,0} - \epsilon_{\infty,0}) + (\kappa_s - \kappa_\infty)p^{n+1})}{2(\tau_0 + \kappa_\tau p^{n+1})}\right)E_z|^{n+1}.
\end{aligned}
\tag{65}
$$

From (51) we have

$$
E_x|^{n+1} = \frac{1}{(\epsilon_{\infty,0} + \kappa_\infty p^{n+1})}\left(D_x|^{n+1} - P_x|^{n+1} - C_x|^{n+1}\right).
\tag{66}
$$

Substituting the update equations for P_x^{n+1} and C_x^{n+1} in (66) we obtain an expression for E_x^{n+1} in terms of E_x^n, D_x^{n+1}, C_x^n and P_x^n given by

$$
\begin{aligned}
\mathcal{F}(p^{n+1}) = {}& \left(1 + \frac{\Delta t}{2(\tau_0 + \kappa_\tau p^{n+1})}\right)^{-1}\left(\frac{\Delta t((\epsilon_{s,0} - \epsilon_{\infty,0}) + (\kappa_s - \kappa_\infty)p^{n+1})}{2(\tau_0 + \kappa_\tau p^{n+1})}\right) \\
& + (\epsilon_{\infty,0} + \kappa_\infty p^{n+1}) + \frac{\sigma \Delta t}{2\epsilon_0} \\
E_x|^{n+1} = {}& \mathcal{F}(p^{n+1})^{-1}\left[D_x|^{n+1} - C_x^n - \frac{\sigma \Delta t}{2\epsilon_0}E_x|^n - \left(1 + \frac{\Delta t}{2(\tau_0 + \kappa_\tau p^{n+1})}\right)^{-1} \right. \\
& \left. \times \left\{\left(1 - \frac{\Delta t}{2(\tau_0 + \kappa_\tau p^n)}\right)P_x|^n + \left(\frac{\Delta t((\epsilon_{s,0} - \epsilon_{\infty,0}) + (\kappa_s - \kappa_\infty)p^n)}{2(\tau_0 + \kappa_\tau p^n)}\right)E_x|^n\right\}\right],
\end{aligned}
\tag{67}
$$

22

where $D_x|^{n+1}$ is calculated from (60). Thus, all the terms on the right side are known quantities, and we can use equation (67) to update E_x. Similarly the update equation for E_z is

$$
\begin{aligned}
E_z|^{n+1} = \mathcal{F}(p^{n+1})^{-1} &\left[D_z|^{n+1} - C_z^n - \frac{\sigma \Delta t}{2\epsilon_0} E_z|^n - \left(1 + \frac{\Delta t}{2(\tau_0 + \kappa_\tau p^{n+1})} \right)^{-1} \right. \\
&\left. \times \left\{ \left(1 - \frac{\Delta t}{2(\tau_0 + \kappa_\tau p^n)} \right) P_z|^n + \left(\frac{\Delta t((\epsilon_{s,0} - \epsilon_{\infty,0}) + (\kappa_s - \kappa_\infty)p^n)}{2(\tau_0 + \kappa_\tau p^n)} \right) E_z|^n \right\} \right],
\end{aligned}
\tag{68}
$$

with $\mathcal{F}(p^{n+1})$ as defined in (67). As before, we calculate $D_z|^{n+1}$ from (62). Hence all terms on the right hand side are known.

4 The forward problem for a Debye medium: First test case

As discussed in Section 3.3 the pressure dependent parameters ϵ_s^*, ϵ_∞^*, and τ^* are represented as a mean value plus a perturbation that is proportional to the pressure in equations (47) (as discussed in [ABR02]). In our first test case, we present numerical simulations for a Debye medium that is similar to water. For signal bandwidths in the microwave regime the dispersive properties of pure water are usually modeled by a Debye equation having a single molecular relaxation term. The mean values $\epsilon_{s,0}^*$, $\epsilon_{\infty,0}^*$, and τ_0^* for this Debye model [APM89] are given by

$$
\begin{aligned}
\epsilon_{s,0}^* &= 80.1 \quad \text{(relative static permittivity)}, \\
\epsilon_{\infty,0}^* &= 5.5 \quad \text{(relative high frequency permittivity)}, \\
\tau_0^* &= 8.1 \times 10^{-12} \quad \text{seconds}, \\
\sigma^* &= 1 \times 10^{-5} \quad \text{mhos/meter},
\end{aligned}
\tag{69}
$$

where the * superscript will denote the *true values* of all the corresponding dielectric parameters. Since we do not yet have experimental data to determine the actual values, we instead choose trial values for the coefficients of pressure, κ_s^*, κ_∞^* and κ_τ^*. As a first approximation we take these trial values to be a fraction of the mean values of the dielectric parameters, $\epsilon_{s,0}^*$, $\epsilon_{\infty,0}^*$, and τ_0^*, respectively. Thus, in the pressure region we choose

$$
\begin{aligned}
\kappa_s^* &= 0.6\epsilon_{s,0}^* = 48.06, \\
\kappa_\infty^* &= 0.8\epsilon_{\infty,0}^* = 4.4, \\
\kappa_\tau^* &= 0.05\tau_0^* = 4.05 \times 10^{-13}.
\end{aligned}
\tag{70}
$$

We hope to determine the values of these pressure coefficients from appropriately designed experiments in the near future. We have assumed that the effect of the

electric field on the acoustic pressure is negligible. We are interested in how and to what extent the acoustic pressure can change the reflected electric wave from the interface at $z = z_2$. Moreover, the relaxation parameter is a characteristic of the material in $[z_1, z_2]$, which affects the transmission of electric waves through this region. Consequently, we will examine in more detail how τ_0 can effect the electric field. The electromagnetic input source has the form

$$\mathbf{J}_s(t, x, z) = I_{(x_1, x_2)} \delta(z) \sin(\omega_c(t - 3t_0)) \exp\left(-\left[\frac{t - 3t_0}{t_0}\right]^2\right) \hat{\mathbf{x}}$$

$$t_0 = \frac{1}{2\pi \times 10^9}; \ \omega_c = 6\pi \times 10^9 \ \text{rad/sec}; \ f_c = 3.0 \times 10^9 \ \text{Hz}. \tag{71}$$

The Fourier spectrum of this pulse has even symmetry about 3.0 GHz. The computational domain is defined as follows. We take $X_0 = (0, 0.1)$, $Z_a = (0, 0.15)$ and $Z_D = (0.15, 0.2)$. The number of nodes along the z-axis is taken to be 320 and the number of nodes along the x-axis is taken to be 160. The spatial step size in both the x and z directions is $\Delta x = \Delta z = h = 0.1/160$. From the CFL condition (55) with the Courant number $\eta_{CN} = 1/2$ we obtain the time increment to be $\Delta t \approx 1.0417$ pico seconds. The central frequency of the input source as described in (71) is 3.0 GHz and based on the speed of light in air, $c_0 = 3 \times 10^8 \ m/s$, we calculate the corresponding central wavelength to be $\lambda_c = (2\pi c_0)/\omega = 0.1$ meters. The antenna is half a wavelength long and is placed at $(x_1, x_2) \times z_c$, with $z_c = 0$, $x_1 = 0.025$ and $x_2 = 0.075$. We use PML layers that are half a wavelength thick on all fours sides of the computational domain as shown in Figure 3. The reflections of the electromagnetic pulse at the air-Debye interface and from the acoustic pressure wave are recorded at the center of the antenna (x_c, z_c), with $x_c = 0.05$, at every time step. This data will be used as observations for the parameter identification problem to be presented later. The component of the electric field that is of interest here is the E_x component. Thus our data is the set

$$\mathbf{E}(\mathbf{q}^*) = \{E_x(n\Delta t, x_c, z_c; \mathbf{q}^*)\}_{n=1}^M$$

$$\mathbf{q}^* = (\epsilon_{s,0}^*, \epsilon_{\infty,0}^*, \tau_0^*, \sigma^*, \kappa_s^*, \kappa_\infty^*, \kappa_\tau^*)^T. \tag{72}$$

The windowed acoustic pressure wave as defined in (49) has the parameter values $\omega_p = 6.0\pi \times 10^5$ rad/sec, $c_p = 1500$ m/s, and thus, $\lambda_p = 0.005$. The location of the pressure region is in the interval $(z_2, z_2 + \lambda_p) = (0.175, 0.18)$.

In Figure 5 we plot the electromagnetic source that is used in the simulations for the Debye model (69). We plot the power spectral density of the source (71) in Figure 6. The power spectral density $|Y|^2$ of the vector $\mathbf{J}_s$ is defined to be

$$\mathcal{Z} = \text{FFT}(\mathbf{J}_s),$$

$$|Y|^2 = \mathcal{Z} \cdot \bar{\mathcal{Z}}, \tag{73}$$
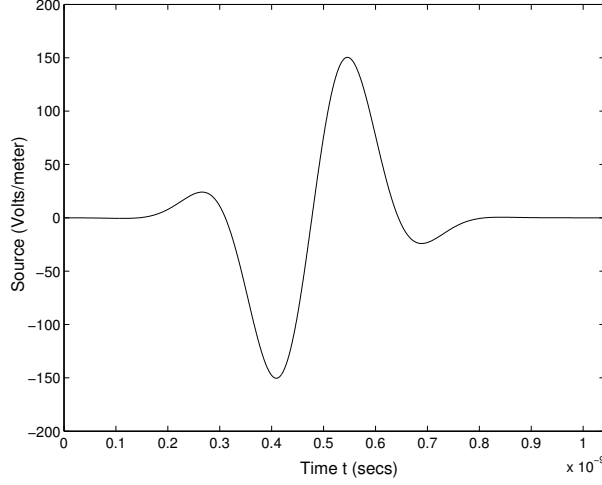
24

Figure 5: Forward Simulation for a Debye medium with parameters given in (69) and (70). The source as defined in (71)

where $\text{FFT}(\mathbf{J}_s)$ is the fast fourier transform of the vector $\mathbf{J_s}$. As seen in Figure 6 the power spectral density is symmetric about 3.0 GHz.

In Figures 7 and 8 we plot the E_x field magnitude at the center of the antenna versus time, which shows the electromagnetic source, the reflection off the air-Debye interface and the reflection from the region containing the acoustic pressure wave. As seen in these plots the amplitude of the reflection from the acoustic pressure is many orders of magnitude smaller than that of the initial electromagnetic source as well as that of the reflection from the air-Debye interface. Thus, it is an interesting question as to whether the reflections from the acoustic pressure region can be used for identification of parameters.

In Figure 9 we plot the power spectral density of the data in Figure 7. In Figures 10 -14 we plot the E_x field magnitude in the plane containing the center of the antenna versus depth along the z axis. Figures 10 and 11 shows the electromagnetic wave penetrating the Debye medium. In 12 we see the reflection of the electromagnetic wave from the Debye medium moving towards the antenna and the Brillouin precursor propagating in the Debye medium. In Figure 13 we observe the reflection from the region containing the acoustic pressure and the transmitted part of the electromagnetic source travelling into the absorbing layer. The reflection from the acoustic pressure crosses the Debye medium in Figure 14.

25
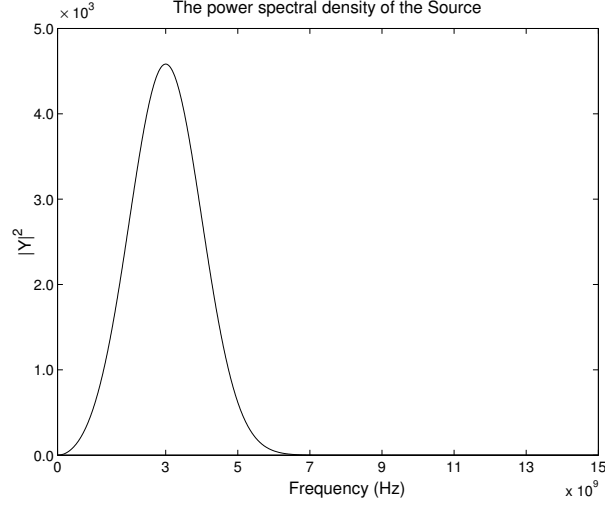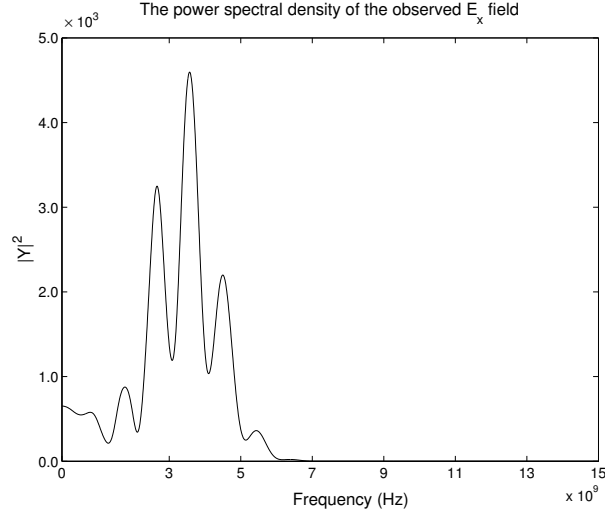
Figure 6: Fourier transform of the source. The transform is centered around the central frequency of $\omega = 6\pi \times 10^9$.

PSfrag replacements
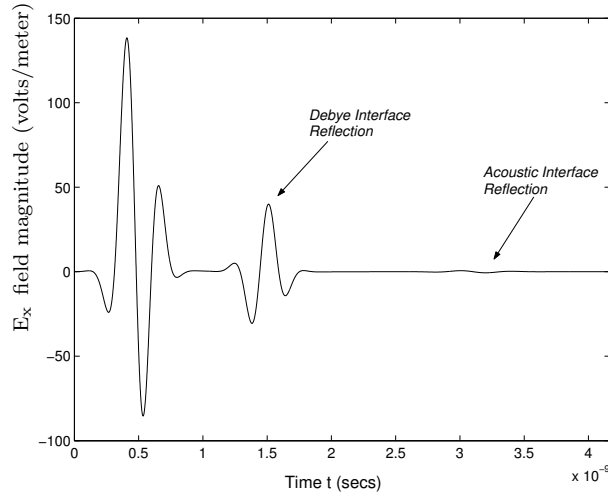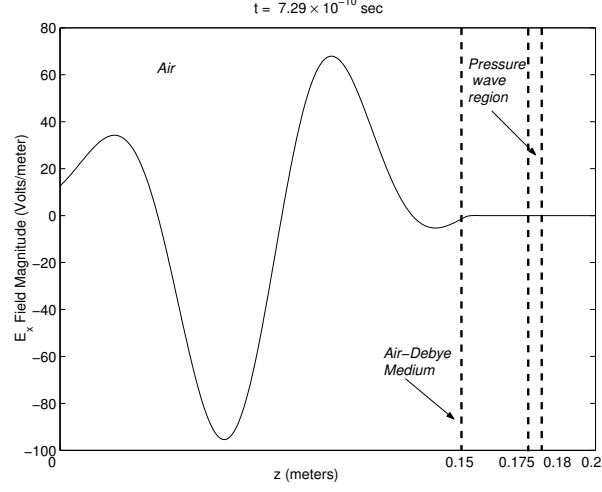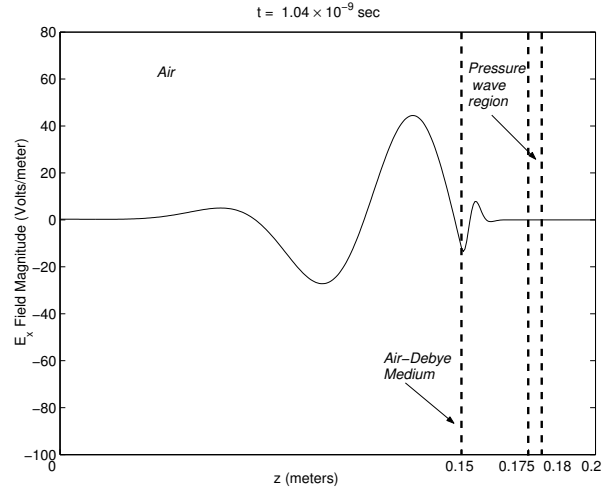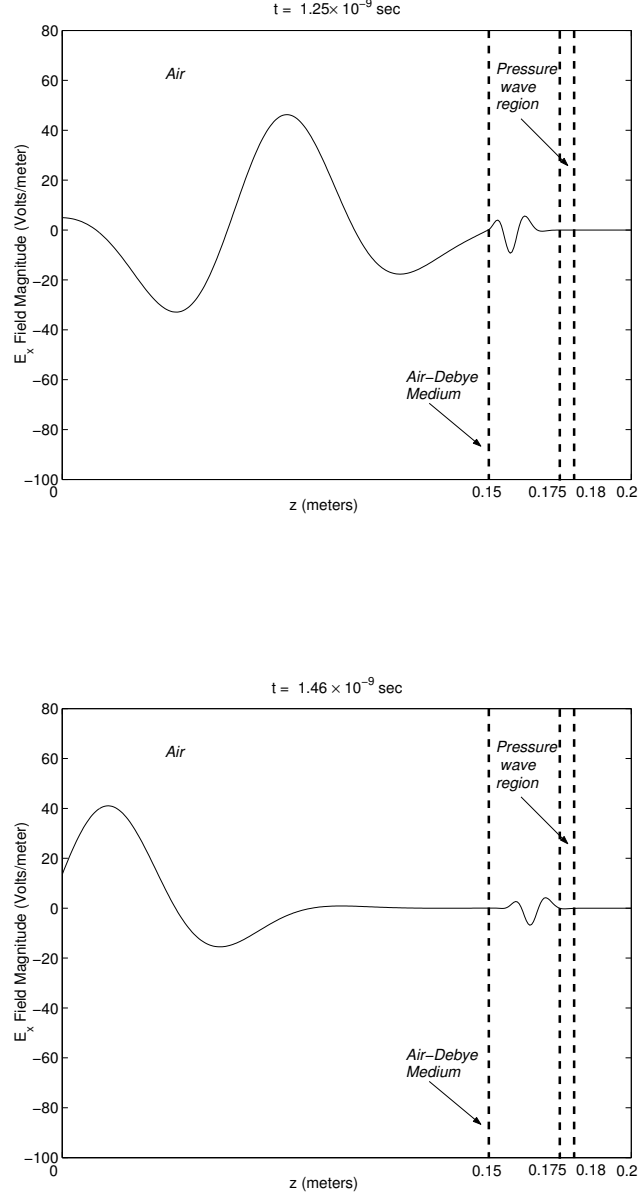
Figure 7: Forward simulation for a Debye medium with parameters given in (69) and (70). Time plot of the E_x component of the electric field. This is the data that is received at the center of the antenna. This plot consists of the original signal (source), the reflection off the Air-Debye interface and the reflection due to the pressure wave.
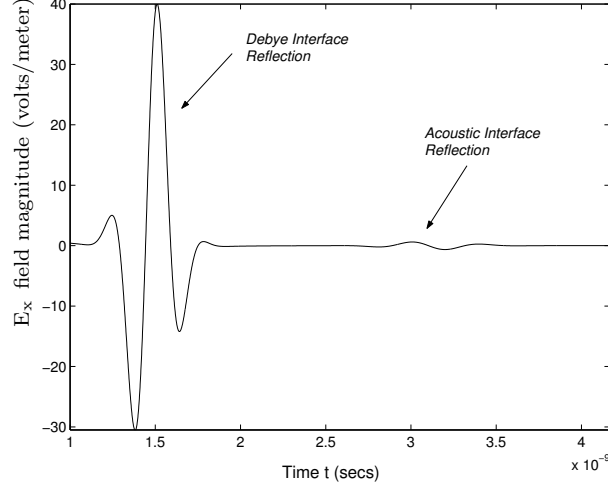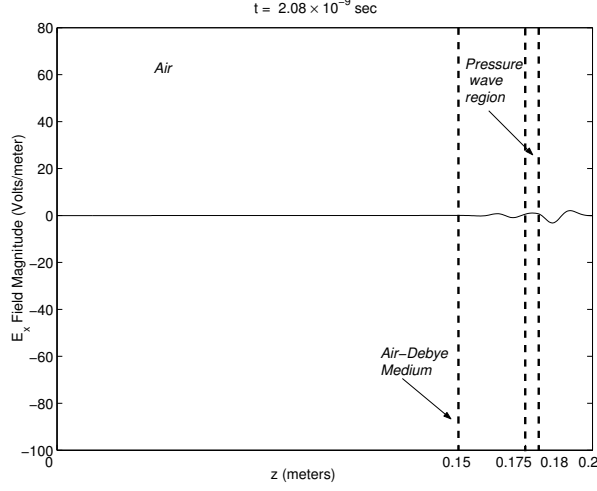
Figure 8: Forward simulation for a Debye medium with parameters given in (69) and (70). Time plot of the E_x component of the electric field. This is the data that is received at the center of the antenna. This plot consists of the reflection off the Air-Debye interface and the reflection due to the pressure wave.

Figure 9: Fourier transform of the data in Figure 7. The transform is centered around the central frequency of $\omega = 6\pi \times 10^9$.

27

Figure 10: Forward simulation for a Debye medium with parameters given in (69) and (70). Plot of the magnitude of the E_x component of the electric field against z (meters). The input source is propagating towards the Debye medium.

Figure 11: Forward simulation for a Debye medium with parameters given in (69) and (70). Plot of the magnitude of the E_x component of the electric field against z (meters). The input signal gets partially reflected off the Debye medium and partially transmitted into the medium.

Figure 12: Forward simulation for a Debye medium with parameters given in (69) and (70). Plots of the magnitude of the E_x component of the electric field against z (meters). In both the plots, the reflection off the air-Debye interface is seen moving towards the antenna, while the transmitted part of the source is seen propagating in the Debye medium towards the region containing the pressure wave.
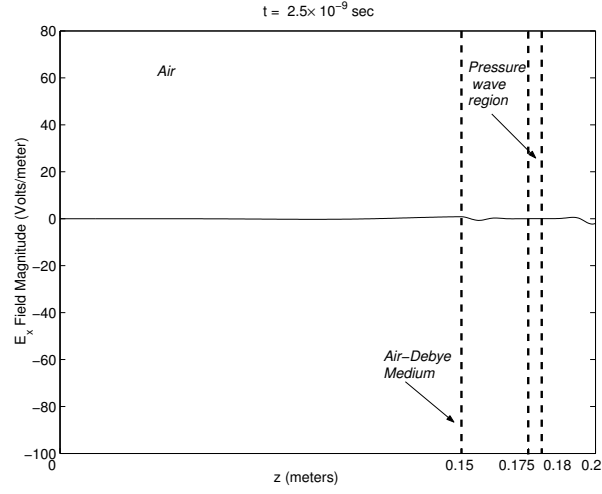
Figure 13: Forward simulation for a Debye medium with parameters given in (69) and (70). Plot of the magnitude of the E_x component of the electric field against z (meters). The interaction of the electromagnetic wave with the pressure wave causes the electromagnetic wave to partially reflect and partially transmit.

4.1 Sensitivity analysis

Here we examine the system dynamics as the parameters vary. We are interested in the changes produced by the coefficents of pressure in the polarization, namely the parameters κ_s, κ_∞ and κ_τ. In Figure 15 we plot the E_x component of the electric field for the simulation with parameter values given in (69) and four other simulations for which all the parameters, except κ_s, are fixed at the values given in (69). We change the value of κ_s to 0, $0.3\epsilon_{s,0}$, $0.6\epsilon_{s,0}$ and $0.9\epsilon_{s,0}$, repectively, and plot the electric field values for each of the corresponding forward simulations. As expected, by changing the value of κ_s, we notice a change in the magnitude of the acoustic reflection observed at the center of the antenna.

In order to determine if the forward problem is sensitive to changes in the value of the pressure coefficient κ_∞, in Figure 16 we plot the absolute value of the differences in the E_x field component between simulations in which all the parameters except κ_∞ are fixed at the values given in (69). The solid line in this figure represents the difference in the E_x field magnitude between the forward simulation in which $\kappa_\infty = 0.8\epsilon_{\infty,0}$ and the simulation in which $\kappa_\infty = 0$. The dashed line represents the difference in the E_x field magnitude between the simulation in which $\kappa_\infty = 0.8\epsilon_{\infty,0}$ and the simulation in which $\kappa_\infty = 0.2\epsilon_{\infty,0}$. We now determine if the forward problem is sensitive to changes in the value of the pressure coefficient κ_τ. In Figure 17 we plot the absolute value of the differences in the E_x field component between simulations in

Figure 14: Forward simulation for a Debye medium with parameters given in (69) and (70). Plot of the magnitude of the E_x component of the electric field against z (meters). The reflection from the acoustic pressure wave impinges on the air-Debye interface, while the wave transmitted into the pressure region moves into the right absorbing layer.
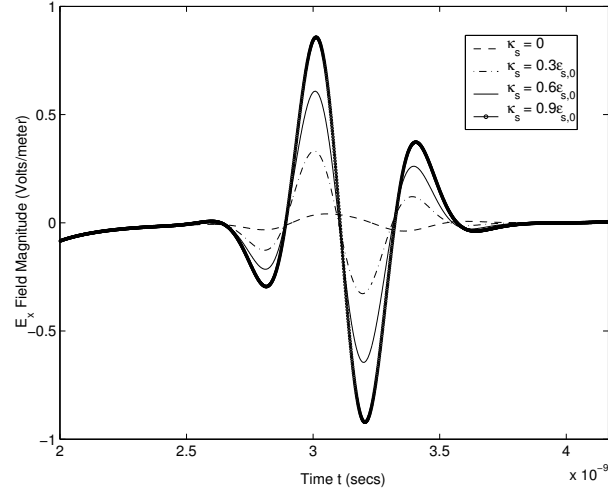

Figure 15: Plot of the magnitude of the E_x component of the electric field against z (meters) for different values of the parameter κ_s. The other parameters are fixed at the values given in (69) and (70)
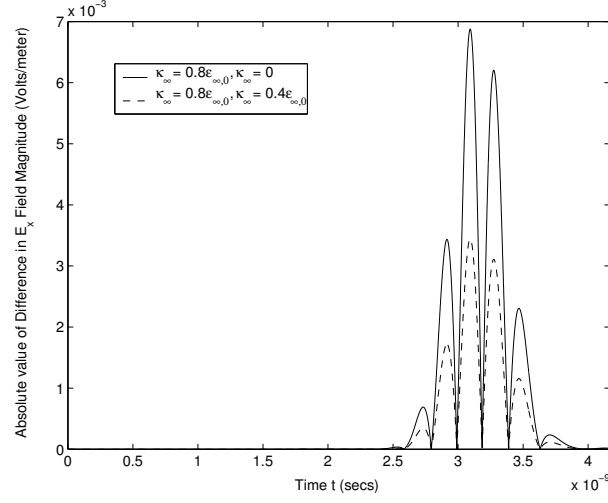
Figure 16: Plot of the absolute value of the difference in magnitude of the E_x component of the electric field, between simulations in which $\kappa_\infty = 0.8\epsilon_{\infty,0}$ and simulations with different values of κ_∞, against z (meters). The other parameters are fixed at the values given in (69) and (70).
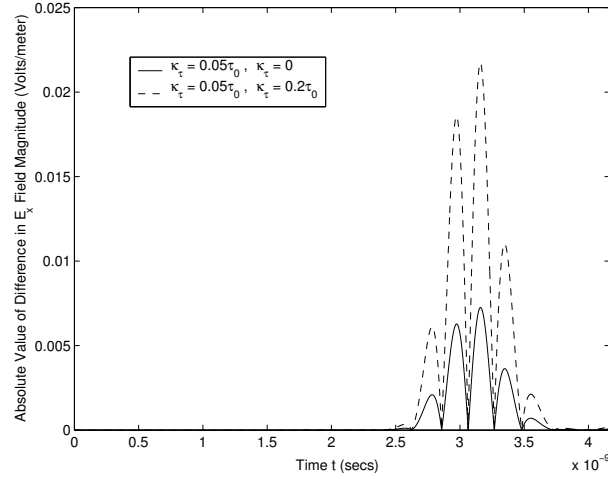
Figure 17: Plot of the absolute value of the difference in magnitude of the E_x component of the electric field, between simulations in which the value of $\kappa_\tau = 0.05\tau_0$ and simulations with different values of κ_τ, against z (meters). The other parameters are fixed at their true values.

which all the parameters except κ_τ are fixed at the values given in (69). The solid line in this figure represents the difference in the E_x field magnitude between the forward simulation in which $\kappa_\tau = 0.05\tau_0$ and the simulation in which $\kappa_\tau = 0$. The dashed line represents the difference in the E_x field magnitude between the simulation in which $\kappa_\tau = 0.05\tau_0$ and the simulation in which $\kappa_\tau = 0.2\tau_0$ From these plots we observe that the parameter κ_s seems to be the most influential in the wave interaction, whereas the pressure coefficients κ_∞ and κ_τ do not seem to be as influential. This observation can be supported from an analysis of (40). In our simulations the outgoing and reflected radiation will be dominated by frequencies near the center frequency 3.0 GHz. Thus, ϵ_r^* will be dominated by frequencies near 3.0 GHz. In this problem $\omega\tau_0^* \approx \mathcal{O}(10^{-2})$, and $\epsilon_0 = 8 \times 10^{-12}$. Rewriting (40) as

$$\epsilon_r^* = \frac{\epsilon_s}{1 + \mathrm{j}\omega\tau} + \left(\frac{\mathrm{j}\omega\tau}{1 + \mathrm{j}\omega\tau}\right)\epsilon_\infty + \frac{\sigma}{\mathrm{j}\omega\epsilon_0}, \tag{74}$$

we consider each of the three terms in (74) separately to determine their magnitude. The magnitudes of the corresponding true values of these three terms (neglecting the acoustic pressure terms) are approximately given as

$$\begin{aligned}
\left(\frac{\epsilon_{s,0}^*}{1 + \mathrm{j}\omega\tau_0^*}\right) &\approx \mathcal{O}(\epsilon_{s,0}^*) &\approx \mathcal{O}(10), \\
\left(\frac{\mathrm{j}\omega\tau_0^*}{1 + \mathrm{j}\omega\tau_0^*}\right)\epsilon_{\infty,0} &\approx \mathcal{O}(10^{-2}\epsilon_{\infty,0}^*) &\approx \mathcal{O}(10^{-2}), \\
\left(\frac{\sigma^*}{\mathrm{j}\omega\epsilon_0}\right) &\approx \mathcal{O}(10^2\sigma^*) &\approx \mathcal{O}(10^{-3}).
\end{aligned} \tag{75}$$

Thus we see that ϵ_r^* will be most sensitive to the static permittivity $\epsilon_{s,0}$ and the effects of $\epsilon_{\infty,0}$ and τ_0 will not be as pronounced. Also, this implies that ϵ_r^* will be more sensitive to the pressure coefficient κ_s than to the coefficients κ_∞ and κ_τ, which coincides with the observation that was made from Figures 15, 16 and 17

We would also like to see what effect the acoustic speed and frequency have on the amplitude of the reflection from the acoustic pressure region. In Figure 18 we plot the acoustic reflection observed at the center of the antenna for different values of the acoustic frequency and in Figure 19 we plot the acoustic reflection for different values of the acoustic speed. By changing the speed or the frequency, the wavelength λ_p changes and thus the size of the interval $(z_2, z_2 + \lambda_p)$ in which the pressure wave is generated. The amplitude of the acoustic reflection appears to decrease as the acoustic frequency is increased and increases at the acoustic speed increases. We note here that our windowed pressure wave contains only one wavelength of the sinusoid. Thus in general it will be difficult to predict precisely how the reflections will behave as the speed or the frequency is changed.
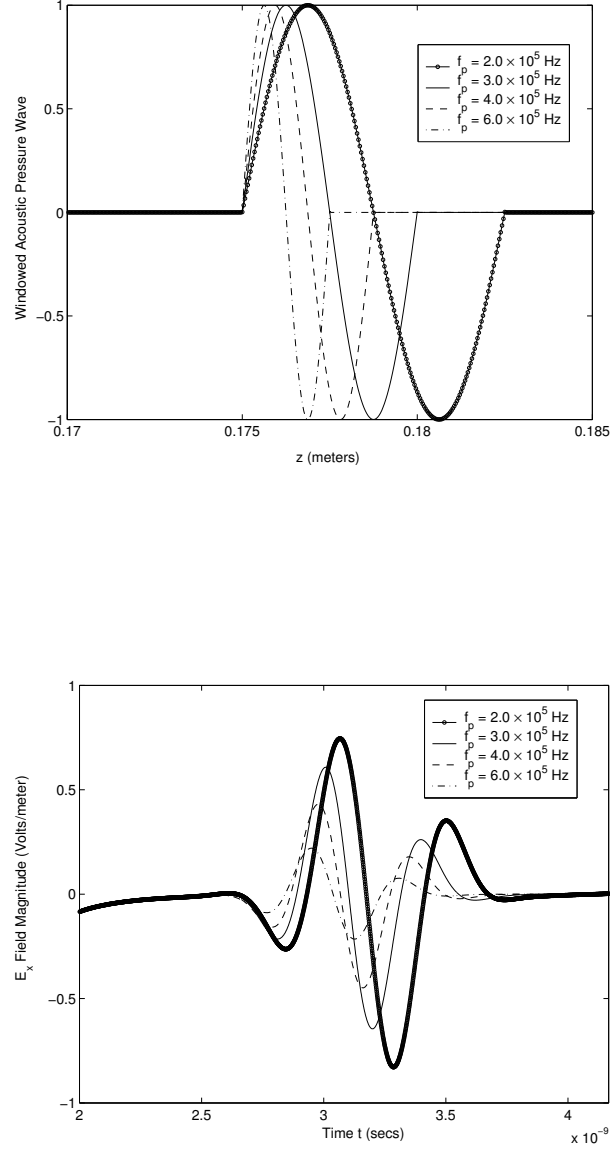
Figure 18: Plot of the reflection from the pressure region that is measured at the center of the antenna, versus time t (bottom), corresponding to different windowed acoustic pressure waves (top) of varying acoustic frequencies. The other parameters are fixed at the values given in (69) and (70). We note that the amplitude of the reflection changes as the frequency of the pressure wave changes.
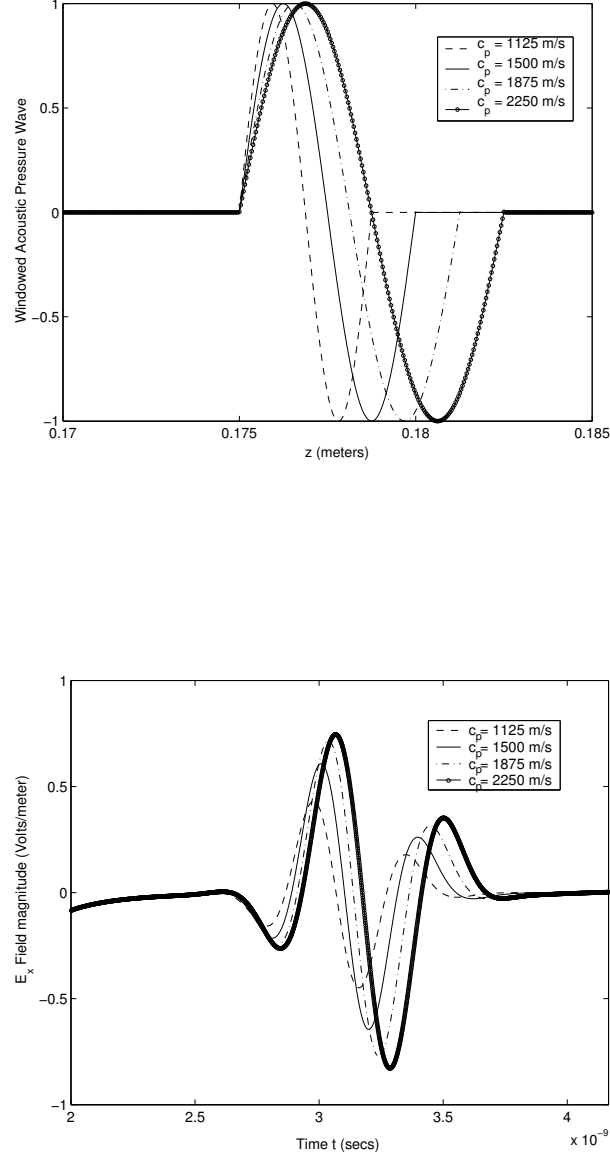
Figure 19: Plot of the reflection from the acoustic region that is measured at the center of the antenna, against time t (bottom), corresponding to different windowed acoustic pressure waves (top) of varying acoustic speeds. The other parameters are fixed at the values given in (69) and (70). We observe that the magnitude of the reflection is affected by the speed of the acoustic wave.

5 Parameter estimation and statistical inference: The inverse problem

In our forward simulations the signal that we record at the center of the antenna is a set of measurements of E_x, the x component of the electric field, at the point $(0, z_c)$ in our computational domain at discrete, uniformly spaced intervals of time. This signal has components consisting of the input source, the reflection at the air-Debye interface and another reflection from the region that contains the pressure wave as seen in Section 4. The signal is a function of the various dielectric properties of the Debye medium; namely, the static relative permittivity $\epsilon_{s,0}$, the infinite frequency permittivity $\epsilon_{\infty,0}$, the relaxation time τ_0, the conductivity σ, and the three pressure coefficients κ_s, κ_∞ and κ_τ. We collect all these quantities together to define the parameter vector

$$\mathbf{q} = [\epsilon_{s,0}, \epsilon_{\infty,0}, \tau_0, \sigma, \kappa_s, \kappa_\infty, \kappa_\tau]^T. \tag{76}$$

Thus, the signal recorded in the forward simulation is a function of $\mathbf{q}$, and changing the value of $\mathbf{q}$ will change the signal that is recorded. In general, such signals are usually obtained in an experimental setting conducted in a laboratory with physical equipment such as electric pulse generators to generate electric pulses, piezoelectric transducers that generate the acoustic pressure waves and antennas/receivers that record the electric field intensities. Moreover, such signals generated in an experimental setting are usually noisy, with noise arising through the equipment that is used; namely the resistor, antenna/receiver and the transducer, in our case. Implicit in such collection of measurements is the assumption that there exist *true* values of all the parameters that characterize the medium to be interrogated. We will denote the corresponding *true parameter vector* by $\mathbf{q}^*$.

In order to simulate an experimental situation (i.e., generate typical "data") we assume that there exist true values of all the parameters involved in our problem, and we *use these true values (which of course would not be known in an experimental setting!) in our forward simulation*, viz. the FDTD method and record the signal observed at the antenna as described above. We then add noise to the generated signal to produce a noisy signal which will form the *observations* or *data* that we will use in an inverse problem, as a substitute for data generated in the laboratory. The goal of our electromagnetic interrogation technique is to identify or estimate the true parameter $\mathbf{q}^*$ that characterizes the particular Debye medium being interrogated, from data that consists of a signal recorded at the center of the antenna. The reason for using simulated data in the inverse problem is to validate the methods first on "data" from known parameters in a setting with known noise. If we cannot estimate the dielectric parameters from data that is constructed via numerical simulations of our discrete model, then the reconstruction of these parameters from actual experimental data usually will not be feasible.

We can state the inverse or parameter estimation problem that we will attempt to

solve as follows: Using observations or data (electric field intensities containing noise collected at the center of the antenna), determine an estimate $\hat{\mathbf{q}}$, of the true parameter $\mathbf{q}^*$, that belongs to an admissible set Q, so that the solution of the forward problem with $\mathbf{q} = \hat{\mathbf{q}}$ best describes the data that is collected. When we have solved this deterministic problem (as will be detailed below), it will also be necessary to specify reliablility of our estimates, i.e., can we specify measures of uncertainty related to the estimate $\hat{\mathbf{q}}$ of $\mathbf{q}^*$? It is important to note that the uncertainty in consideration is inherent in the method of producing the estimates as well as in the process of data collection. Such measures of uncertainty will be specified by means of *confidence intervals*. These intervals are a probability statement about the procedure which is used to construct estimates of the parameters. Thus we are led in a completely natural way to stochastic or probabilistic aspects of estimates from a deterministic problem solved with deterministic algorithms [BB99]. The statistical error analysis that we will present here is based on standard statistical formulations as given in [DG95].

We first consider the two different ways in which we can add noise to our signal, i.e., the values of the x component, E_x, of the electric field observed at the center of the antenna, $(0, z_c)$, for different times $t_k = k\Delta t,\ k = 0, 1, \ldots, M$. We represent this signal as the vector

(i) $\mathbf{E}(\mathbf{q}^*) = \{E_k^*\}_{k=1}^M = (E_x(t_1, 0, z_c; \mathbf{q}^*), \ldots, E_x(t_M, 0, z_c; \mathbf{q}^*))^T$,

(ii) $\mathbf{q}^* = (\epsilon_{s,0}^*, \epsilon_{\infty,0}^*, \tau_0^*, \sigma^*, \kappa_s^*, \kappa_\infty^*, \kappa_\tau^*)^T$,
$$(77)$$

$\mathbf{q}^*$ being the true parameter vector.

1. *Relative random noise (RN)* : In this case the amplitude of the noise that is added is proportional to the size of the signal, $\{E_k^*\}_{k=1}^M$. Our simulated data is

$$O_k^s = E_k^*(1 + \nu\eta_k^s),\ k = 1, \ldots M, \tag{78}$$

where $\bar{\eta} = \{\eta_k\}_{k=1}^M$ are independent normally distributed random variables with mean zero and variance one, i.e., $\eta_k \sim \mathcal{N}(0, 1), k = 1, \ldots, M$. We express the relative magnitude of the noise as a percentage of the magnitude of $\mathbf{E}(\mathbf{q}^*)$ by taking two times the value of ν as the size of the random variable. For example, $\nu = 0.005$ corresponds to 1% relative noise [BBL00]. This noise model does not produce constant variance across the samples.

2. *Constant variance noise*: Since constant variance is most conveniently assumed in standard error analysis, we will consider estimates obtained from an inverse problem applied to simulated data which contains constant variance random noise. The data that we try to fit in this case is

$$O_k^s = E_k^* + \beta\eta_k^s,\ k = 1, \ldots M, \tag{79}$$

where as in (78), $\eta_k \sim \mathcal{N}(0, 1), k = 1, \ldots, M$. The constant β is taken to be the product $\nu\alpha$, where α is a scaling factor which is chosen so that the signal to noise ratio (SNR) of the data defined in (79) corresponds to data defined in (78) with noise level ν. This justifies comparing results obtained with the two different ways of adding comparable noise to our signal. This will be addressed in more detail in Section 5.

The vector $\mathbf{O}^s = \{O_k^s\}_{k=1}^M$ will be our data or observations, and the noise $\bar{\eta} = \{\eta_k\}_{k=1}^M$ will be referred to as the *measurement errors* corresponding to the observations. The statistical error analysis that we now develop is only applicable to the case of constant variance noise. Thus, for the rest of this section, we will assume that our observations are of the form (79). The sample observations $\mathbf{O}^s$, which are in general obtained from experiment, are a *realization* of the corresponding random variable $\mathbf{O} = (O_1, O_2, \ldots, O_M)^T$ which can be seen to be a transformation of the random variable $\bar{\eta}$. Thus

$$O_k = E_k^* + \beta\eta_k, \ \ k = 1, \ldots M, \tag{80}$$

is a stochastic process and has a multivariate normal distribution with mean vector $\mathbf{E}(\mathbf{q}^*)$ defined in (77, i) and *covariance matrix* $\beta^2 I_M$. The *statistical model*

$$\mathbf{O} \sim \mathcal{N}_M\{\mathbf{E}(\mathbf{q}^*), \beta^2 \mathcal{I}_M\}, \tag{81}$$

is a formal representation of the *population* of all possible realizations of $O_1, O_2, \ldots, O_M$ that can be observed. When we collect data, we are observing a single realization of $O_1^s, \ldots, O_M^s$ i.e., a *sample*. Our objective then is to estimate the true value of the parameter $\mathbf{q}^*$ by collecting data, i.e., observing a single realization of $\mathbf{O}$ as well as accounting for the fact that a different realization will produce a different estimate of $\mathbf{q}^*$. We would like to learn about the true value $\mathbf{q}^*$ (which determines the nature of the population) from a sample, as well as indicate the certainty (or uncertainty) that we can associate to our knowledge of this parameter. This process of making statements about a population of interest on the basis of a sample from the population is called *statistical inference*.

The unknown true parameters vector $\mathbf{q}^*$ will be estimated by means of a suitable function $\hat{\mathbf{q}}(\mathbf{O})$ of the observations $\mathbf{O}$. The function $\hat{\mathbf{q}}(\mathbf{O})$ is a random variable and is referred to as an *estimator*. When evaluated at a particular realization, $O_1^s, O_2^s, \ldots, O_M^s$, this estimator yields a numerical value that gives information about the true value of the parameter $\mathbf{q}^*$. For a particular realization $\mathbf{O}^s$ of the random variable of observations $\mathbf{O}$, we call $\hat{\mathbf{q}}(\mathbf{O}^s)$ an *estimate*. In this report we will consider the method of least squares to obtain estimates for the parameters and to calculate confidence intervals for the estimates by linearizing around the estimate $\hat{\mathbf{q}}(\mathbf{O}^s)$. In this case $\hat{\mathbf{q}}(\mathbf{O})$ will be the least squares estimator $\hat{\mathbf{q}}_{\mathrm{OLS}}(\mathbf{O})$. Associated with the random variable $\hat{\mathbf{q}}_{\mathrm{OLS}}(\mathbf{O})$ is the probability space $\mathcal{Q} = (Q, \mathcal{B}, m)$, where Q is the sample set of all admissible parameters $\mathbf{q}$, $\mathcal{B}$ is the σ-algebra of events and m is the probability measure (or distribution). Thus we look for the least squares estimator $\hat{\mathbf{q}}_{\mathrm{OLS}}(\mathbf{O})$

on Q such that

$$\hat{\mathbf{q}}_{\text{OLS}}(\mathbf{O}) = \arg \min_{\hat{\mathbf{q}} \text{ on } Q} \text{J}(\hat{\mathbf{q}}),$$

$$\text{J}(\hat{\mathbf{q}}) = \frac{1}{2} \sum_{k=1}^{M} |E_x(t_k, 0, z_c; \hat{\mathbf{q}}) - O_k|^2 \,,$$

(82)

where $\mathbf{E}(\mathbf{q}) = (E_x(t_1, 0, z_c; \mathbf{q}), E_x(t_2, 0, z_c; \mathbf{q}), \ldots, E_x(t_M, 0, z_c; \mathbf{q}))^T$ will be generated by our forward simulation. We will refer to the vector $\mathbf{E}(\mathbf{q})$ as our *simulations*. For a particular realization $\mathbf{O}^s$ of the random variable $\mathbf{O}$ of observations, this process will yield the least squares estimate $\hat{\mathbf{q}}_{\text{OLS}}(\mathbf{O}^s) \in Q$, where

$$\hat{\mathbf{q}}_{\text{OLS}}(\mathbf{O}^s) = \arg \min_{\mathbf{q} \in Q} \text{J}^S(\mathbf{q}),$$

$$\text{J}^S(\mathbf{q}) = \frac{1}{2} \sum_{k=1}^{M} |E_x(t_k, 0, z_c; \mathbf{q}) - O_k^s|^2 \,,$$

(83)

5.1 Calculation of confidence intervals via linearization

In general, the mappings between the parameters $\mathbf{q}$ and the simulations $\mathbf{E}$ are non-linear. Let $E_k = E_x(t_k, 0, z_c; \mathbf{q})$. The functions

$$E_1(q_1, \ldots, q_l) = E_x(t_1, 0, z_c; \mathbf{q}),$$

$$E_2(q_1, \ldots, q_l) = E_x(t_2, 0, z_c; \mathbf{q}),$$

$$\vdots$$

$$E_M(q_1, \ldots, q_l) = E_x(t_M, 0, z_c; \mathbf{q}),$$

(84)

denote real-valued differentiable functions of the unknown parameters $\mathbf{q} = (q_1, \ldots, q_l)^T$, where $1 \leq l \leq 7$ depending on how many parameters we attempt to identify. Let $\mathbf{q} = \mathbf{q}^* + \mathcal{D}_{\mathbf{q}}$, where the corrector term $\mathcal{D}_{\mathbf{q}} = (\Delta q_1, \ldots \Delta q_l)^T$ is unknown. Linearizing the functions in (84) around the true parameter $\mathbf{q}^*$ by using the Taylor expansion we obtain

$$E_k(q_1, \ldots q_l) = E_k(q_1^* + \Delta q_1, \ldots, q_l^* + \Delta q_l)$$

$$= E_k(\mathbf{q}^*) + \sum_{j=1}^{l} \frac{\partial E_k}{\partial q_j} \bigg|_{\mathbf{q}^*} \Delta q_j, \ k = 1 \ldots M.$$

(85)

Let us define

$$\mathcal{D}_{\text{e}} = (O_1 - E_1(\mathbf{q}^*), \ldots, O_M - E_M(\mathbf{q}^*))^T,$$

(86)

and

$$\mathcal{X}(\mathbf{q}^*) = \begin{pmatrix} \frac{\partial E_1}{\partial q_1} \bigg|_{\mathbf{q}^*} & \cdots & \frac{\partial E_1}{\partial q_l} \bigg|_{\mathbf{q}^*} \\ \vdots & \vdots & \vdots \\ \frac{\partial E_M}{\partial q_1} \bigg|_{\mathbf{q}^*} & \cdots & \frac{\partial E_M}{\partial q_l} \bigg|_{\mathbf{q}^*} \end{pmatrix}.$$

(87)

Thus, in order to estimate the unknown corrector terms by the method of least squares, the estimator $\hat{\mathcal{D}}_{\mathrm{OLS}}$ is determined by

$$\hat{\mathcal{D}}_{\mathrm{OLS}} = \min_{\mathcal{D}_q} \frac{1}{2}(\mathcal{D}_{\mathrm{e}} - \mathcal{X}(\mathbf{q}^*)\mathcal{D}_{\mathbf{q}})^T(\mathcal{D}_{\mathrm{e}} - \mathcal{X}(\mathbf{q}^*)\mathcal{D}_{\mathbf{q}}), \tag{88}$$

which is the linearized version of (82). This involves solving

$$\frac{\partial\left(\mathcal{D}_e^T\mathcal{D}_e - 2\mathcal{D}_e^T\mathcal{X}(\mathbf{q}^*)\hat{\mathcal{D}}_{\mathrm{OLS}} + \hat{\mathcal{D}}_{\mathrm{OLS}}^T\mathcal{X}(\mathbf{q}^*)^T\mathcal{X}(\mathbf{q}^*)\hat{\mathcal{D}}_{\mathrm{OLS}}\right)}{\partial\hat{\mathcal{D}}_{\mathrm{OLS}}} = 0, \tag{89}$$

and the corresponding optimality condition yields the estimator

$$\hat{\mathcal{D}}_{\mathrm{OLS}} = (\mathcal{X}(\mathbf{q}^*)^T\mathcal{X}(\mathbf{q}^*))^{-1}\mathcal{X}(\mathbf{q}^*)^T\mathcal{D}_{\mathrm{e}}. \tag{90}$$

We note that the expected value of $\hat{\mathcal{D}}_{\mathrm{OLS}}$ is $\mathrm{Exp}(\hat{\mathcal{D}}_{\mathrm{OLS}}) = 0$, and the covariance matrix of $\hat{\mathcal{D}}_{\mathrm{OLS}}$ and hence also of $\hat{\mathbf{q}}_{\mathrm{OLS}}$ is

$$\begin{aligned}\mathrm{Cov}(\hat{\mathcal{D}}_{\mathrm{OLS}}) &= (\mathcal{X}(\mathbf{q}^*)^T\mathcal{X}(\mathbf{q}^*))^{-1}\mathcal{X}(\mathbf{q}^*)^T\mathrm{Cov}(\mathcal{D}_{\mathrm{e}})\mathcal{X}(\mathbf{q}^*)(\mathcal{X}(\mathbf{q}^*)^T\mathcal{X}(\mathbf{q}^*))^{-1}\\ &= \beta^2(\mathcal{X}(\mathbf{q}^*)^T\mathcal{X}(\mathbf{q}^*))^{-1} = \mathrm{Cov}(\hat{\mathbf{q}}_{\mathrm{OLS}}),\end{aligned} \tag{91}$$

where $\hat{\mathbf{q}}_{\mathrm{OLS}} = \mathbf{q}^* + \hat{\mathcal{D}}_{\mathrm{OLS}}$, and β is defined in (79). Thus the least squares estimator is a random variable with a multivariate normal distribution which after linearization can be approximately represented as

$$\hat{\mathbf{q}}_{\mathrm{OLS}}(\mathbf{O}) \sim \mathcal{N}_l\left(\mathbf{q}^*, \beta^2[\mathcal{X}^T(\mathbf{q}^*)\mathcal{X}(\mathbf{q}^*)]^{-1}\right). \tag{92}$$

However, when data is generated in an experimental setting, we do not have any knowledge of the true parameter vector $\mathbf{q}^*$ and hence we cannot calculate $\left(\mathcal{X}(\mathbf{q}^*)^T\mathcal{X}(\mathbf{q}^*)\right)^{-1}$. Thus, we further approximate our least squares estimator as having the multivariate normal distribution

$$\hat{\mathbf{q}}_{\mathrm{OLS}}(\mathbf{O}) \sim \mathcal{N}_l\left(\hat{\mathbf{q}}_{\mathrm{OLS}}(\mathbf{O}^s), \hat{\beta}_{\mathrm{OLS}}^2[\mathcal{X}^T(\hat{\mathbf{q}}_{\mathrm{OLS}}(\mathbf{O}^s))\mathcal{X}(\hat{\mathbf{q}}_{\mathrm{OLS}}(\mathbf{O}^s))]^{-1}\right), \tag{93}$$

which is obtained by repeating the linearization process around the estimate $\hat{\mathbf{q}}_{\mathrm{OLS}}(\mathbf{O}^s)$ obtained from a realization $\mathbf{O}^s$ of the random variable $\mathbf{O}$ of observations. The value of $\hat{\beta}_{\mathrm{OLS}}^2$ is chosen as

$$\hat{\beta}_{\mathrm{OLS}}^2 = \frac{1}{M-l}\sum_{k=1}^{M}|E_x(t_k, 0, z_c; \hat{\mathbf{q}}_{\mathrm{OLS}}(\mathbf{O}^s)) - O_k^s|^2, \tag{94}$$

which is the minimum value of the least squares objective function scaled by $2/(M-l)$.

Whenever an estimate based on data is reported, it should be accompanied by an assessment of uncertainty based on the sampling distribution. To this end we

will construct confidence intervals for all the estimates that we will provide. The approach we use is to look at the standard error (SE) for each of the l components of the estimate $\hat{\mathbf{q}}_{\text{OLS}}(\mathbf{O}^s)$, which is given for its jth component by the jth diagonal term of the covariance matrix, i.e.,

$$
\begin{aligned}
\text{SE}(\hat{q}_{\text{OLS},j}) &= \sqrt{\text{var}(\hat{q}_{\text{OLS},j}(\mathbf{O}^s))} \\
&= \sqrt{\hat{\beta}_{\text{OLS}}^2 \left((\mathcal{X}(\hat{\mathbf{q}}_{\text{OLS}}(\mathbf{O}^s))^T \mathcal{X}(\hat{\mathbf{q}}_{\text{OLS}}(\mathbf{O}^s)))^{-1} \right)_{jj}} \quad j = 1, \ldots, l.
\end{aligned} \tag{95}
$$

We construct the intervals

$$
\text{CI}_j = (\hat{q}_{\text{OLS},j}(\mathbf{O}^s) - 1.96 SE(\hat{q}_{\text{OLS},j}), \quad \hat{q}_{\text{OLS},j}(\mathbf{O}^s) + 1.96 SE(\hat{q}_{\text{OLS},j})), \ j = 1, \ldots, l, \tag{96}
$$

for which

$$
m\left(\{\hat{q}_{\text{OLS},j}(\mathbf{O}^s) - 1.96 SE(\hat{q}_{\text{OLS},j}) < \hat{q}_{\text{OLS},j}(\mathbf{O}) < \hat{q}_{\text{OLS},j}(\mathbf{O}^s) + 1.96 SE(\hat{q}_{\text{OLS},j})\}\right) = 0.95,
$$
$$
j = 1, \ldots, l, \tag{97}
$$

where m is the probability measure for the probability space $\mathcal{Q}$, and M is sufficiently large that one can use a Gaussian $\mathcal{N}(0,1)$ distribution in computing confidence intervals. These intervals CI_j are called confidence intervals with confidence level 0.95 or the 95% confidence interval.

Remark 2 *The confidence intervals are a probability statement about the procedure by which an estimate is constructed from a sample of the population. They are not a probability statement about the true parameter $\mathbf{q}^*$ which is fixed. If we could construct the confidence intervals, from our estimation procedure, for all possible data samples of size M, then 95% of such intervals would cover the true parameter values $\mathbf{q}^*$. However, for a particular data sample $\mathbf{O}^s$, the confidence intervals constructed as above may or may not cover the true parameter $\mathbf{q}^*$. What we can state is that we are 95% confident that the confidence intervals constructed by our estimation procedure would cover $\mathbf{q}^*$.*

6 Parameter estimation: First test problem

We now attempt to estimate the dielectric parameters for the Debye medium defined in (69) and (70). We restate the values of all the parameters below

$$
\begin{aligned}
\epsilon_{s,0}^* &= 80.1 & \kappa_s^* &= 48.06 \\
\epsilon_{\infty,0}^* &= 5.5 & \kappa_\infty^* &= 4.4 \\
\tau_0^* &= 8.1 \times 10^{-12} & \kappa_\tau^* &= 4.05 \times 10^{-13}. \\
\sigma^* &= 1 \times 10^{-5}
\end{aligned} \tag{98}
$$

We will refer to the values (98) as the true values of the parameters. We will solve the corresponding least squares optimization problem using two different methods; the Nelder-Mead algorithm, which is a simplex based, gradient free method, and the Levenberg-Marquardt trust region method that uses forward finite differences to calculate the gradient. From our estimates for all the seven parameters we will show that our problem is sensitive to only three of the seven parameters. We will then try to estimate two or three of the parameters to which our problem is sensitive. The particular implementation of the Levenberg-Marquardt and the Nelder-Mead algorithm that are used in this report are based on the corresponding algorithms presented in [Kel99]

6.1 Simulation results: The Nelder-Mead method

We first present parameter estimation results using the Nelder-Mead simplex based algorithm which is used for optimization in noisy problems. The Nelder-Mead simplex algorithm keeps a simplex $\mathcal{S}$ of approximations to an optimal point. In this algorithm the vertices of the simplex $\{\mathbf{q}_i\}_{i=1}^{l+1}$, where l is the size of $\mathbf{q}$, are sorted according to the least squares objective function values

$$\mathrm{J}^S(\mathbf{q}_1) \leq \mathrm{J}^S(\mathbf{q}_2) \leq \ldots \mathrm{J}^S(\mathbf{q}_{l+1}). \tag{99}$$

$\mathbf{q}_1$ is called the best vertex and $\mathbf{q}_{l+1}$ the worst. The algorithm attempts to replace the worst vertex $\mathbf{q}_{l+1}$ with a new point of the form

$$\mathbf{q}(\nu_{nm}) = (1 + \nu_{nm})\bar{\mathbf{q}} - \nu_{nm}\mathbf{q}_{l+1}, \tag{100}$$

where $\bar{\mathbf{q}}$ is the centroid of the convex hull of $\{\mathbf{q}_i\}_{i=1}^{l+1}$

$$\bar{\mathbf{q}} = \frac{1}{l} \sum_{i=1}^{l} \mathbf{q}_i. \tag{101}$$

The value of ν_{nm} is selected from a sequence of values that are computed by performing several different operations on the simplex. In general, the Nelder-Mead algorithm is not guaranteed to converge, even for smooth problems. The failure mode is stagnation at a nonoptimal point. For further details we refer the reader to [Kel99].

In the first test we will try to estimate all of seven parameters in $\mathbf{q}^*$. The initial simplex is chosen to have values that are 5-10% larger than the true parameter values given in (98). We do not add any noise to our data that is used in the parameter estimation in this first test. The final estimates from the Nelder-Mead algorithm are presented in Table 1. The details of the simulation are plotted in Figures 21-22. Figure 21 plots the various features of the Nelder-Mead run as functions of the number of iterations. The algorithm is terminated when the maximum least squares function value difference between any two points in the simplex is less than 10^{-8}.

Parameter	True Values	Final Estimates
$\epsilon_{s,0}$	80.1	80.1111
$\epsilon_{\infty,0}$	5.5	5.7461
τ_0	8.1×10^{-12}	8.1283×10^{-12}
σ	1.0×10^{-5}	1.1972×10^{-5}
κ_s	48.06	48.1227
κ_∞	4.4	4.9148
κ_τ	4.05×10^{-13}	4.1935×10^{-13}

Table 1: Final estimates for all seven parameters for water using Nelder-Mead. The initial parameter simplex has values that are 5-10% larger than the true values.

Function Difference	7.6979×10^{-9}
Max Oriented Length	2.4986×10^{-3}
Average least squares value	9.8451×10^{-6}
Best Least squares value	9.8392×10^{-6}
L^2 norm of the gradient	1.008×10^{-2}
L^∞ norm of gradient	8.756×10^{-3}
Number of forward solves	453

Table 2: Status of the Nelder-Mead Simulation at the 283rd iteration.
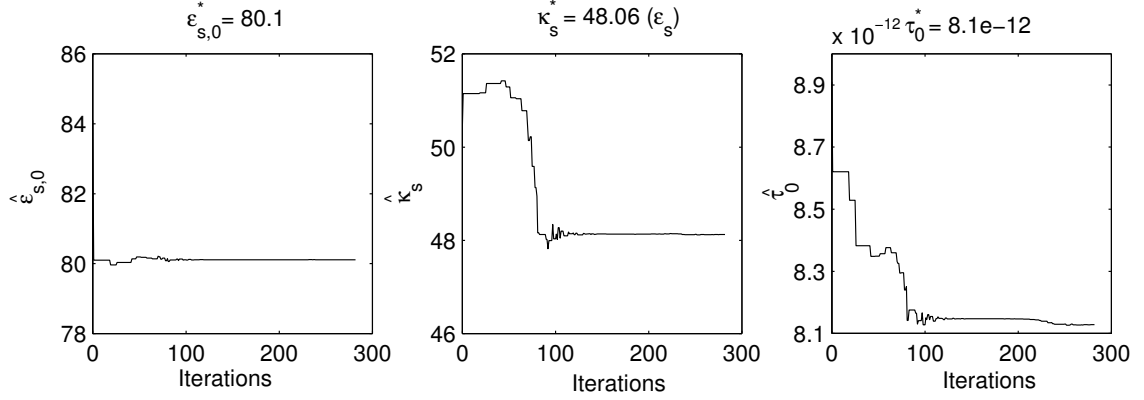
Figure 20: Variation of $\epsilon_{s,0}$, τ_0 and κ_s with respect to iteration number. Out of all seven parameters these three parameters are relatively well estimated.

The algorithm converges in 283 iterations. Table 2 presents the final status of the simulation. In Figure 21, the maximum oriented length is defined as

$$\text{Max Oriented length} = \max_{2 \leq i \leq l+1} ||\mathbf{q}_1 - \mathbf{q}_i||. \tag{102}$$

Also the gradient in this case refers to the simplex gradient. As can be seen from Figure 22 the parameters $\epsilon_{\infty,0}$, σ and the two pressure coefficients κ_∞ of $\epsilon_{\infty,0}$ and κ_τ of τ_0 are difficult for the inverse problem to identify. On the other hand, from Figure 20 we see that the parameters $\epsilon_{s,0}$ and its pressure coefficient κ_s as well as the parameter τ_0 are relatively well estimated. Since the inverse problem is only able to identify three parameters in the absence of noise we do not expect to see any improvement when noise is added to the data! Thus we will henceforth concentrate on the identification of $\epsilon_{s,0}$, τ_0 and κ_s.

We will first attempt the identification of $\epsilon_{s,0}$ and κ_s. In a first test, we fix all the other 5 parameters (including τ_0) at the true values and attempt to identify $\epsilon_{s,0}$ and κ_s. Table 3 presents the results for this test. As can be seen from Table 3, with the other 5 parameters fixed at their true values we do not have any difficulty in identifying $\epsilon_{s,0}$ and κ_s accurately. In Table 3, FC denotes the function count, i.e., the number of times the least squares objective function is evaluated. In Figure 23 we plot the values of $\hat{\epsilon}_{s,0}$ (left) and $\hat{\kappa}_s$ (right) over all iterations, for the three different initial simplicies with values that are 5%-10% lower than $\mathbf{q}^*$ (o-), 5% -10% higher than $\mathbf{q}^*$(- -), and 50%-60% lower than $\mathbf{q}^*$(-).

In Figure 24 we plot the details of the Nelder-Mead simulations for the three different initial simplices tabulated in Table 3. In each case the algorithm converges when the difference between function values is less than 10^{-8}. For the second case
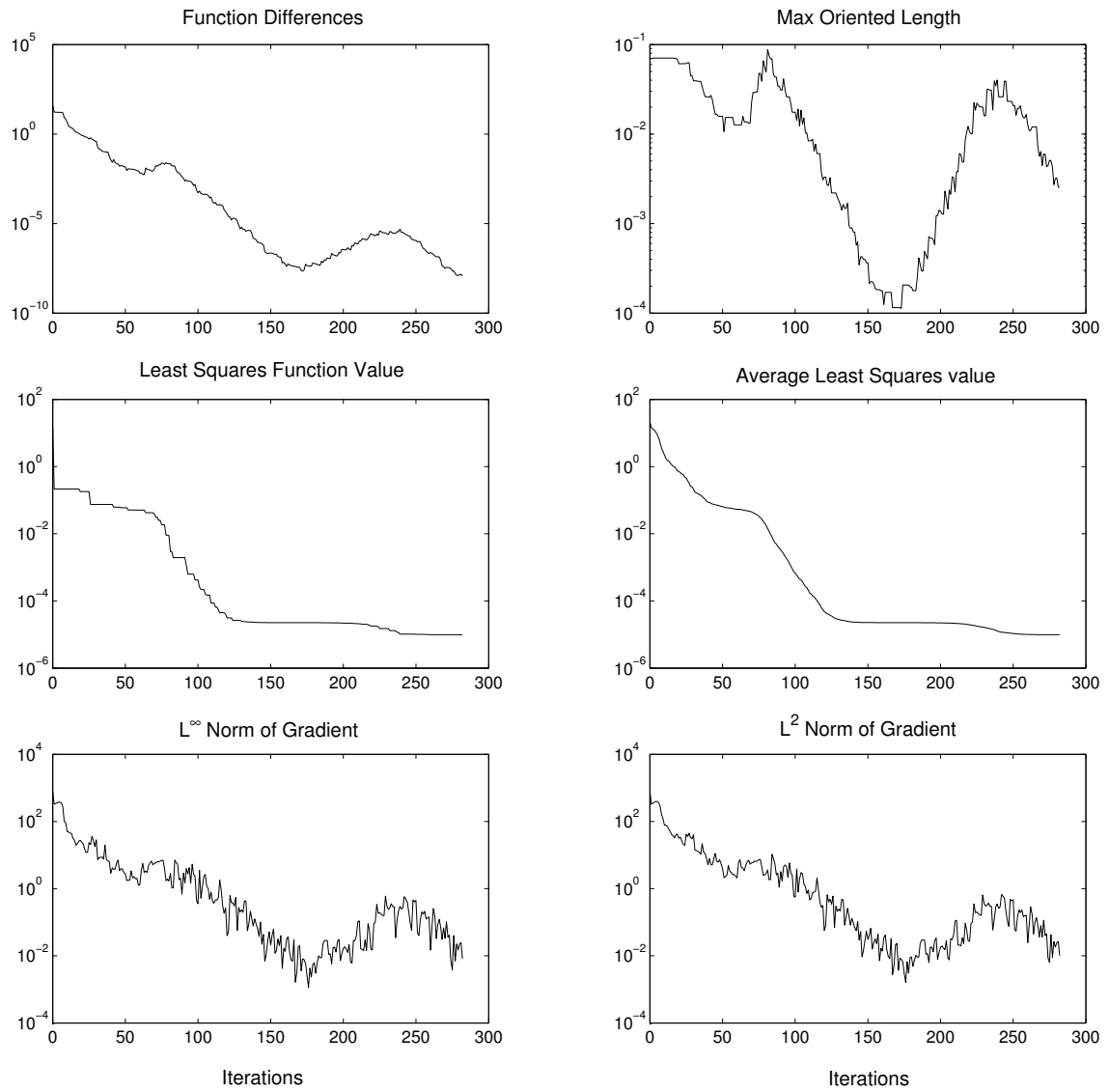
44

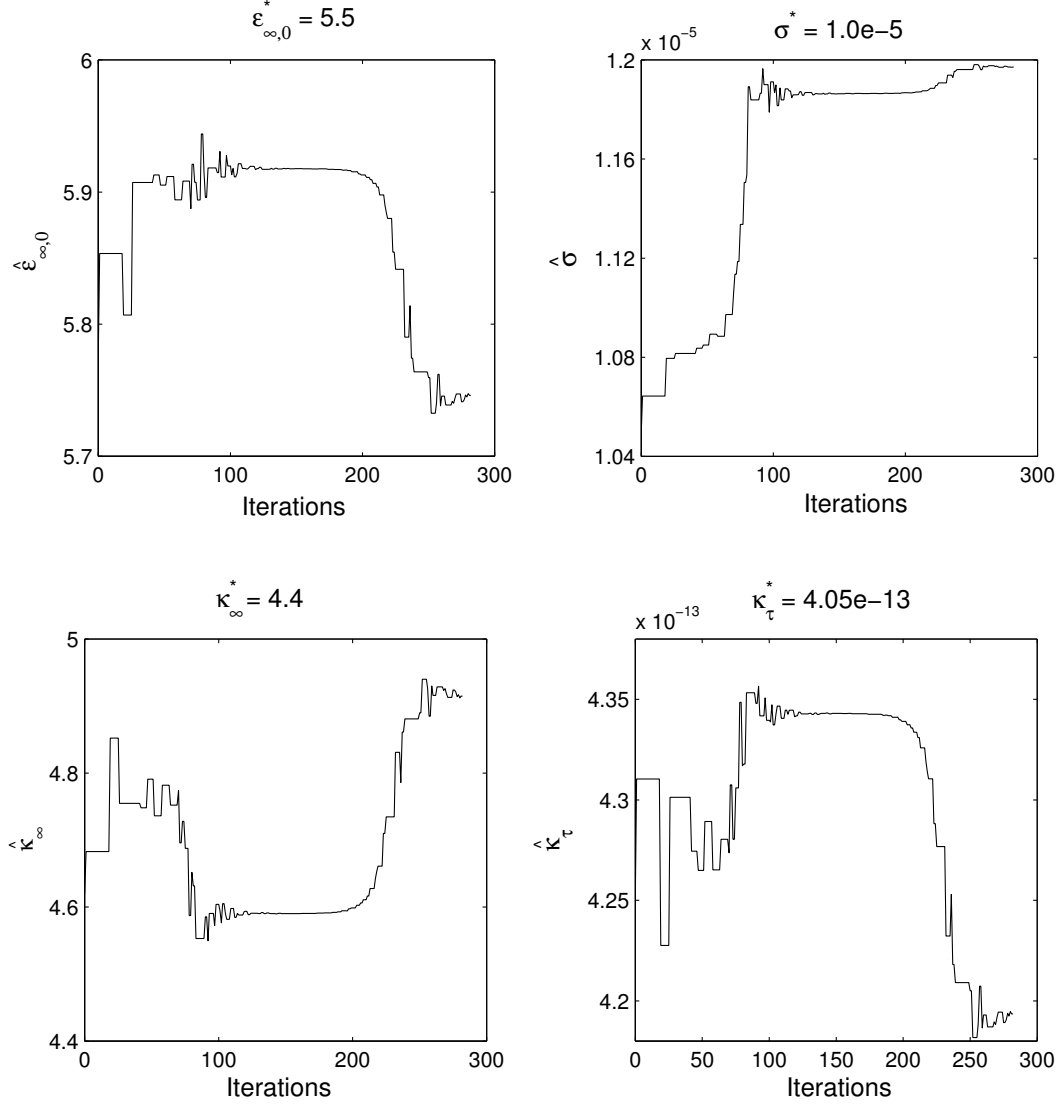Figure 21: Nelder-Mead for the estimation of seven parameters for water.

Figure 22: Variation of $\hat{\epsilon}_{\infty,0}$, $\hat{\sigma}$ and estimates of the two pressure coefficients, namely, $\hat{\kappa}_{\infty}$ and $\hat{\kappa}_{\tau}$, with respect to iteration number. As can be seen our inverse problem is not sensitive to these four parameters and their identification is difficult even in the absence of noise.
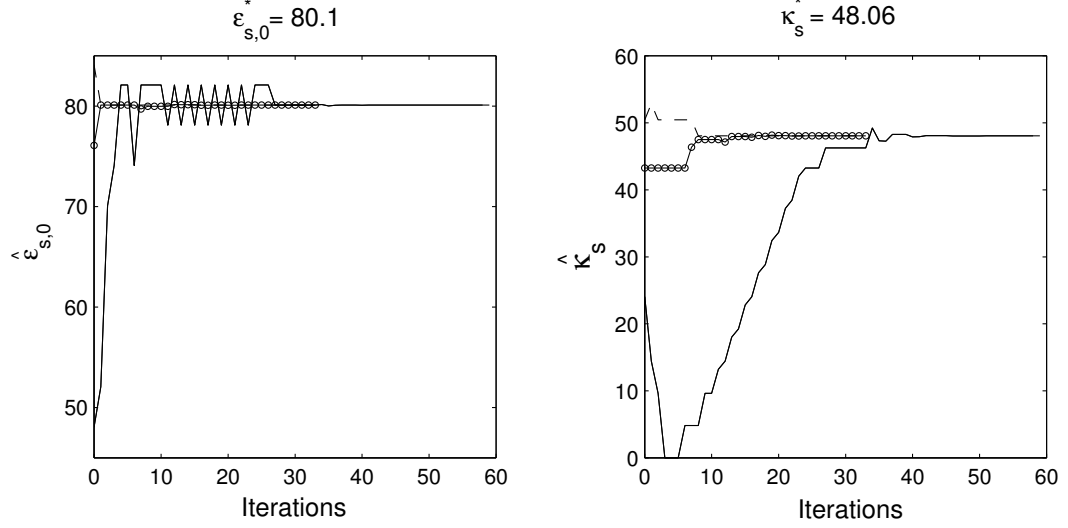
Figure 23: Plots of $\hat{\epsilon}_{s,0}$ (left) and $\hat{\kappa}_s$ (right) against the number of iterations for simulations in which the other five parameters are fixed at their true values and no noise is added to the data. (o-) $0.95\mathbf{q}^*$, (- -) $1.05\mathbf{q}^*$, (-) $0.5\mathbf{q}^*$.

Table 3: Parameter estimation of $\epsilon_{s,0}$ and κ_s for different initial simplices with no added noise.

$\mathbf{q}_0$	Iter	$\hat{\epsilon}_{s,0}$	$\hat{\kappa}_s$	$|\mathrm{J}_{n+1}^S - \mathrm{J}_0^S|$	J^S	$||\nabla \mathrm{J}^S||_{L^2}$	FC
$0.95\mathbf{q}^*$	33	80.0999	48.0607	4.7019×10^{-9}	1.4560×10^{-8}	0.0204	65
$1.05\mathbf{q}^*$	32	80.1	48.06	9.5079×10^{-9}	7.1205×10^{-27}	0.0096	66
$0.5\mathbf{q}^*$	59	80.1001	48.0603	8.4746×10^{-9}	5.5171×10^{-9}	0.0130	112

47

where the initial simplex has points with 5%-10% larger values than the true values, we obtain an unusually small least squares function value of the order of 10^{-27}. We believe this to be an accidental artifact of the algorithm. In Figure 25 and 26 we plot the least squares objective function for values of $\epsilon_{s,0}$ and $\hat{\kappa}_s$ that differ by 0%-10% from the true values. The other five parameters are kept fixed at their true values. From Figures 25 and 26, we determine that our inverse problem is more sensitive to $\epsilon_{s,0}$ than to the pressure coefficient κ_s. This is expected as the static relative permittivity, $\epsilon_{s,0}$ is more influential in the system dynamics than the pressure coefficients, and hence is also more important in identifying and characterizing the material.

As explained in Section 5, in a more realistic situation we will not have access to the true values of any of the parameters. Hence, we now fix five of the seven parameters at values that have a relative error from the true values of about 10%-50%. We use the values

$$
\begin{aligned}
\epsilon_{\infty,0} &= 6.0, \\
\tau_0 &= 10.0 \times 10^{-12}, \\
\sigma &= 1.5 \times 10^{-5}, \\
\kappa_\infty &= 4.8, \\
\kappa_\tau &= 5.0 \times 10^{-13},
\end{aligned}
\tag{103}
$$

in our simulations. Such choices for the parameters are typical in testing algorithms [BK89]. We use different initial guesses for $\epsilon_{s,0}$ and κ_s. Also in an experimental setting noise is introduced into the data, as discussed earlier. To simulate the experimental process in data collection we first add relative random noise to our data, and we use the fixed values (103) in the inverse problem. The results are tabulated in 4. From Table 4 we see that using the inverse problem we are able to estimate $\epsilon_{s,0}$ but we are unable to reconstruct κ_s with good accuracy. In Figure 27 we plot the values of $\hat{\epsilon}_{s,0}$ (left) and $\hat{\kappa}_s$ (right) over all iterations, In Figure 28 we plot the details of the Nelder-Mead simulation for the results in Figure 27 and Table 4 which show the final estimates of $\epsilon_{s,0}$ and κ_s for water. The other five parameters are fixed at the values given in (103) and relative noise of varying levels is added to the data.

To understand why κ_s is not recovered, we note that the fixed value of τ_0 in (103) has a relative error of 23% from its true value. Since the reflections from the acoustic

Table 4: Parameter estimation of $\epsilon_{s,0}$ and κ_s for 0%, 1%, 3% and 5% relative noise.

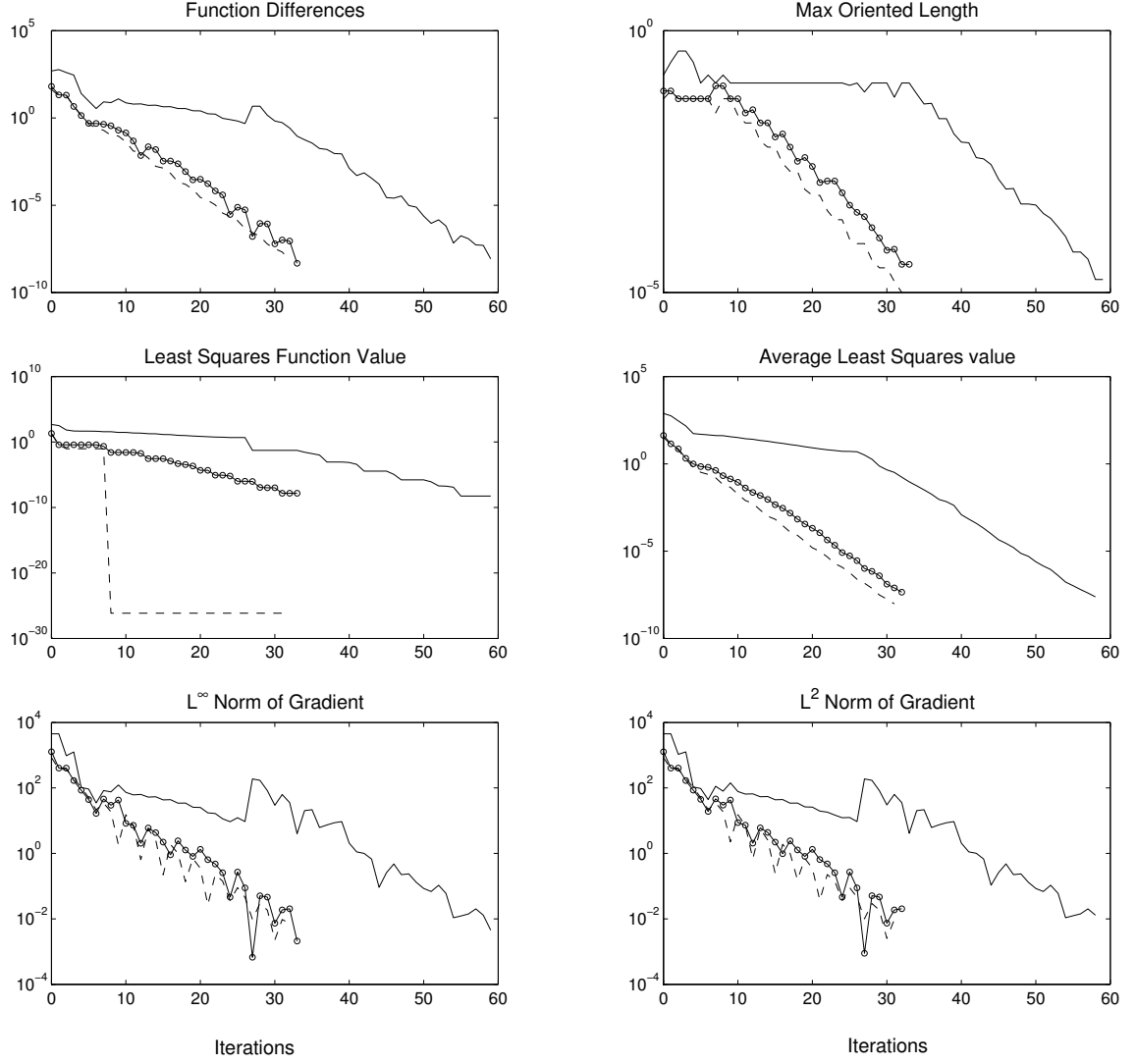| % RN	Iter	$\hat{\epsilon}_{s,0}$	$\hat{\kappa}_s$	$|\mathrm{J}_{n+1}^S - \mathrm{J}_0^S|$	J^S	$||\nabla \mathrm{J}^S||_{L^2}$	FC
0.0	37	80.3636	66.0486	8.5719×10^{-9}	2.5594	0.0076	73
1.0	41	80.3638	66.0422	3.2939×10^{-9}	25.2195	0.0098	80
3.0	40	80.3640	66.0280	8.6023×10^{-9}	208.1146	0.0080	77
5.0	40	80.3643	66.0157	6.3563×10^{-9}	574.4429	0.0060	79

Figure 24: Nelder-Mead for the estimation of $\epsilon_{s,0}$ and κ_s for water. The other five parameters are fixed at their true values and no noise is added to the data. (o-) $0.95\mathbf{q}^*$, (- -) $1.05\mathbf{q}^*$, (-) $0.5\mathbf{q}^*$.
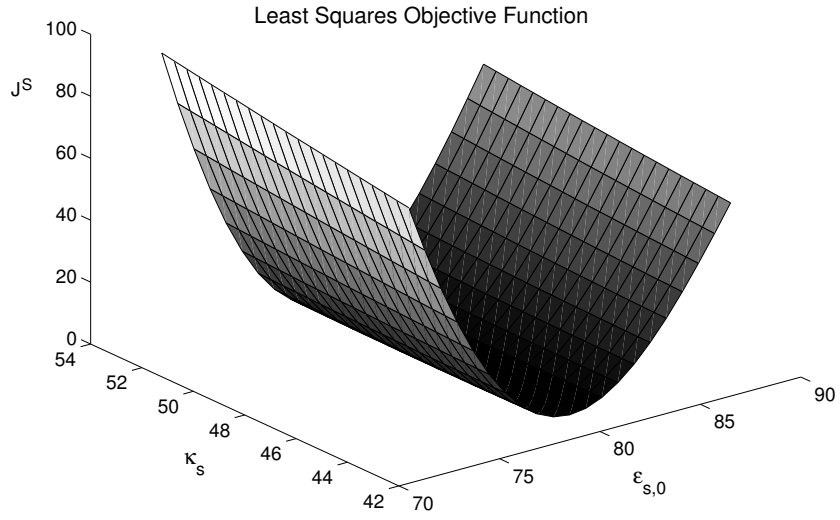
Figure 25: The Least Squares Objective Function for different values of $\epsilon_{s,0}$ and κ_s. We can see from this plot that the problem is more sensitive to $\epsilon_{s,0}$ than to the pressure coefficient κ_s.
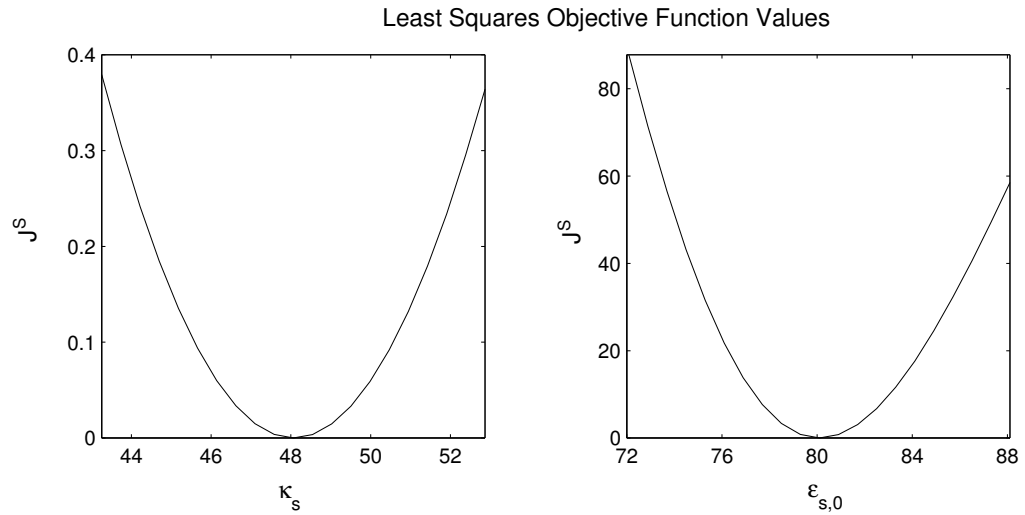
Figure 26: Cross-sections of the Least Squares Objective function versus κ_s (left) and versus $\epsilon_{s,0}$ (right). Note the difference in scales between the two figures.
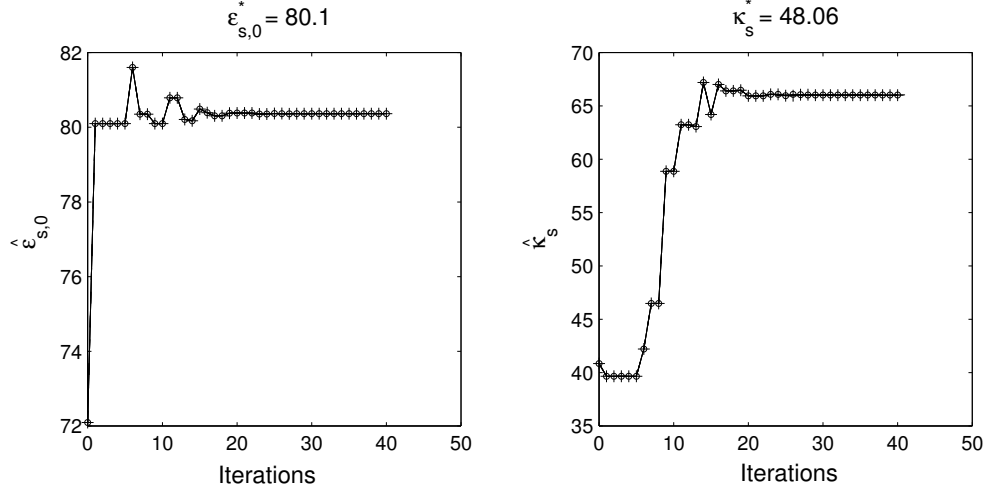
Figure 27: Plots of $\hat{\epsilon}_{s,0}$ (left) and $\hat{\kappa}_s$ (right) against the number of iterations for simulations in which the other five parameters are fixed at values that have 10%-50% relative error from the true values (103) and relative noise of varying levels is added to the data.

region depend strongly on the value of τ_0, a relative error of 23% is too high to get a good estimate of the pressure coefficients. To test this we lower the value of τ_0 to 8.91×10^{-12}. So instead of the values in (103) we will use the values

$$
\begin{aligned}
\epsilon_{\infty,0} &= 6.0, \\
\tau_0 &= 8.91 \times 10^{-12}, \\
\sigma &= 1.5 \times 10^{-5}, \\
\kappa_\infty &= 4.8, \\
\kappa_\tau &= 5.0 \times 10^{-13}.
\end{aligned}
\tag{104}
$$

This value of τ_0 has a relative error of 10% from its true value τ_0^*. With this new fixed value for τ_0 we attempt the inverse problem again to reconstruct $\hat{\epsilon}_{s,0}$ and $\hat{\kappa}_s$. These results are presented in Table 5. From Table 5 we observe that the estimated value of κ_s is closer to the true value than in the previous test. Thus we can obtain accurate estimates of κ_s by choosing values of τ_0 that are closer to its true value. We can conclude that if the value of τ_0 is not accurately known, then the identification of κ_s is difficult. The identification of $\epsilon_{s,0}$ on the other hand does not appear to be sensitive to the fixed value of τ_0 that is chosen. The combined identification of both $\epsilon_{s,0}$ and κ_s appears to be quite insensitive to the level of relative noise that is added to the data. The results of the Nelder-Mead run and the variation of the parameters over all iterations are plotted in Figures 29 and 30, respectively.
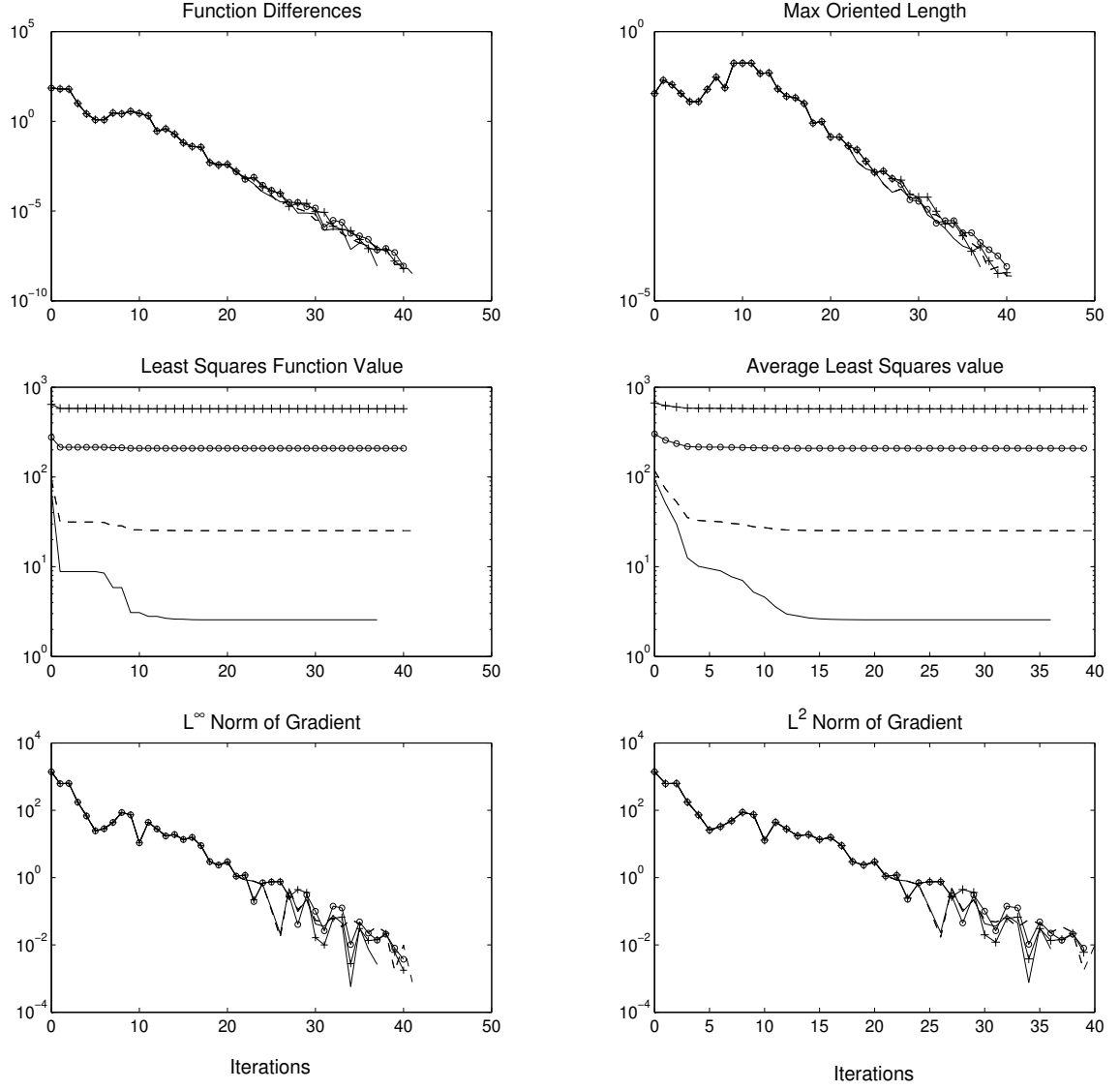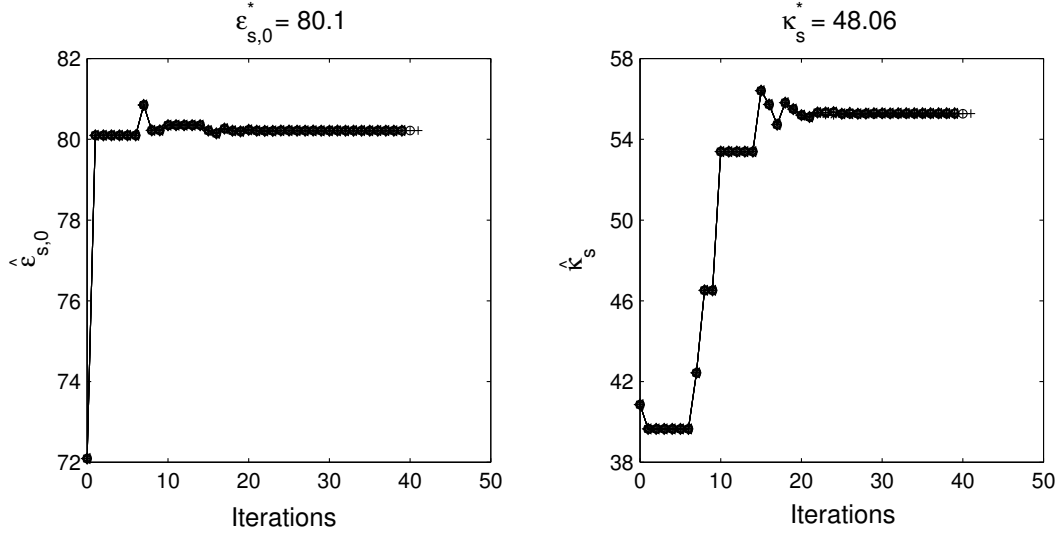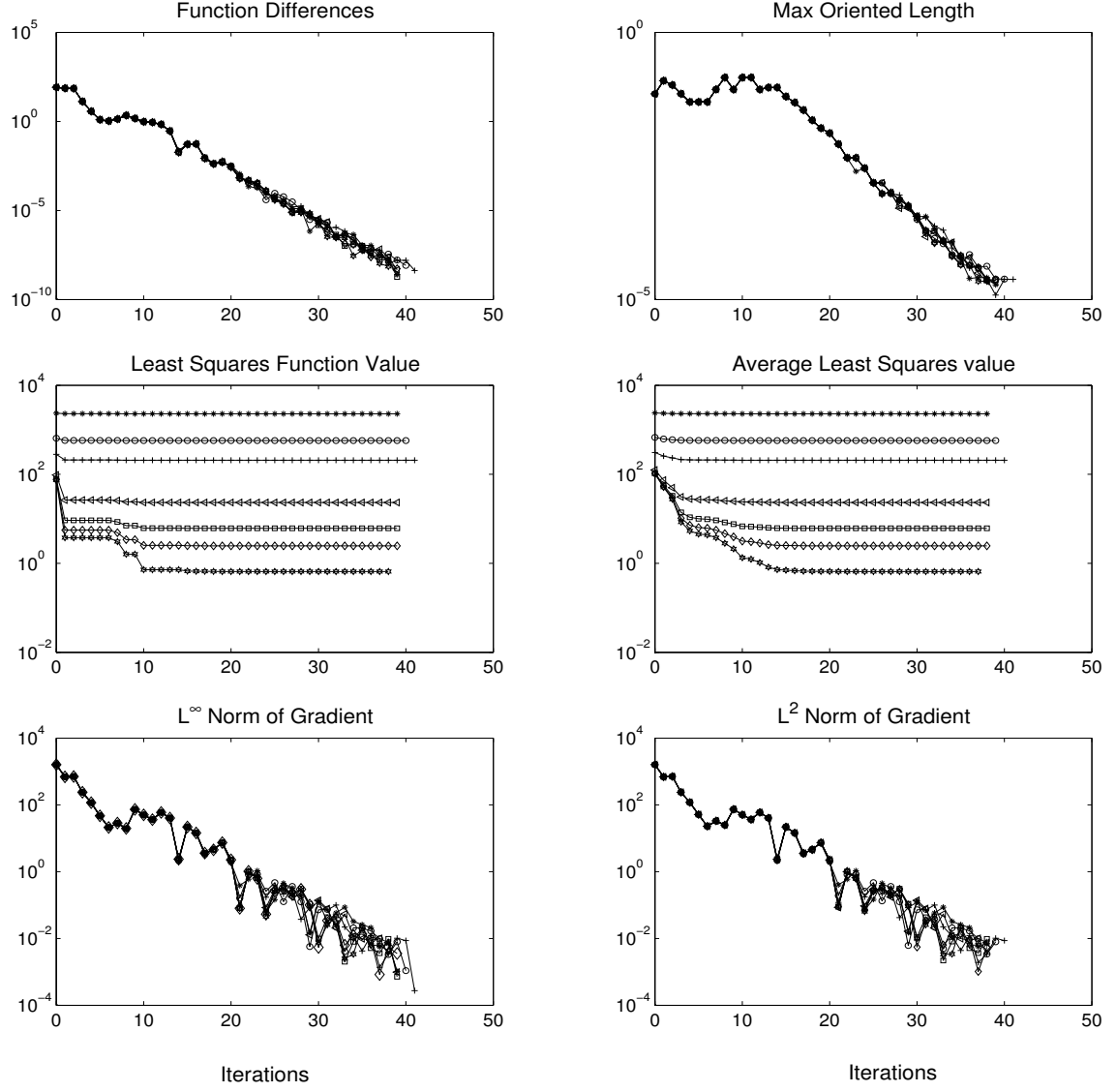
Figure 28: Nelder-Mead for the estimation of $\epsilon_{s,0}$ and κ_s for water. The other five parameters are fixed at the values given in (103) and relative noise of varying levels is added to the data. 0% (−), 1% (- -) 3% (o-) and 5% (+-)

Table 5: Parameter estimation of $\epsilon_{s,0}$ and κ_s for 0% - 10% added relative random noise. The values of the other five parameters are fixed at values given in (104).

% RN	Iter	$\hat{\epsilon}_{s,0}$	$\hat{\kappa}_s$	$|J^S_{n+1} - J^S_0|$	J^S	$||\nabla J^S||_{L^2}$	FC
0.0	38	80.2165	55.2945	1.5487×10^{-9}	0.4369	0.0013	73
0.1	38	80.2165	55.2949	7.2106×10^{-9}	0.6551	0.006310	75
0.3	39	80.2166	55.2946	5.4008×10^{-9}	2.4674	0.005495	76
0.5	39	80.2167	55.2939	1.8372×10^{-9}	6.1140	0.009746	76
1.0	39	80.2169	55.2914	4.5901×10^{-9}	23.2556	0.0075	76
3.0	41	80.2173	55.2826	4.2341×10^{-9}	206.4680	0.0087	78
5.0	40	80.2178	55.2729	8.2103×10^{-9}	573.1135	0.0079	78
10.0	39	80.2191	55.2509	2.5361×10^{-9}	2292.24730	0.00701	76

Figure 29: Plots of $\hat{\epsilon}_{s,0}$ (left) and $\hat{\kappa}_s$ (right) against the number of iterations for simulations in which the other five parameters are fixed at values that have 10%-50% relative error from the true values as given in (104), and relative noise of varying levels is added to the data.

Figure 30: Nelder-Mead for the estimation of $\epsilon_{s,0}$ and κ_s for water. The other five parameters are fixed at the values in (104), and relative random noise of varying levels is added to the data.

We next attempt the inverse problem with simulated data to which we add constant variance noise. We would like to compare the results of this case with the results obtained from the inverse problem by adding relative random noise to the simulated data. We use the notion of signal to noise ratio to make such comparisions.

6.2 Signal to noise ratio

In analog and digital communications, the signal to noise ratio, denoted as SNR, is a measure of the signal strength relative to the background noise. The ratio is usually measured in decibels (dB). There are many equivalent ways of defining the SNR [JN84]. Since we assume the mean of our noise to be zero, we define the SNR as

$$
\text{SNR} = 10\log_{10}\left(\frac{\sum_{k=1}^{M}|E_k^*|^2}{\sum_{k=1}^{M}\text{var}(O_k - E_k^*)}\right) \quad \text{dB}, \tag{105}
$$

where dB denotes decibels. If the signal strength is equal to the variance of the background noise, i.e.,

$$
\sum_{k=1}^{M}|E_k^*|^2 = \sum_{k=1}^{M}\text{var}(O_k - E_k^*) \tag{106}
$$

then SNR = 0, and the signal is almost unreadable, as the noise level severely competes with it. Ideally, the strength of the signal is greater than the variance of the noise, so that the SNR is positive which results in the signal being readable. If the strength of the signal is less than the variance of the noise, then the SNR is negative. Communications engineers always strive to maximize the SNR ratio. The SNR ratio can be increased by providing the source with a higher level of signal output power if necessary. In wireless systems, it is always important to optimize the performance of the transmitting and receiving antennas.

Using the notation presented in Section 5, the SNR in the cases of relative random noise SNR_R and constant variance noise SNR_C are, respectively, given as

$$
\text{SNR}_R = 10\log_{10}\left(\frac{\sum_{k=1}^{M}|E_k^*|^2}{\sum_{k=1}^{M}\text{var}(\nu E_k^* \eta_k)}\right) \quad \text{dB},
$$

$$
\text{SNR}_C = 10\log_{10}\left(\frac{\sum_{k=1}^{M}|E_k^*|^2}{\sum_{k=1}^{M}\text{var}(\beta \eta_k)}\right) \quad \text{dB}
\tag{107}
$$

To compare the case of constant variance noise with the case of relative random noise, we proceed as follows.

1. As noted in (79) and the discussion thereafter, we set $\beta = \nu\alpha$. Setting the SNR

Table 6: Comparison of relative random noise and constant variance noise

SNR (dB)	ν	% RN	$\beta = \nu\alpha$
66	0.0005	0.1	0.0118
56	0.0015	0.3	0.0353
52	0.0025	0.5	0.0588
46	0.005	1.0	0.1175
36	0.015	3.0	0.3526
32	0.025	5.0	0.5877
26	0.05	10.0	1.1754

in the two cases to be equal i.e., $\mathrm{SNR_R} = \mathrm{SNR_C}$, implies

$$\sum_{k=1}^{M} \mathrm{var}(\nu E_k^* \eta_k) = M\nu^2\alpha^2 \implies \alpha = \sqrt{\frac{\sum_{k=1}^{M} |E_k^*|^2}{M}}. \tag{108}$$

2. Thus for a given value of ν, we have $\beta = \alpha\nu$ and the corresponding SNR is calculated as

$$\mathrm{SNR_R} \equiv \mathrm{SNR_C} = 10\log_{10}\left(\frac{\sum_{k=1}^{M} |E_k^*|^2}{M\alpha^2\nu^2}\right) = 10\log_{10}\left(\frac{1}{\nu^2}\right). \tag{109}$$

Hence, for each value of ν there is a corresponding value of β for which the SNR for relative random noise is equivalent to the SNR for constant variance noise. In Table 6 we present the values of the SNR, β, and ν that correspond to each other in the manner described above. For this test problem $\alpha = 23.5077$.

We next attempt to identify the two parameters $\epsilon_{s,0}$ and κ_s by adding constant variance noise as given in (79) to our data and using the fixed values (104). The results for the corresponding inverse problem are presented in Table 7. The results in this case are quite different from the case of relative noise as shown in Table 5. We can see that the estimation of κ_s becomes worse as the level of noise increases. The estimation of $\epsilon_{s,0}$ on the other hand is relatively stable, though it is not as accurate as the estimate obtained in the case where relative noise is added to the data. The estimates also become worse as the level of constant variance noise increases. In Table 7, ν corresponds to the scaling factor in (78). The constant variance case and the relative noise case for the same value of ν have the same signal to noise ratio. Figure 31 plots the variation of $\hat{\epsilon}_{s,0}$ and $\hat{\kappa}_s$ over all iterations. As can be seen here the value of $\hat{\kappa}_s$ increases, away from the true value, as the noise level increases. Figure 32 plots the details of the corresponding Nelder-Mead Simulation.
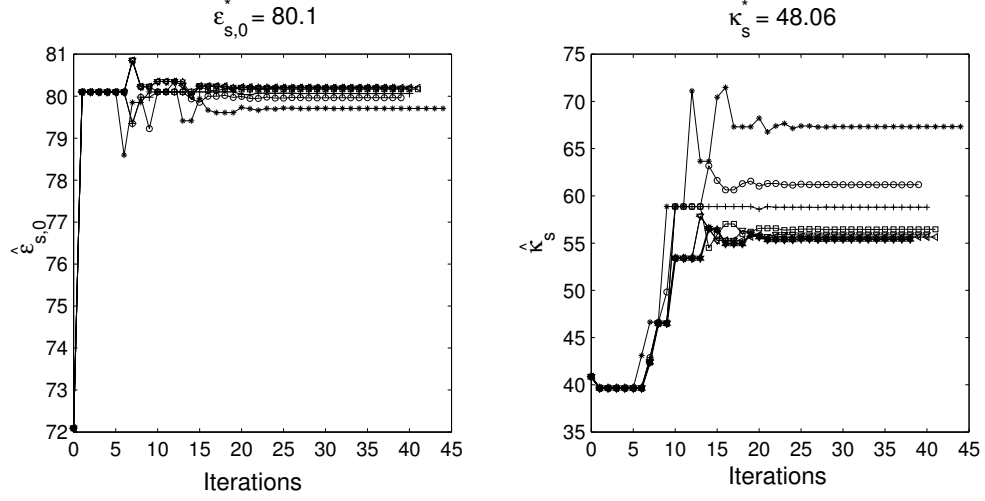
Figure 31: Plots of $\hat{\epsilon}_{s,0}$ (left) and $\hat{\kappa}_s$ (right) against the number of iterations for simulations in which the other five parameters are fixed at values that have 10%-50% relative error from the true values as given in (104), and constant variance noise corresponding to varying levels of relative noise is added to the data.

Table 7: Parameter estimation of $\epsilon_{s,0}$ and κ_s for 0%-10% constant variance noise. The other five parameters are fixed at the values given in (104)

% RN	Iter	$\hat{\epsilon}_{s,0}$	$\hat{\kappa}_s$	$|J_{n+1}^S - J_0^S|$	J^S	$||\nabla J^S||_{L^2}$	FC
0.0	38	80.2165	55.2945	1.5487×10^{-9}	0.4369	0.0013	73
0.1	38	80.2114	55.4112	8.1590×10^{-9}	0.6973	0.01237	74
0.3	41	80.2012	55.6422	9.6609×10^{-9}	2.8205	0.001064	77
0.5	40	80.1910	55.8728	8.1572×10^{-9}	7.0804	0.0005887	77
1.0	41	80.1654	56.4531	3.1244×10^{-9}	27.0778	0.007561	82
3.0	40	80.0636	58.7953	9.7228×10^{-9}	240.6053	0.01135	77
5.0	39	79.9621	61.1779	7.8005×10^{-9}	667.7927	0.0111	79
10.0	44	79.7084	67.3235	3.5288×10^{-10}	2670.5115	0.007417	85

Table 8: Confidence Intervals for the parameter estimation of $\epsilon_{s,0}$ and κ_s for constant variance noise with the Nelder-Mead algorithm.

	RN = 0.0%
$\hat{\epsilon}_{s,0}$	$(8.02165 \pm 1.8804 \times 10^{-3}) \times 10$
$\hat{\kappa}_s$	$(5.52945 \pm 1.6448 \times 10^{-2}) \times 10$
	RN = 0.1%
$\hat{\epsilon}_{s,0}$	$(8.02114 \pm 2.3718 \times 10^{-3}) \times 10$
$\hat{\kappa}_s$	$(5.54112 \pm 2.0745 \times 10^{-2}) \times 10$
	RN = 0.3%
$\hat{\epsilon}_{s,0}$	$(8.02012 \pm 4.7554 \times 10^{-3}) \times 10$
$\hat{\kappa}_s$	$(5.56422 \pm 4.1583 \times 10^{-2}) \times 10$
	RN = 0.5%
$\hat{\epsilon}_{s,0}$	$(8.01910 \pm 7.5113 \times 10^{-3}) \times 10$
$\hat{\kappa}_s$	$(5.58728 \pm 6.5668 \times 10^{-2}) \times 10$
	RN = 1.0%
$\hat{\epsilon}_{s,0}$	$(8.01654 \pm 1.4577 \times 10^{-2}) \times 10$
$\hat{\kappa}_s$	$(5.64531 \pm 1.2738 \times 10^{-1}) \times 10$
	RN = 3.0%
$\hat{\epsilon}_{s,0}$	$(8.00636 \pm 4.2160 \times 10^{-2}) \times 10$
$\hat{\kappa}_s$	$(5.87953 \pm 3.6783 \times 10^{-1}) \times 10$
	RN = 5.0%
$\hat{\epsilon}_{s,0}$	$(7.99621 \pm 6.8206 \times 10^{-2}) \times 10$
$\hat{\kappa}_s$	$(6.11779 \pm 5.9447 \times 10^{-1}) \times 10$
	RN = 10.0%
$\hat{\epsilon}_{s,0}$	$(7.97084 \pm 1.2723 \times 10^{-1}) \times 10$
$\hat{\kappa}_s$	$(6.73235 \pm 1.1076) \times 10$

We now calculate confidence intervals for the estimates that we obtained in Table 7. The procedure for calculating these intervals was outlined in Section 4.1. These intervals are presented in Table 8 for varying levels of noise. From our earlier discussion about confidence intervals, we note that the size of the intervals is in direct proportion to the level of uncertainty that we have about the estimates that we have obtained. Thus, the smaller the confidence interval the more confident we are about the estimates obtained. As we can see from Table 8 we have tighter intervals for the estimates of $\epsilon_{s,0}$ than we do for the estimates of κ_s, which is expected as our problem is more sensitive to $\epsilon_{s,0}$ than it is to the pressure coefficient κ_s. We also notice that the intervals become larger as the level of noise that is added to the data is increased. These intervals correspond to a 95% confidence level.
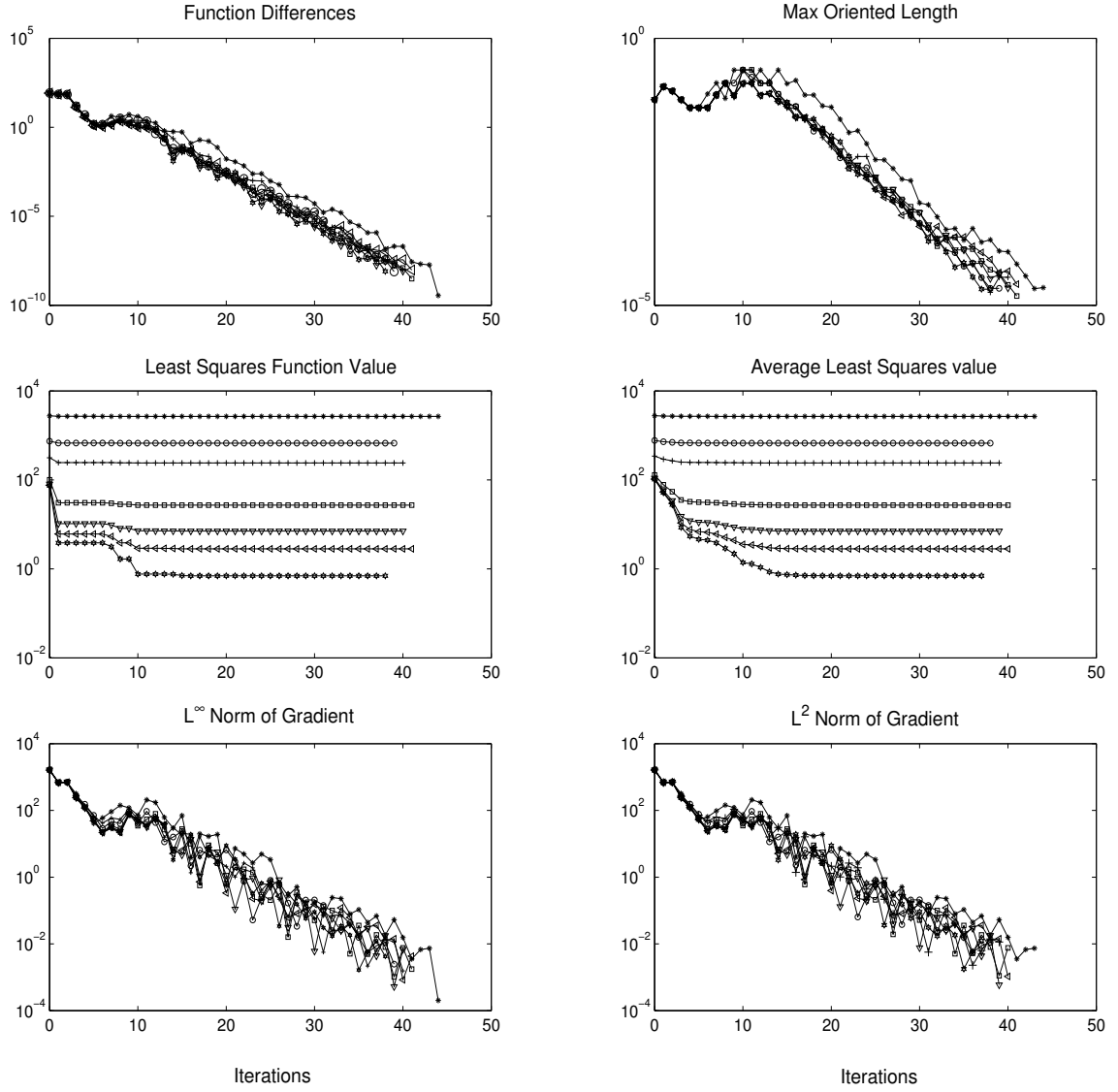
Figure 32: Nelder-Mead for the estimation of $\epsilon_{s,0}$ and κ_s for water. The other five parameters are fixed at the values given in (104), and constant variance noise corresponding to varying levels of relative noise is added to the data.
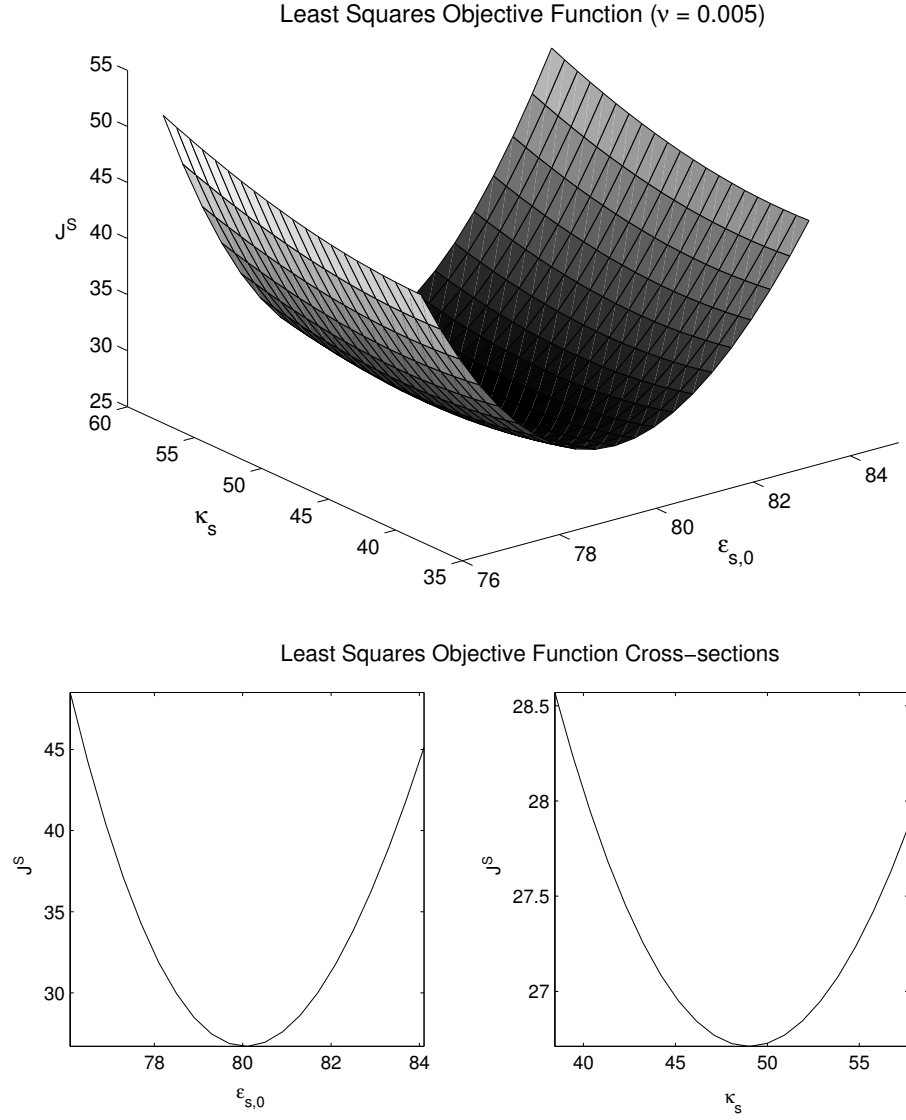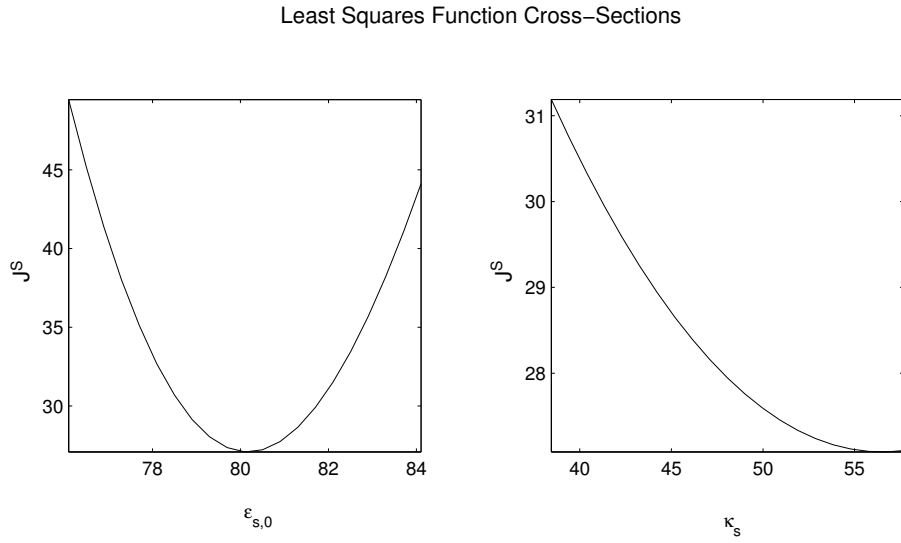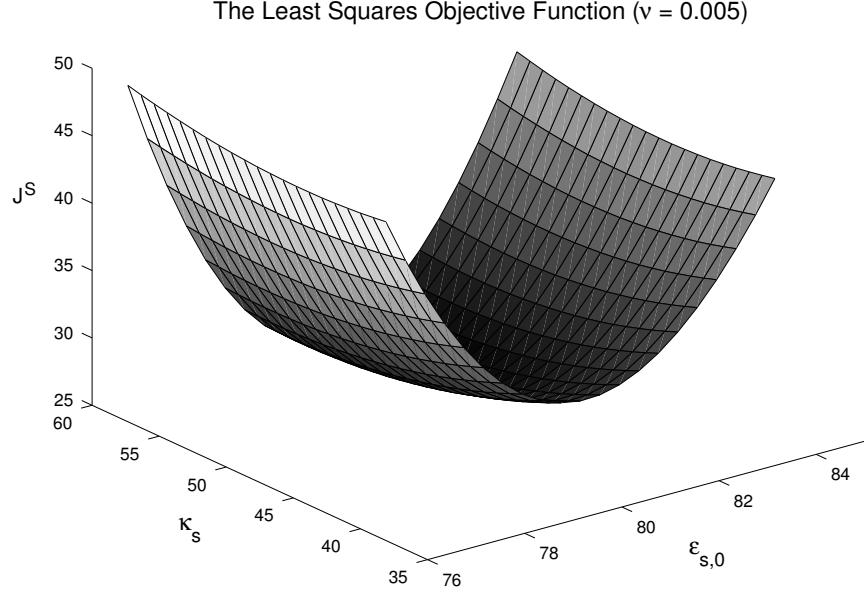
Figure 33: (Top) The Least Squares Objective Function for different values of $\epsilon_{s,0}$ and κ_s. Constant variance noise with $\nu = 0.005$ (1% RN) is added to the data. The other five parameters were fixed at their true values. The minimum for this plot is located at the point $(80.099, 49.0212)$, with a minimum value of 26.712. (Bottom) Cross sections of the Least Squares Objective function versus κ_s (left) and versus $\epsilon_{s,0}$ (right).

Figure 34: (Top) The Least Squares Objective Function for different values of $\epsilon_{s,0}$ and κ_s. Constant variance noise with $\nu = 0.005$ (1% RN) is added to the data. The other five parameters were fixed at the values given in (104). The minimum is located at the point $(80.099, 56.7108)$, with a minimum value of 27.0837. (Bottom) Cross sections of the Least Squares Objective function versus κ_s (left) and versus $\epsilon_{s,0}$ (right).
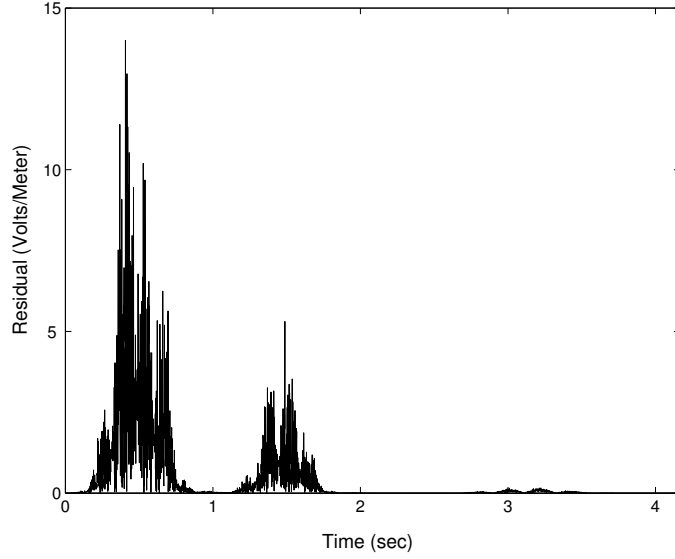
Figure 35: Plot of the Least Squares residual versus time in the case of 10% relative random noise added to the data.

In Figure 33 we plot the least squares objective function for values of $\hat{\epsilon}_{s,0}$ that have up to 5% relative error from the true values, and values of $\hat{\kappa}_s$ that have up to 20% relative error from the true values. The other five parameters were fixed at their true values in the case of the top plot in Figure 33 and at the values (104) in the case of the bottom plot, respectively. In Figure 34 the top and bottom plots show the the cross sections of the objective function against $\hat{\epsilon}_{s,0}$, and $\hat{\kappa}_s$ across the minimum with respect to the other variable, for the surface plots in Figure 33. Comparing with Figure 25 we observe that the minimum value of $\hat{\kappa}_s$ has moved away from its true value.

In Figures 35 we plot the least squares residual versus time in the case when 10% relative random noise is added to the data. A magnified plot of the least squares residual versus time in the interval where the acoustic reflection is observed is plotted in Figure 36. Finally we plot the least squares residual versus the absolute value of the electric field data in Figure 37 again in the case where 10% relative random noise is added to the data. We notice in this figure that the amount of noise increases as the absolute value of the electric field data magnitude increases. This is in direct contrast to the case when constant variance noise is added to the simulated data. We plot analogous plots of the least squares residual for 10% added constant variance noise in Figures 38 and 39. Comparing Figures 38 and 35 we note the lack of any patterns in the residual in Figure 38 for the case of added constant variance noise; whereas in Figure 35, the residual follows the peaks in the simulated data used in
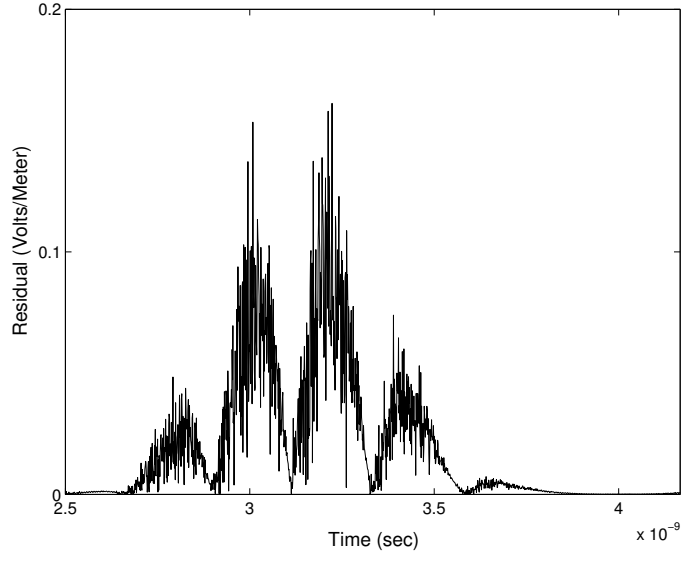
Figure 36: A magnified plot of the Least Squares residual versus time in the interval where the acoustic reflection is observed, for the case of 10% relative random noise added to the data.
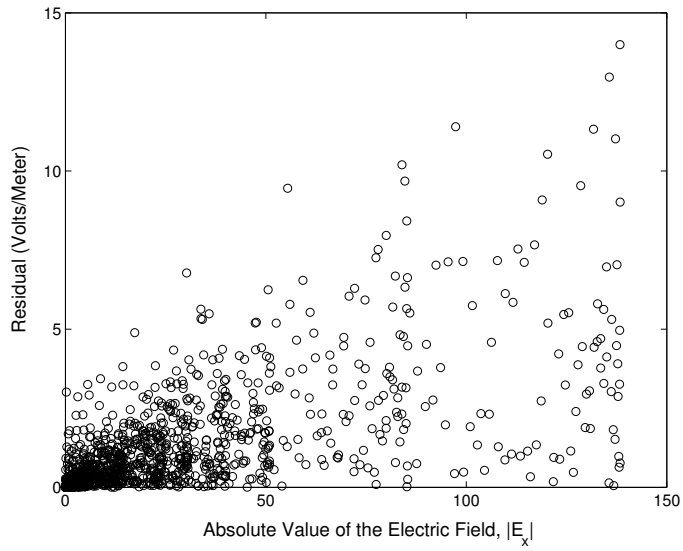

Figure 37: Plot of the Least Squares residual versus the absolute value of the electric field data for the case of 10% relative random noise added to the data.
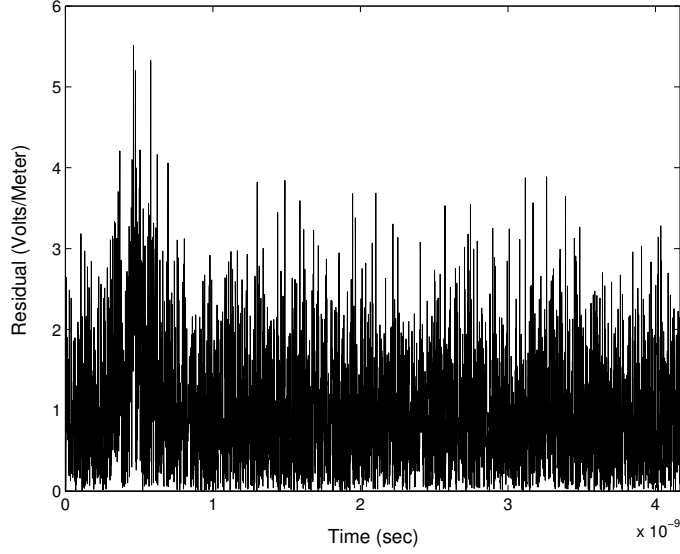
Figure 38: Plot of the Least Squares residual versus time for the case of constant variance noise added to the simulated data.

the inverse problem. Again in Figure 37 we note the fan like structure of the residual with the residual increasing with the absolute value of the electric field. In the case of added constant variance noise, however, we again note the lack of a pattern in the residual as seen in Figure 39. We also observe that there are many points of the residual on the line $E_x = 0$. This is beacuse in the simulated data, the electric field magnitude is almost zero most of the time. We compare the simulated data with added relative random noise and added constant variance noise in Figures 40-43. We notice in Figure 43 that the acoustic reflection is drowned by the constant variance noise with $\nu = 0.05$ (10% RN), which is not the case with the relative random noise data for the same value of ν. Thus the identification of κ_s is more difficult with constant variance noise added to the simulated data.

We next attempt the identification of three parameters, namely $\epsilon_{s,0}$, τ_0 and κ_s. The other four parameters, $\epsilon_{\infty,0}$, σ, κ_∞ and κ_τ are fixed at values given in (104). Tables 9 and 10 present the final estimates and the details of the corresponding Nelder-Mead simulation. We observe that the final estimates for both τ_0 and κ_s start to increase away from their true values as the level of constant variance noise is increased. The plots of the least squares objective function presented before provide an explanation for this. In Figures 45-44 we plot the variation of the three parameters over all iterations in the Nelder-Mead simulation. In each of these figures the dashed line represents the true value of the corresponding parameter. Again, we observe that the estimates for $\epsilon_{s,0}$ are stable with respect to the level of constant variance noise,
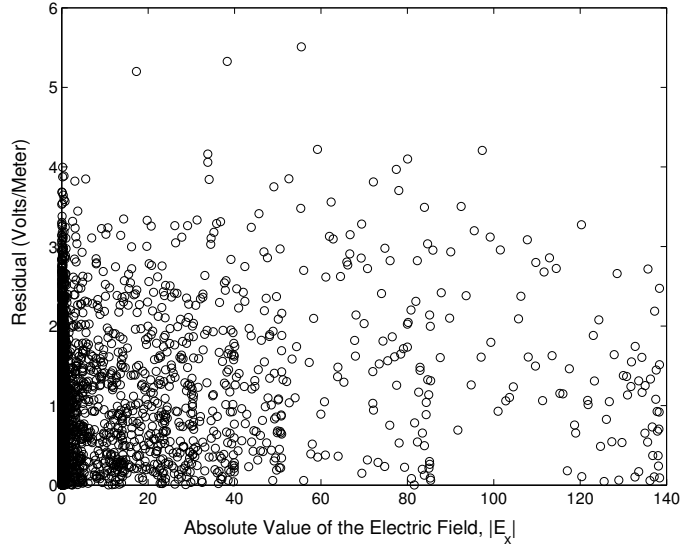
64

Figure 39: Plot of the Least Squares residual versus the absolute value of the electric field for the case of constant variance noise added to the simulated data.

however, the estimates for τ_0 and κ_s increase as the value of ν is increased.

Table 9: Parameter estimation of $\epsilon_{s,0}$ and τ_0 and κ_s for constant variance noise, corresponding to varying levels of relative noise with the Nelder-Mead algorithm.

% RN	Iter	$\hat{\epsilon}_{s,0}$	$\hat{\tau}_0(\times 10^{-12})$	$\hat{\kappa}_s$
0.0	78	80.1069	8.1543	48.2026
0.1	81	80.1033	8.1627	48.3386
0.3	75	80.0959	8.1768	48.6725
0.5	81	80.0890	8.1919	48.9905
1.0	90	80.0745	8.2242	49.8265
3.0	79	80.0076	8.3635	53.1810
5.0	99	79.9315	8.5015	56.7926
10.0	83	79.7087	8.8299	66.2803

65
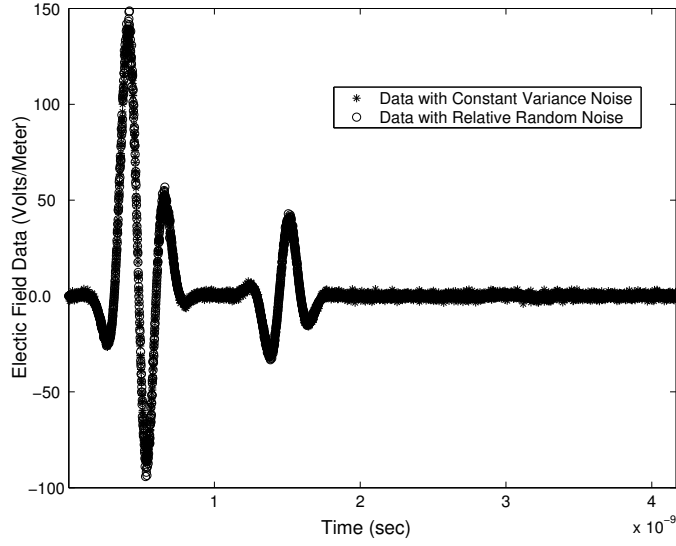
Figure 40: Comparison of the data with added relative random noise to the data with constant variance noise added. The value of ν in both the cases is $\nu = 0.05$ (10% RN).
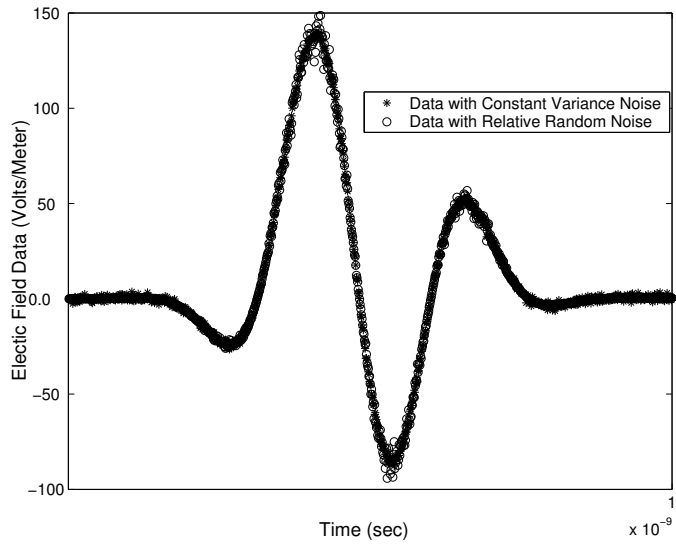
Figure 41: Comparison of the data with added relative random noise to the data with constant variance noise added for the input signal at the center of the antenna. The value of ν in both the cases is $\nu = 0.05$ (10% RN).
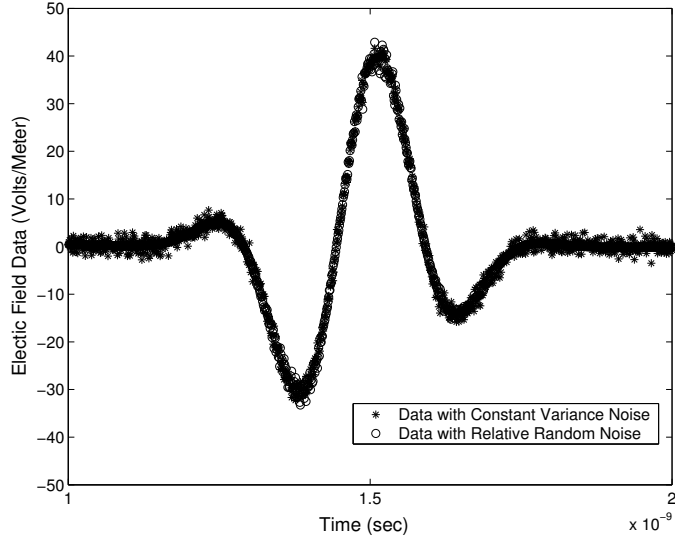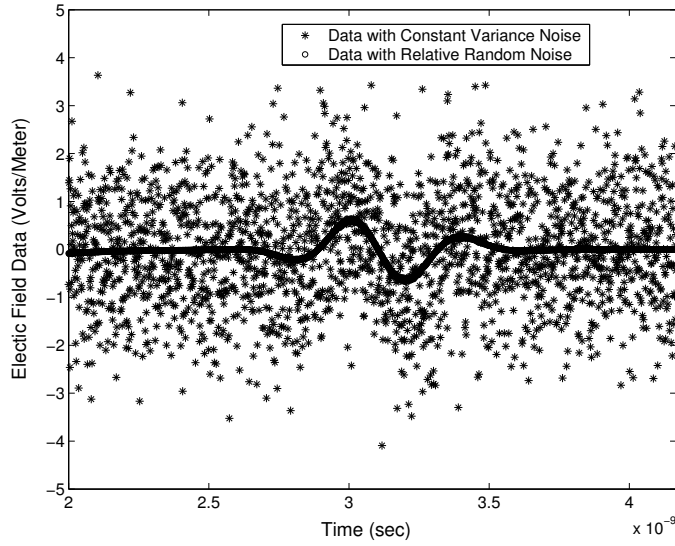
Figure 42: Comparison of the data with added relative random noise to the data with constant variance noise added for the first reflection from the air-Debye interface. The value of ν in both the cases is $\nu = 0.05$ (10% RN).

Figure 43: Comparison of the data with added relative random noise to the data with constant variance noise added for the reflection from the acoustic wave region. The value of ν in both the cases is $\nu = 0.05$ (10% RN).

67
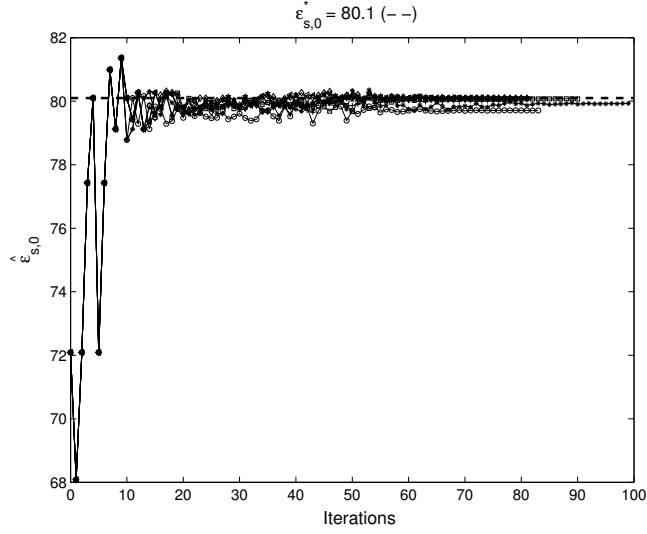
Figure 44: Estimation of $\epsilon_{s,0}$ by the Nelder-Mead algorithm. We plot the variation of $\hat{\epsilon}_{s,0}$ with the iteration count.

Table 10: Parameter estimation of $\epsilon_{s,0}$ and τ_0 and κ_s for constant variance noise, corresponding to varying levels of relative noise with the Nelder-Mead algorithm.

% RN	$||\nabla J^S||_{L^2}$	FC	$|J^S_{n+1} - J^S_0|$	J^S
0.0	0.008942	140	8.02867×10^{-9}	4.4391×10^{-5}
0.1	0.00224	144	4.3059×10^{-9}	0.2672
0.3	0.00499	136	5.9737×10^{-9}	2.4039
0.5	0.0139	150	3.5686×10^{-9}	6.6771
1.0	0.001414	161	8.5522×10^{-9}	26.7071
3.0	0.0277	147	9.0774×10^{-9}	240.3553
5.0	0.007697	181	6.7874×10^{-9}	667.6441
10.0	0.001432	154	6.2983×10^{-9}	2670.5056

In the case of the estimation of three parameters we observe that the estimates of κ_s are more accurate when τ_0 is allowed to vary as opposed to the case of two parameter estimation when τ_0 is fixed at a particular value. Varying τ_0, however, does not seem to make much difference in estimating $\epsilon_{s,0}$. Also, comparing the intervals in Tables 8 and 11 we find that we obtain tighter confidence intervals for the three parameter case as opposed to the two parameter case, for the same level of
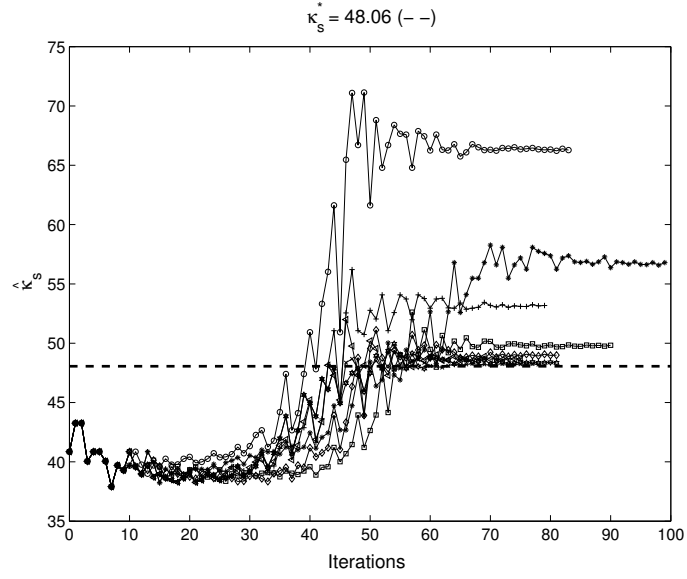
Figure 45: Estimation of κ_s by the Nelder-Mead algorithm. We plot the variation of $\hat{\kappa}_s$ with the iteration count.
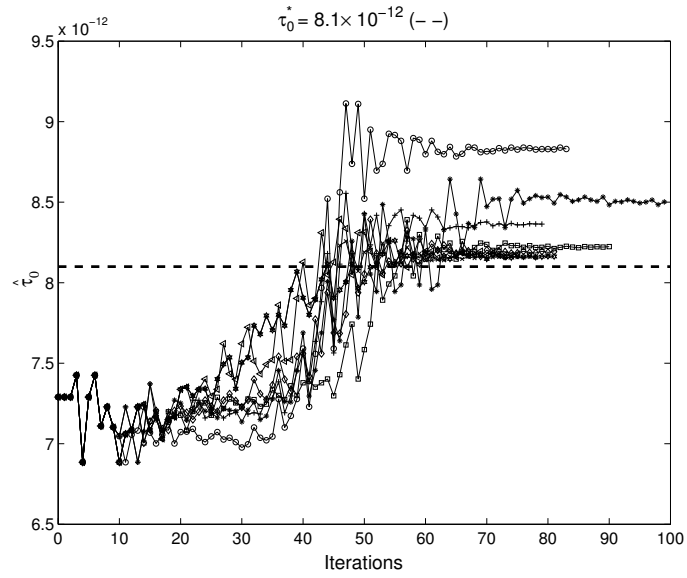

Figure 46: Estimation of τ_0 by the Nelder-Mead algorithm. We plot the variation of $\hat{\tau}_0$ with the iteration count.

Table 11: Confidence Intervals for the parameter estimation of $\epsilon_{s,0}$, τ_0 and κ_s for constant variance noise with the Nelder-Mead algorithm.

RN	0.0%
$\hat{\epsilon}_{s,0}$	$(8.01069 \pm 1.8738 \times 10^{-5}) \times 10$
$\hat{\tau}_0$	$(8.1543 \pm 2.3240 \times 10^{-4}) \times 10^{-12}$
$\hat{\kappa}_s$	$(4.82026 \pm 2.6832 \times 10^{-4}) \times 10$
RN	0.1%
$\hat{\epsilon}_{s,0}$	$(8.01033 \pm 1.4526 \times 10^{-3}) \times 10$
$\hat{\tau}_0$	$(8.1627 \pm 1.8004 \times 10^{-2}) \times 10^{-12}$
$\hat{\kappa}_s$	$(4.83386 \pm 2.0798 \times 10^{-2}) \times 10$
RN	0.3%
$\hat{\epsilon}_{s,0}$	$(8.00959 \pm 4.3438 \times 10^{-3}) \times 10$
$\hat{\tau}_0$	$(8.1768 \pm 5.3824 \times 10^{-2}) \times 10^{-12}$
$\hat{\kappa}_s$	$(4.86725 \pm 6.2220 \times 10^{-2}) \times 10$
RN	0.5%
$\hat{\epsilon}_{s,0}$	$(8.00890 \pm 7.2206 \times 10^{-3}) \times 10$
$\hat{\tau}_0$	$(8.1919 \pm 8.9417 \times 10^{-2}) \times 10^{-12}$
$\hat{\kappa}_s$	$(4.89905 \pm 1.0345 \times 10^{-1}) \times 10$
RN	1.0%
$\hat{\epsilon}_{s,0}$	$(8.00745 \pm 1.4327 \times 10^{-2}) \times 10$
$\hat{\tau}_0$	$(8.2242 \pm 1.7739 \times 10^{-1}) \times 10^{-12}$
$\hat{\kappa}_s$	$(4.98265 \pm 2.0555 \times 10^{-1}) \times 10$
RN	3.0%
$\hat{\epsilon}_{s,0}$	$(8.00076 \pm 4.1809 \times 10^{-2}) \times 10$
$\hat{\tau}_0$	$(8.3635 \pm 5.1532 \times 10^{-1}) \times 10^{-12}$
$\hat{\kappa}_s$	$(5.31810 \pm 6.0160 \times 10^{-1}) \times 10$
RN	5.0%
$\hat{\epsilon}_{s,0}$	$(7.99315 \pm 6.7761 \times 10^{-2}) \times 10$
$\hat{\tau}_0$	$(8.5015 \pm 8.3067 \times 10^{-1}) \times 10^{-12}$
$\hat{\kappa}_s$	$(5.67926 \pm 9.7751 \times 10^{-1}) \times 10$
RN	10.0%
$\hat{\epsilon}_{s,0}$	$(7.97087 \pm 1.2738 \times 10^{-1}) \times 10$
$\hat{\tau}_0$	$(8.8299 \pm 1.5286) \times 10^{-12}$
$\hat{\kappa}_s$	$(6.62803 \pm 1.8366) \times 10$

added noise. The reason for this again is most likely the dependence of the acoustic reflections on the value of τ_0. Thus, the algorithm for the inverse problem can choose τ_0 appropriately so that the value of $\hat{\kappa}_s$ is minimized. As before, estimates for all three parameters become worse as the level of noise added is increased and the corresponding confidence intervals become larger as seen in Table 11.

In Figure 47 we plot the details of the Nelder-Mead simulation for the identification of the three parameters $\epsilon_{s,0}$, τ_0 and κ_s. In Figure 48 we plot the least squares objective function for values of τ_0 and $\hat{\kappa}_s$ that differ from the true values by up to 10%, in the case of added constant variance noise with $\nu = 0.05$ (10% RN). The other five parameters are fixed at the values given in (104) with $\epsilon_{s,0}$ fixed at the value 73.1. We observe that the minimum has moved away from the true values. The fact that the acoustic reflection is overshadowed by the constant variance noise as shown in Figure 43 explains this behaviour of the objective function.

6.3   Simulation Results: The Levenberg-Marquardt method

We now repeat our inverse problem with a different least squares optimization technique. The Nelder Mead method presented in the previous section is a gradient free method based on the use of simplices. We will now use a gradient based method, namely the Levenberg-Marquardt method to solve our inverse problem. For the overdetermined least squares objective function

$$\mathrm{J}^S(\mathbf{q}) = \frac{1}{2} \sum_{k=1}^{M} |E_x(t_k, 0, z_c; \mathbf{q}) - O_k^s|^2 = \frac{1}{2} R(\mathbf{q})^T R(\mathbf{q}), \tag{110}$$

Levenberg-Marquardt, which is a trust region method, adds a regularization parameter $\nu_{LM} > 0$ to the approximate Hessian of the Gauss-Newton method to obtain a new estimate $\mathbf{q}_c = \mathbf{q}_c + s$, where

$$s = -\left(\nu_{LM}I + R'(\mathbf{q}_c)^T R'(\mathbf{q}_c)\right)^{-1} R'(\mathbf{q}_c)^T R(\mathbf{q}_c), \tag{111}$$

with $\mathbf{q}_c$, the current estimate and I the $l \times l$ identity matrix, where l is the number of parameters that we are attempting to estimate. The matrix $\left(\nu_{LM}I + R'(\mathbf{q}_c)^T R'(\mathbf{q}_c)\right)$ is positive definite. The parameter ν_{LM} is called the Levenberg-Marquardt parameter. For details of this implementation of the Levenberg-Marquardt method we refer the reader to [Kel99].

As with Nelder-Mead, we first attempt the identification of all the seven parameters, then we identify $\epsilon_{s,0}$ and κ_s and finally we attempt the identification of $\epsilon_{s,0}$, τ_0 and κ_s. Figures 49-50 plot the final estimates for all the seven parameters and the details of the Levenberg-Marquardt simulation. The dashed lines here represent the true values of the corresponding parameter. Tables 12 and 13 present the results for the inverse problem of identifying the seven parameters. We observe how close the final estimates of the parameters here are with those computed by Nelder-Mead. We
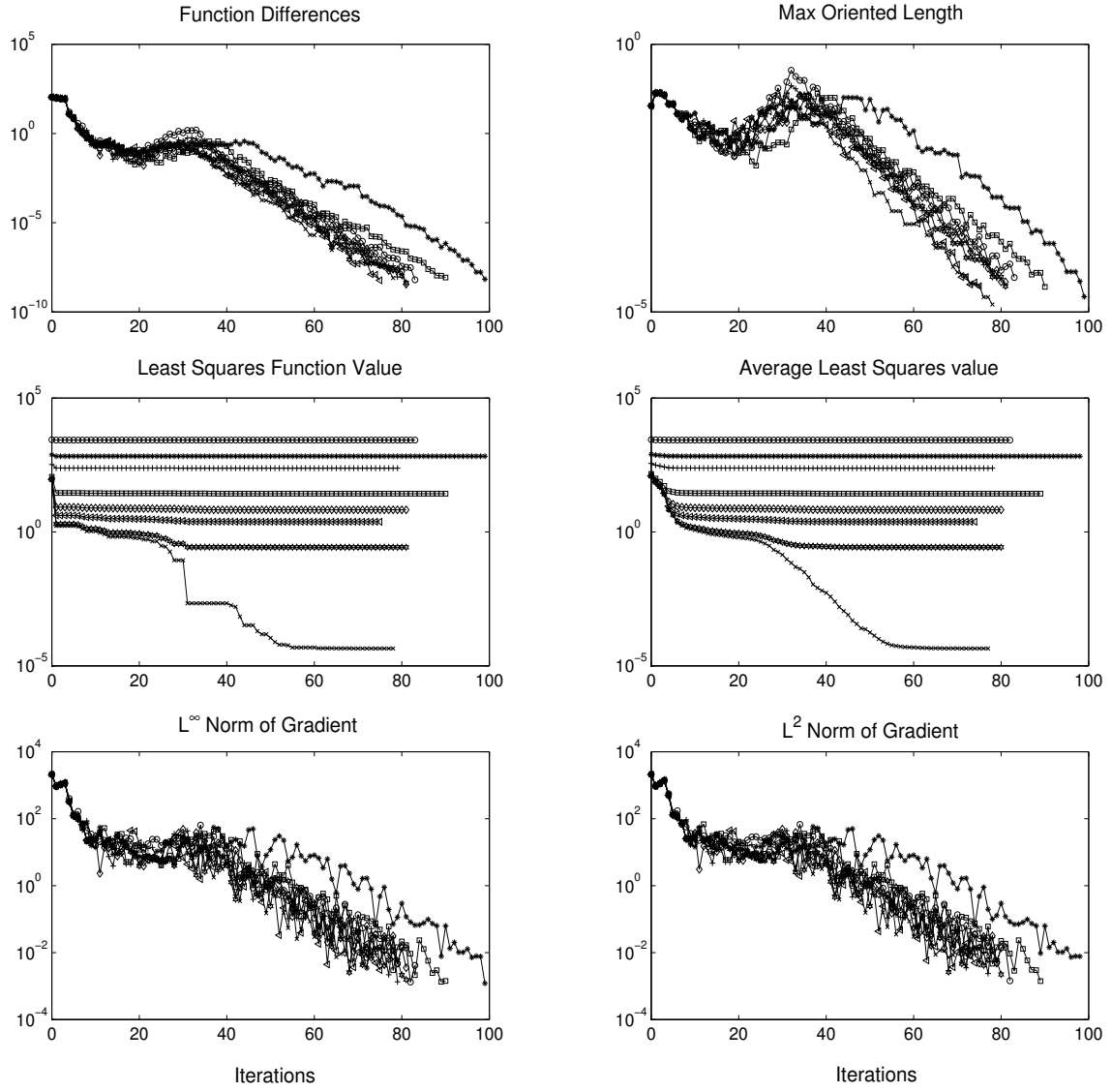
Figure 47: Nelder-Mead for the three parameter estimation problem for varying levels of constant variance noise.
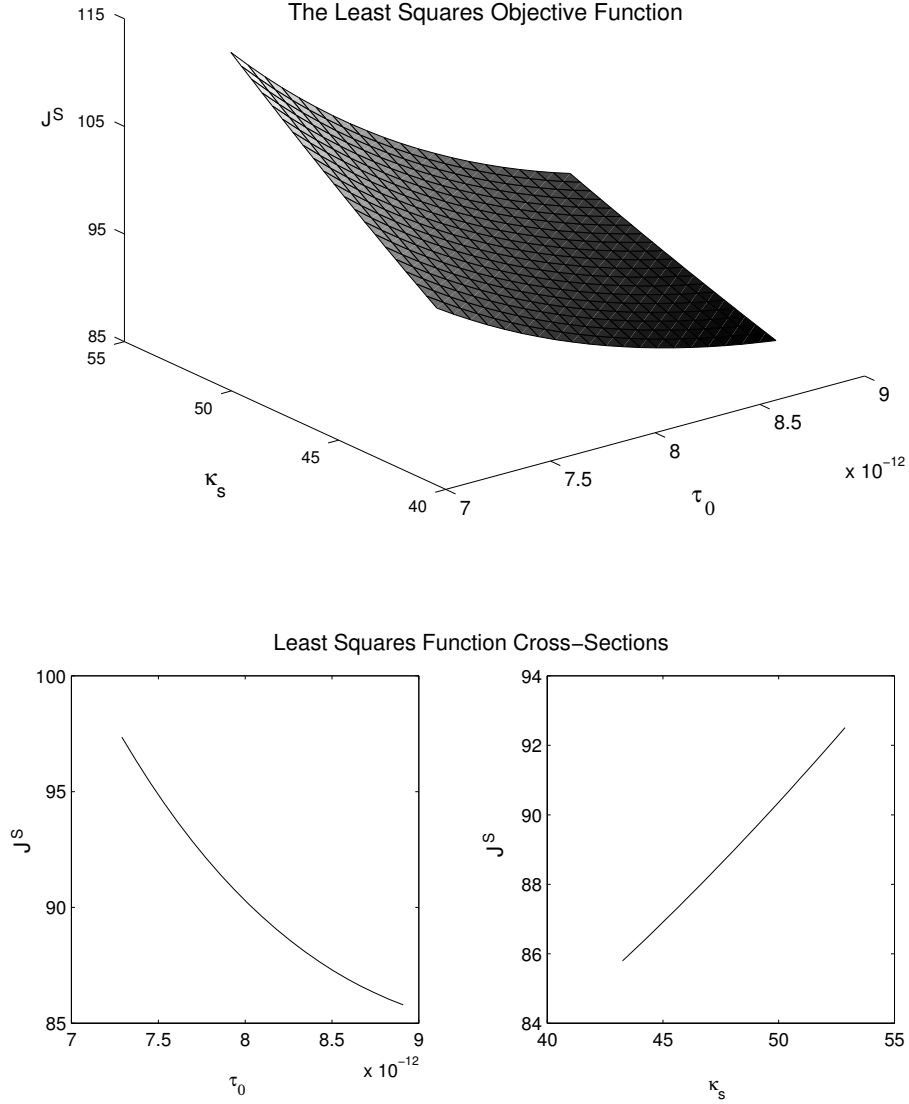
The Least Squares Objective Function

Least Squares Function Cross-Sections

Figure 48: (Top) The Least Squares Objective Function for different values of τ_0 and $\hat{\kappa}_s$. constant variance noise with $\nu = 0.005$ (1% RN) is added to the data. The other five parameters were fixed at the values given in (103) with $\epsilon_{s,0}$ fixed at the value 73.1. The minimum is located at the point $(8.91 \times 10^{-12}, 43.254)$, with a minimum value of 85.796. (Bottom) Plot of the Least Squares Objective function versus $\hat{\kappa}_s$ (left) and versus τ_0 (right).
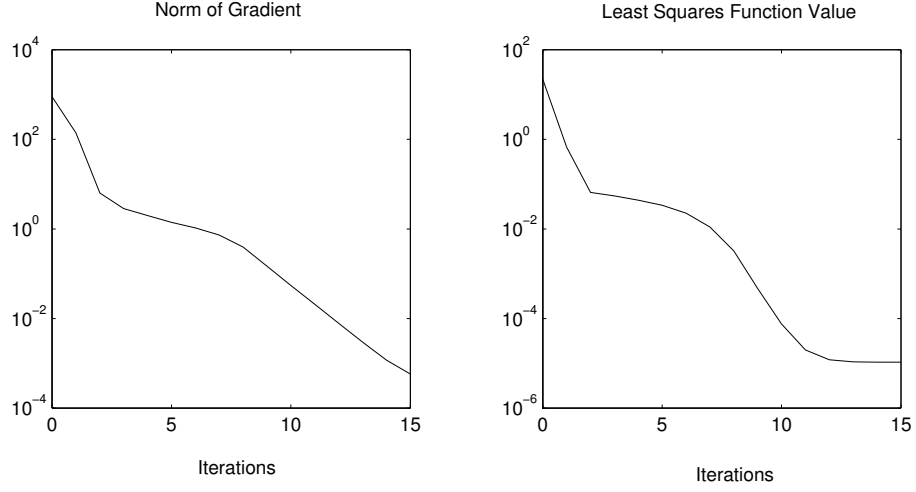
Figure 49: Levenberg-Marquardt for the seven parameter estimation problem
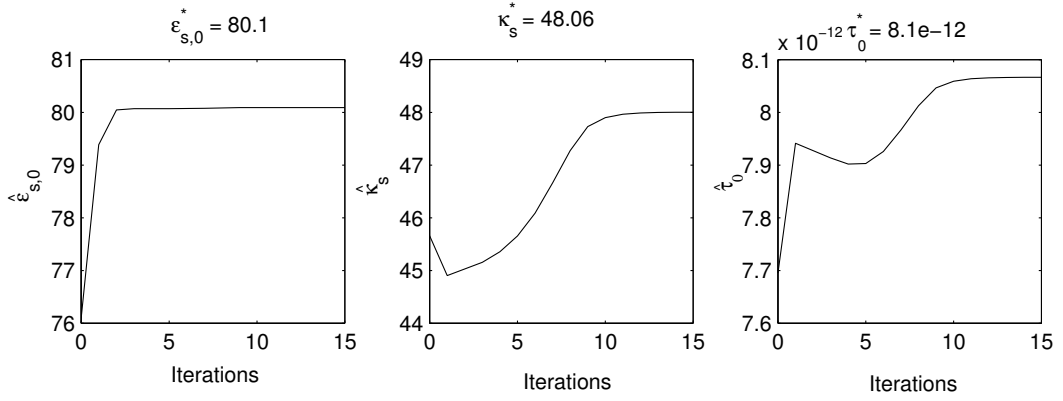
Figure 50: Estimation of $\epsilon_{s,0}$, τ_0 and κ_s by the Levenberg-Marquardt algorithm. We plot the variation of the three parameters with the iteration count.
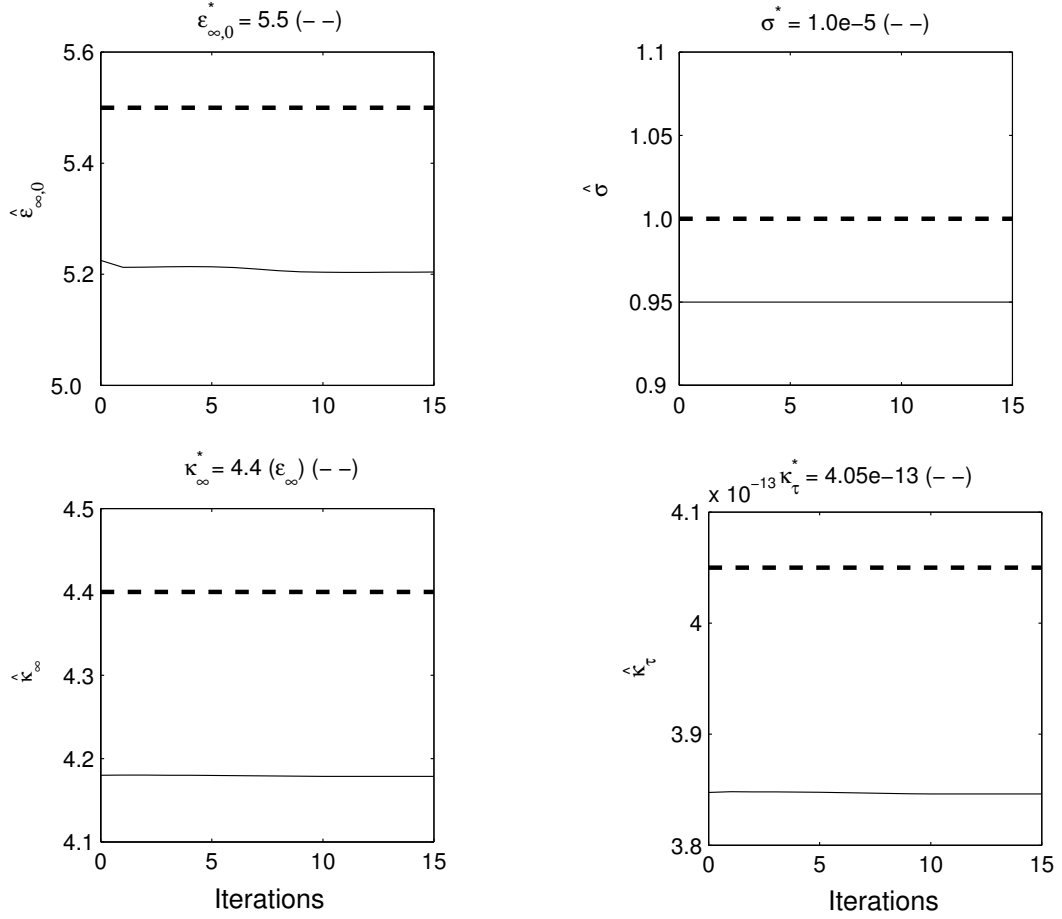
Figure 51: Levenberg-Marquardt for the seven parameter estimation problem. We plot the variation of the parameters with the iteration count. The dashed lines indicate the true values of the parameters, while the solid lines are the estimates over the iterations

Table 12: Final estimates for all seven parameters for water using Levenberg-Marquardt. The initial parameter set has values that are 5% smaller than the true values.

Parameter	True Values	Final Estimates
$\epsilon_{s,0}$	80.1	80.0917
$\epsilon_{\infty,0}$	5.5	5.2039
τ_0	$8.1e-12$	8.0666×10^{-12}
σ	1.0×10^{-5}	9.5×10^{-6}
$\hat{\kappa}_s$	48.06	48.0028
κ_∞	4.4	4.1786
κ_τ	4.05×10^{-13}	3.8462×10^{-13}

Table 13: Status of the Levenberg-Marquardt Simulation at the final iteration.

Least squares value	1.0584×10^{-5}
L^2 norm of the gradient	5.7248×10^{-4}
Number of forward solves	31
Number of gradient evaluations	16
Number of hessian evaluations	30

can again make similar conclusions as we did in the case of the Nelder-Mead results. Only $\epsilon_{s,0}$, τ_0 and κ_s seem to be identifiable with some accuracy, whereas the problem appears to be insensitive to changes in the other four parameters. We next attempt the identification of $\epsilon_{s,0}$ and κ_s with simulated data in which constant variance noise is added. The values of the remaining five parameters are fixed at those in (104). Tables 14 and 15 present the final estimates and the details of the corresponding LM simulation. In Figures 52 and 53 we plot the details of the LM run as well as the variation of $\hat{\epsilon}_{s,0}$ and $\hat{\kappa}_s$ over all iterations. The confidence intervals for these estimates are presented in Table 16. Again, we can make similar remarks and observations as in the case of the results of the Nelder-Mead method.

Finally we attempt to identify the three parameters $\epsilon_{s,0}$, τ_0 and κ_s. Figures 55 and 54 plot the details of the LM simulation and the variation of the parameters over all iterations. Tables 17 and 18 present the final estimates and details of the algorithm. Again, as was observed in the results of the Nelder-Mead runs, the estimates for κ_s are better when the value of τ_0 is kept variable as opposed to fixing the value of τ_0. Thus, the inverse problem captures κ_s more accurately if the value of τ_0 is allowed to change. In Table 19 we present the confidence intervals for the three parameter

Table 14: Parameter estimation of $\epsilon_{s,0}$ and κ_s for constant variance noise, corresponding to varying levels of relative noise with the Levenberg-Marquardt algorithm.

% RN	Iter	$\hat{\epsilon}_{s,0}$	$\hat{\kappa}_s$	J^S	$||\nabla J^S||_{L^2}$
0.0	18	80.2166	55.2951	0.4369	0.0006526
0.5	18	80.191	55.8726	7.0804	0.0071
1.0	18	80.1654	56.4524	27.0778	0.00076
3.0	18	80.0636	58.7948	240.6053	0.001068
5.0	18	79.9621	61.1765	667.7927	0.001385
10.0	19	79.7084	67.3217	2670.5115	0.001417

Table 15: Parameter estimation of $\epsilon_{s,0}$ and κ_s for constant variance noise, corresponding to varying levels of relative noise with the Levenberg-Marquardt algorithm.

% RN	Iter	J^S	$||\nabla J^S||_{L^2}$	F	G	H
0.0	18	0.4369	0.0006526	37	19	36
0.5	18	7.0804	0.0071	37	19	36
1.0	18	27.0778	0.00076	37	19	36
3.0	18	240.6053	0.001068	37	19	36
5.0	18	667.7927	0.001385	37	19	36
10.0	19	2670.5115	0.001417	39	20	38
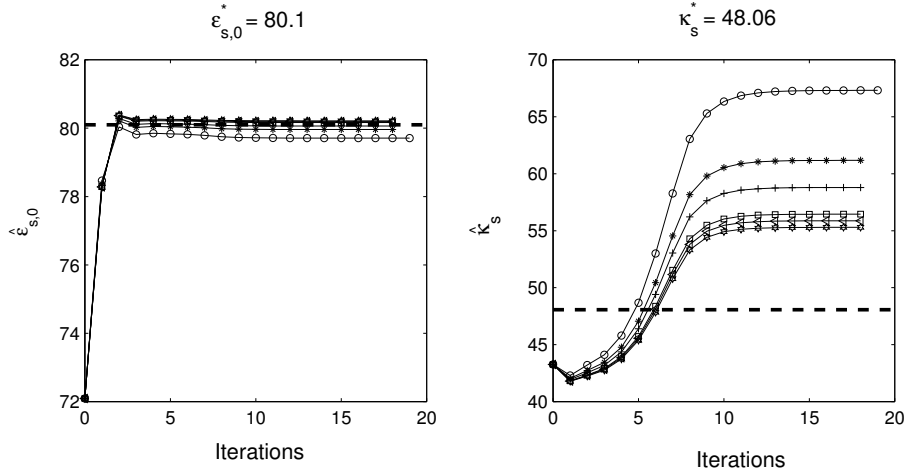
Figure 52: Levenberg-Marquardt for the two parameter estimation problem. Variation of $\hat{\epsilon}_{s,0}$ (left) and $\hat{\kappa}_s$ (right) over the iteration count.

Table 16: Confidence Intervals for the parameter estimation of $\epsilon_{s,0}$ and κ_s for constant variance noise with the Levenberg-Marquardt algorithm.

	RN = 0.0%
$\hat{\epsilon}_{s,0}$	$(8.02166 \pm 1.8803 \times 10^{-3}) \times 10$
$\hat{\kappa}_s$	$(5.52951 \pm 1.6448 \times 10^{-2}) \times 10$
	RN = 0.5%
$\hat{\epsilon}_{s,0}$	$(8.01910 \pm 7.5113 \times 10^{-3}) \times 10$
$\hat{\kappa}_s$	$(5.58726 \pm 6.5668 \times 10^{-2}) \times 10$
	RN = 1.0%
$\hat{\epsilon}_{s,0}$	$(8.01654 \pm 1.4577 \times 10^{-2}) \times 10$
$\hat{\kappa}_s$	$(5.64524 \pm 1.2738 \times 10^{-1}) \times 10$
	RN = 3.0%
$\hat{\epsilon}_{s,0}$	$(8.00636 \pm 4.2160 \times 10^{-2}) \times 10$
$\hat{\kappa}_s$	$(5.87948 \pm 3.6783 \times 10^{-1}) \times 10$
	RN = 5.0%
$\hat{\epsilon}_{s,0}$	$(7.99621 \pm 6.8206 \times 10^{-2}) \times 10$
$\hat{\kappa}_s$	$(6.11765 \pm 5.9447 \times 10^{-1}) \times 10$
	RN = 10.0%
$\hat{\epsilon}_{s,0}$	$(7.97084 \pm 1.2723 \times 10^{-1}) \times 10$
$\hat{\kappa}_s$	$(6.73217 \pm 1.1076) \times 10$
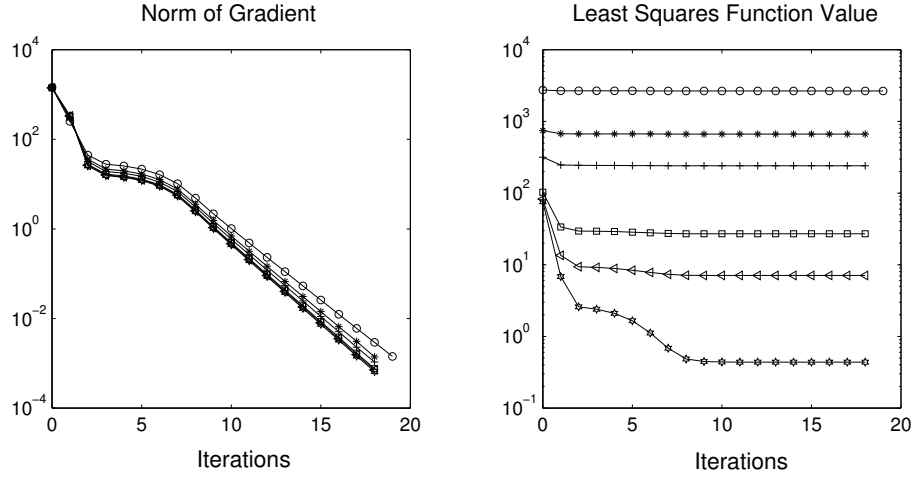
Figure 53: Estimation of $\epsilon_{s,0}$ and κ_s by the Levenberg-Marquardt algorithm for varying levels of constant variance noise. Details of the LM simulation.
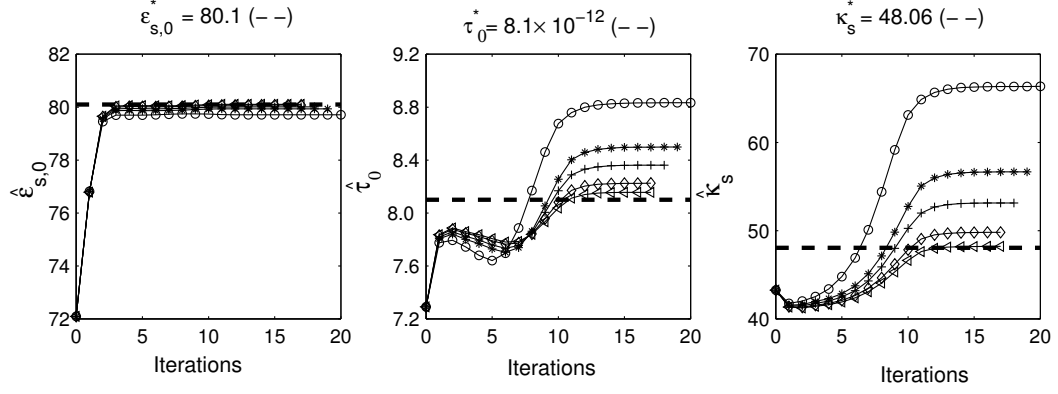
Figure 54: Estimation of $\epsilon_{s,0}$, τ_0 and κ_s by the Levenberg-Marquardt algorithm with varying levels of added constant variance noise. We plot the variation of the three parameters with the iteration count.
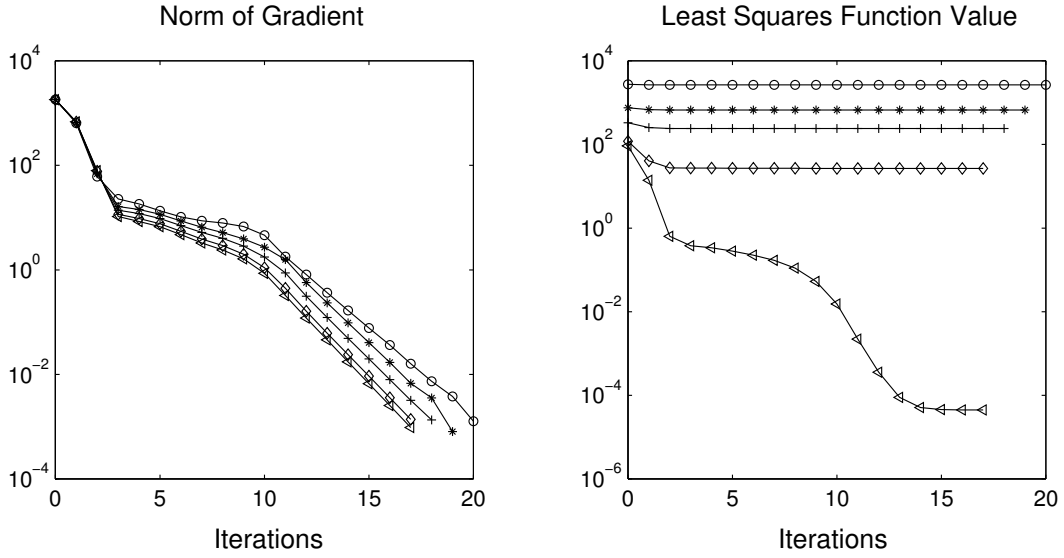

Figure 55: Levenberg-Marquardt for the three parameter estimation problem with varying levels of added constant variance noise. Details of the LM simulation.

Table 17: Parameter estimation of $\epsilon_{s,0}$ and τ_0 and κ_s for constant variance noise, corresponding to varying levels of relative noise with the Levenberg-Marquardt algorithm.

% RN	Iter	$\hat{\epsilon}_{s,0}$	$\hat{\tau}_0(\times 10^{-12})$	$\hat{\kappa}_s$	J^S	$||\nabla J^S||_{L^2}$
0.0	17	80.1083	8.1562	48.2113	4.4383×10^{-5}	0.0009637
1.0	17	80.0765	8.2247	49.8060	26.7071	0.001371
3.0	18	80.0079	8.3618	53.1392	240.3553	0.001345
5.0	19	79.9320	8.4983	56.6654	667.6441	0.0008044
10.0	20	79.7085	8.8330	66.3476	2670.5056	0.001268

Table 18: Parameter estimation of $\epsilon_{s,0}$ and τ_0 and κ_s for constant variance noise, corresponding to varying levels of relative noise with the Levenberg-Marquardt algorithm.

% RN	Iter	J^S	$||\nabla J^S||_{L^2}$	F	G	H
0.0	17	4.4383×10^{-5}	0.0009637	35	18	34
1.0	17	26.7071	0.001371	35	18	34
3.0	19	240.3553	0.001345	37	19	36
5.0	19	667.6441	0.0008044	39	20	38
10.0	20	2670.5056	0.001268	41	21	40

Table 19: Confidence Intervals for the parameter estimation of $\epsilon_{s,0}$, τ_0 and κ_s for constant variance noise with the Levenberg-Marquardt algorithm.

RN	0.0%
$\hat{\epsilon}_{s,0}$	$(8.01083 \pm 1.8741 \times 10^{-5}) \times 10$
$\hat{\tau}_0$	$(8.1562 \pm 2.3234 \times 10^{-4}) \times 10^{-12}$
$\hat{\kappa}_s$	$(4.82113 \pm 2.6830 \times 10^{-4}) \times 10$
RN	1.0%
$\hat{\epsilon}_{s,0}$	$(8.00765 \pm 1.4334 \times 10^{-2}) \times 10$
$\hat{\tau}_0$	$(8.2247 \pm 1.7742 \times 10^{-1}) \times 10^{-12}$
$\hat{\kappa}_s$	$(4.98060 \pm 2.0560 \times 10^{-1}) \times 10$
RN	3.0%
$\hat{\epsilon}_{s,0}$	$(8.00079 \pm 4.1822 \times 10^{-2}) \times 10$
$\hat{\tau}_0$	$(8.3618 \pm 5.1552 \times 10^{-1}) \times 10^{-12}$
$\hat{\kappa}_s$	$(5.31392 \pm 6.0178 \times 10^{-1}) \times 10$
RN	5.0%
$\hat{\epsilon}_{s,0}$	$(7.99320 \pm 6.7841 \times 10^{-2}) \times 10$
$\hat{\tau}_0$	$(8.4983 \pm 8.3159 \times 10^{-1}) \times 10^{-12}$
$\hat{\kappa}_s$	$(5.66654 \pm 9.7843 \times 10^{-1}) \times 10$
RN	10.0%
$\hat{\epsilon}_{s,0}$	$(7.97085 \pm 1.2736 \times 10^{-1}) \times 10$
$\hat{\tau}_0$	$(8.8330 \pm 1.5277) \times 10^{-12}$
$\hat{\kappa}_s$	$(6.63476 \pm 1.8360) \times 10$

estimation problem.

7   A second test case

In this section we consider the parameter estimation for a Debye medium with a larger relaxation time than the value that was considered in the first test problem. We would like to study the effect of the relaxation time τ and the interrogation frequency ω_c on the ability of the electromagnetic pulse to penetrate the dielectric material. As shown in [BBL00] a very small relaxation time, such as that for water $\tau_0^* = 8.1 \times 10^{-12}$, will make the material appear comparatively "hard" in the sense that it will allow much less of the signal to penetrate the air-Debye interface at $z = z_1$ for a sufficiently high interrogation frequency like $\omega_c = \pi \times 10^{10}$ rad/sec. This small transmitted wave can only generate very little, if any, reflection at the second interface as it enters the region containing the pressure wave. This demonstrates the importance of the choice of the carrier frequency ω_c for effective interrogation. In [BBL00] the authors have

demonstrated the strong influence of the dielectric relaxation time on an appropriate choice of the interrogating frequency for successfully penetrating the material. In this second test case we consider a parameter estimation problem for a Debye medium with a relaxation time $\tau_0^* = 3.16 \times 10^{-8}$ (as used in [BBL00, ABR02]), and an interrogation frequency $\omega_c = \pi \times 10^{10}$ rad/sec.

As observed in Section (4.1), the product $\omega_c \tau_0$ strongly determines the parameters in the problem that can be identified accurately. We will observe that by changing the values of τ_0 and ω_c in this second test problem, the parameters that dominate in the term ϵ_r^* in (74) are no longer the same as those of the first test problem, i.e., $\epsilon_{s,0}^*$ and κ_s^*. As will be demonstrated in Section (7.2), the parameters whose magnitude dominates the quantity ϵ_r^* are $\epsilon_{\infty,0}^*$ and the pressure coefficient κ_∞^*.

The data that we will attempt to fit is generated with a Debye model which is defined by the parameter values

$$
\begin{aligned}
\epsilon_{s,0}^* &= 78.2 \\
\epsilon_{\infty,0}^* &= 5.5 \\
\tau_0^* &= 3.16 \times 10^{-8} \\
\sigma^* &= 1 \times 10^{-5}
\end{aligned}
\qquad
\begin{aligned}
\kappa_\tau^* &= 0.05\tau_0^* = 1.58 \times 10^{-9} \\
\kappa_s^* &= 0.6\epsilon_{s,0}^* = 46.92 \\
\kappa_\infty^* &= 0.3\epsilon_{\infty,0}^* = 1.65.
\end{aligned}
\tag{112}
$$

In this model, the value of τ_0^* is much higher than in the case of the first test problem. As will be seen in the sequel, this value of τ_0^* leads to a parameter estimation problem with very different properties.

7.1   The forward problem: Simulation results

We perform similar numerical simulations, as were done for the first test problem, to collect simulated data at the center of the antenna and to demonstrate the effect of the acoustic pressure on the electric field. We would like to know how and to what extent the acoustic pressure can change the reflected electric wave from the interface at $z = z_2$. In Figure 56 we plot the electromagnetic source that is used in our simulations. The form for the source is

$$
\mathbf{J}_s(t, x, z) = I_{(x_1, x_2)}\delta(z)\sin(\omega_c(t - 3t_0))\exp\left(-\left[\frac{t - 3t_0}{t_0}\right]^2\right)\hat{\mathbf{x}},
$$
$$
t_0 = \frac{1}{\pi \times 10^9}; \ \omega_c = \pi \times 10^{10} \ \text{rad/sec}; \ f_c = 5.0 \times 10^9 \ \text{Hz}.
\tag{113}
$$

where $I_{(x_1, x_2)}$ is the Indicator function on (x_1, x_2). The Fourier spectrum of this pulse has even symmetry about 5.0 GHz. In Figure 57 we plot the power spectral density of the source defined in (113). We see that the power spectral density is symmetric about 5.0 GHz.

The computational domain is defined as follows. We take $X_0 = (0, 0.12)$, $Z_a = (0, 0.33)$ and $Z_D = (0.33, 0.5)$. The number of nodes along the z-axis is taken to be 450

and the number of nodes along the x-axis is taken to be 108. The spatial step size in both the x and z directions is $\Delta x = \Delta z = h = 0.06/54$. From the CFL condition (55) with the Courant number $\eta_{\mathrm{CN}} = 1/2$ we obtain the time increment to be $\Delta t \approx 1.852$ pico seconds. The central frequency of the input source as described in (54) is 5.0 GHz and thus the wavelength is 0.06 meters. The antenna is half a wavelength long and is placed at $(x_1, x_2) \times z_c$, with $z_c = 0$, $x_1 = 0.03$ and $x_2 = 0.09$. We use PML layers that are half a wavelength thick on all fours sides of the computational domain as shown in Figure 3. The reflections of the electromagnetic pulse at the air-Debye interface and from the acoustic pressure wave are recorded at the center of the antenna (x_c, z_c), with $x_c = 0.06$, at every time step. This data will be used as observations for the parameter identification problem to be presented later. The component of the electric field that is of interest here is the E_x component. Thus our data is the set

$$\mathbf{E}(\mathbf{q}^*) = \{E_x(t = n\Delta t, x_c, z_c; \mathbf{q}^*)\}_{n=1}^M$$
$$\mathbf{q}^* = (\epsilon_{s,0}^*, \epsilon_{\infty,0}^*, \tau_0^*, \sigma^*, \kappa_s^*, \kappa_\infty^*, \kappa_\tau^*)^T. \tag{114}$$

The windowed acoustic pressure wave as defined in (49) has the parameter values $\omega_p = 4.0\pi \times 10^4$ rad/sec, $c_p = 667.67$ m/s, and thus, $\lambda_p = 0.033$. The location of the pressure region is in the interval $(z_2, z_2 + \lambda_p) = (0.44, 0.47)$.

In Figures 58 -61 we plot the E_x field magnitude in the plane containing the center of the antenna versus depth along the z axis. Figure 58 depicts the electromagnetic wave penetrating the Debye medium. In 59 we see the reflection of the electromagnetic wave from the Debye medium moving towards the antenna and the Brillouin precursor propagating in the Debye medium. In Figure 60 we observe the reflection from the region containing the acoustic pressure moving towards the air-Debye interface and the transmitted part of the electromagnetic source travelling into the absorbing layer. The reflection from the acoustic pressure crosses the air-Debye interface in Figure 61. Here we see another reflected wave from the air-Debye interface that moves towards the right. In Figures 62 and 63 we plot the E_x field magnitude recorded at the center of the antenna versus time, which shows the electromagnetic source, the reflection off the air-Debye interface and the reflection from the region containing the acoustic pressure wave. As seen here the magnitude of the reflection from the acoustic pressure is many orders of magnitude smaller that the initial electromagnetic source as well the reflection from the air-Debye interface.

7.2   Sensitivity analysis

Here we examine the system dynamics as the parameters vary. We are interested in the changes produced by the coefficents of pressure in the polarization, namely the parameters κ_s, κ_∞ and κ_τ. In Figure 65 we plot the difference in the E_x component of the electric field between the simulation with parameter values given in (112) and simulations for which the value of κ_∞ is 0, $0.4\epsilon_{\infty,0}$ and $0.5\epsilon_{\infty,0}$. As expected the difference is seen in the acoustic reflection that is observed at the center of the
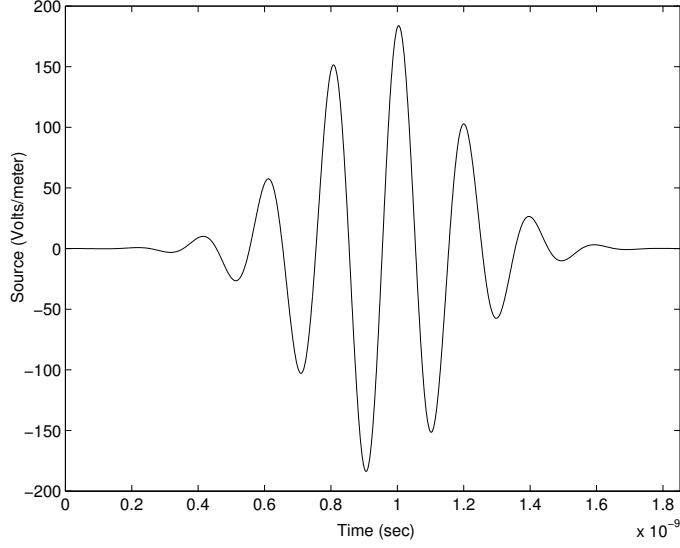
Figure 56: Forward Simulation for a Debye medium with parameters given in (112). The input electromagnetic source as defined in (113).

antenna. In Figure 66 we plot the difference in the E_x component of the electric field between the simulation with parameter values given in (112) and simulations for which the value of κ_s is 0, and $0.3\epsilon_{s,0}$. In Figure 67 we plot the difference in the E_x component of the electric field between the simulation with parameter values given in (112) and simulations for which the value of κ_τ is 0 and $0.1\epsilon_{s,0}$. Again, in both cases the difference is seen in the acoustic reflection that is observed at the center of the antenna. We observe that the difference in the E_x field in the case of Figures 66 and 67 is one or two orders of magnitude smaller than that in Figure 65. This indicates that the coefficent that is most significant for this test problem and which will be estimated more accurately than the others is κ_∞, the pressure coefficient in ϵ_∞. In the first test problem κ_s, the pressure coefficient in ϵ_s was the most significant. So we see a very different behaviour of the acoustic reflection in this case.

This observation, as was done for the first test problem, can also be deduced from an analysis of (40). In the simulations for this test problem the outgoing and reflected radiation will be dominated by frequencies near the center frequency 5.0 GHz. Thus, ϵ_r^* will be dominated by frequencies near 5.0 GHz. In this problem $\omega\tau_0^* \approx \mathcal{O}(10^2)$,

84
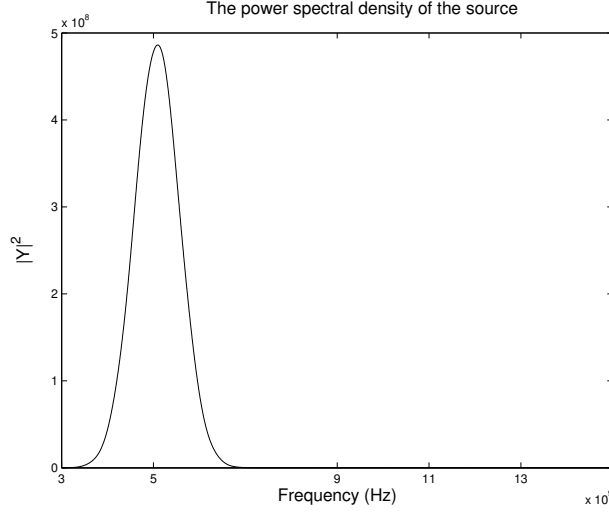
Figure 57: Fourier transform of the source defined in (113). The transform is centered around the central frequency of $\omega = \pi \times 10^{10}$ rad/sec.

and with $\epsilon_0 = 8 \times 10^{-12}$ we have (compare with the estimates of (75))

$$\begin{aligned}
\left(\frac{\epsilon_{s,0}^*}{1 + j\omega\tau_0^*} \right) & \approx \mathcal{O}(10^{-2}\epsilon_{s,0}^*) & \approx \mathcal{O}(10^{-1}), \\
\left(\frac{j\omega\tau_0^*}{1 + j\omega\tau_0^*} \right) \epsilon_{\infty,0}^* & \approx \mathcal{O}(\epsilon_{\infty,0}^*) & \approx \mathcal{O}(10), \\
\left(\frac{\sigma^*}{j\omega\epsilon_0} \right) & \approx \mathcal{O}(10^3\sigma^*) & \approx \mathcal{O}(10^{-3}).
\end{aligned} \tag{115}$$

Thus we can see that ϵ_r^* will be most sensitive to the infinite frequency permittivity $\epsilon_{\infty,0}$ and the effects of $\epsilon_{s,0}$ and τ_0 and σ will not be as pronounced. Also, this implies that ϵ_r^* will be more sensitive to the pressure coefficient κ_∞ than to the coefficients κ_s and κ_τ, which is the same observation that was made from Figures 65, 66 and 67

We next study the effect that the acoustic speed and frequency have on the amplitude of the reflection from the acoustic pressure region as was done in the first test problem. In Figure 68 we plot the acoustic reflection observed at the center of the antenna for different values of the acoustic frequency and in Figure 69 we plot the acoustic reflection for different values of the acoustic speed. As noted before, by changing the speed or the frequency, the wavelength λ_p changes and thus the size of the interval $(z_2, z_2 + \lambda_p)$ in which the pressure wave is generated. The amplitude of the acoustic reflection appears to increase as the acoustic frequency is increased and decreases as the acoustic speed increases, the opposite behaviour to what was
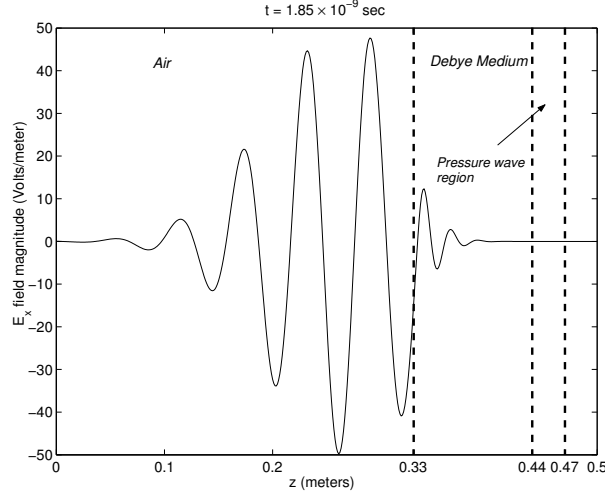
Figure 58: Forward Simulation for a Debye medium with parameters given in (112). The E_x field magnitude along the plane containing the center of the antenna versus depth. We see here the electromagnetic source penetrating the Debye medium.
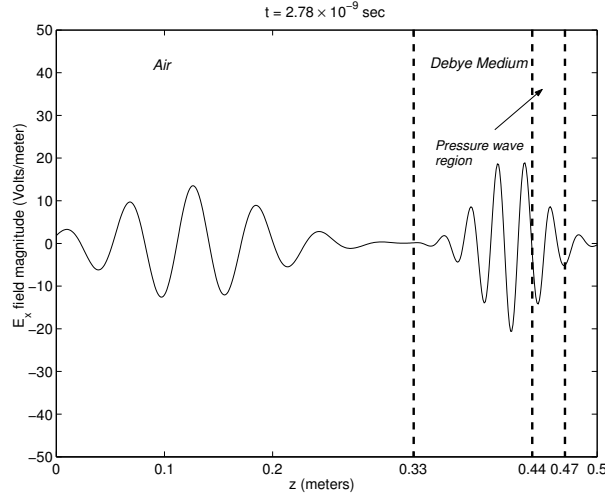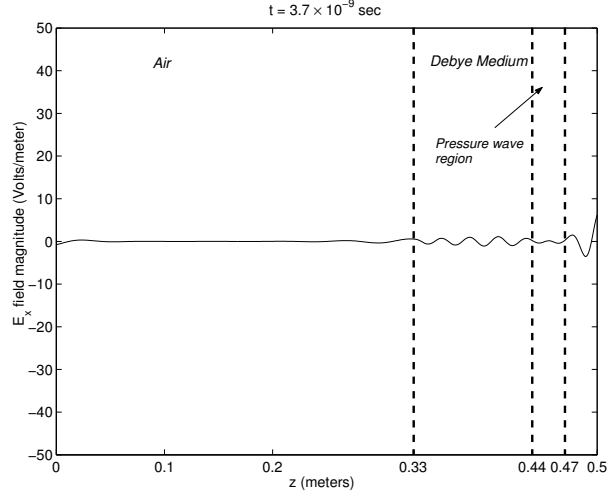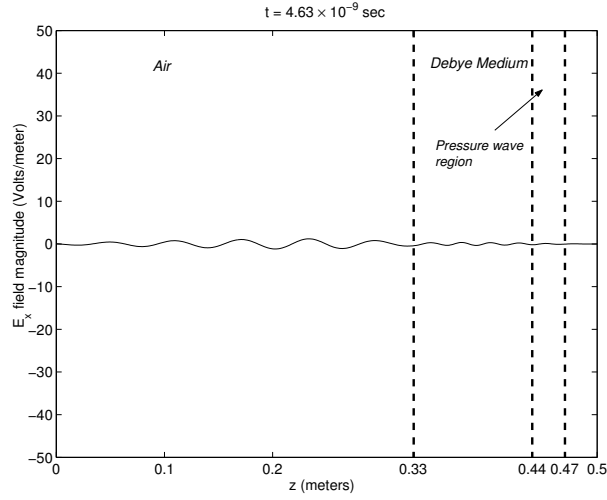

Figure 59: Forward Simulation for a Debye medium with parameters given in (112). The E_x field magnitude along the plane containing the center of the antenna versus depth. The plot shows the reflection of the electromagnetic source off the air-Debye interface travelling towards the antenna. We also see the brillouin precursor propagating inside the Debye medium.

Figure 60: Forward Simulation for a Debye medium with parameters given in (112). The E_x field magnitude along the plane containing the center of the antenna versus depth. Here we see the reflection from the acoustic pressure wave moving towards the left.
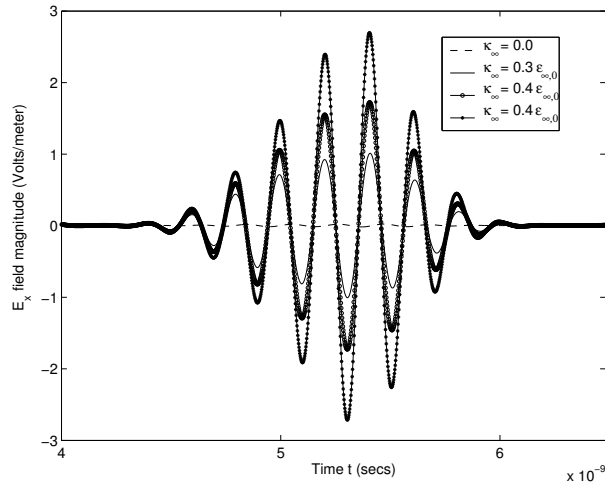

Figure 61: Forward Simulation for a Debye medium with parameters given in (112). The E_x field magnitude along the plane containing the center of the antenna. The reflection from the acoustic pressure wave crosses the air-Debye interface. A secondary reflection off this interface travels towards the right.
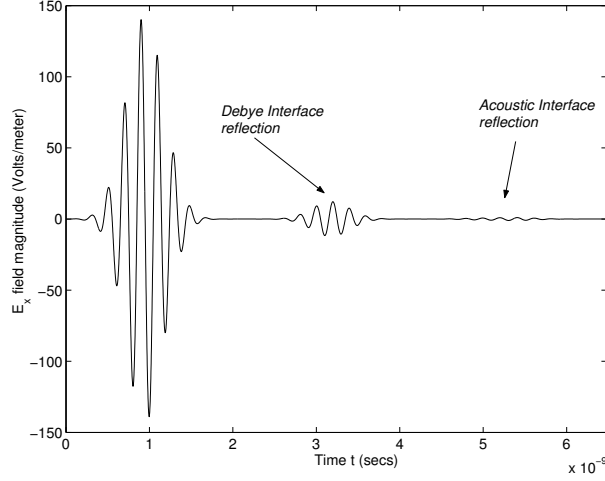
Figure 62: Forward Simulation for a Debye medium with parameters given in (112). The E_x field magnitude versus time. We see three sets of observations. The electromagnetic source, the reflection off the air-Debye interface and the relection from the acoustic pressure wave.
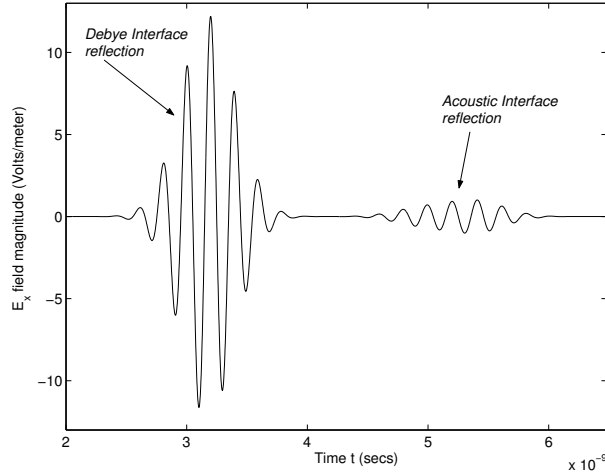
Figure 63: Forward Simulation for a Debye medium with parameters given in (112). The E_x field magnitude versus time. Here we magnify the two sets of reflections, one from the air-Debye interface and from the acoustic pressure wave.
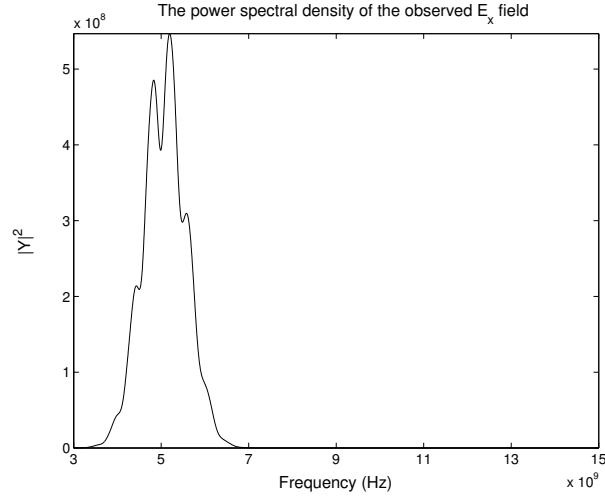
Figure 64: Fourier transform of the electric field data in Figure 62. The transform is centered around the central frequency of $\omega = 10\pi \times 10^9$.

Figure 65: Forward Simulation for a Debye medium with parameters given in (112). The E_x field magnitude measured at the center of the antenna for different values of κ_∞.
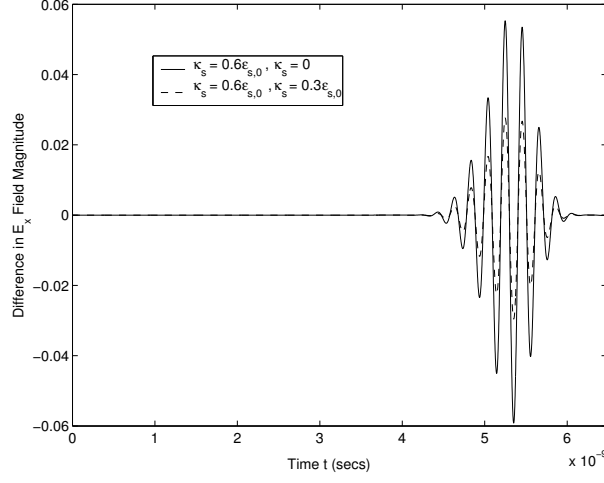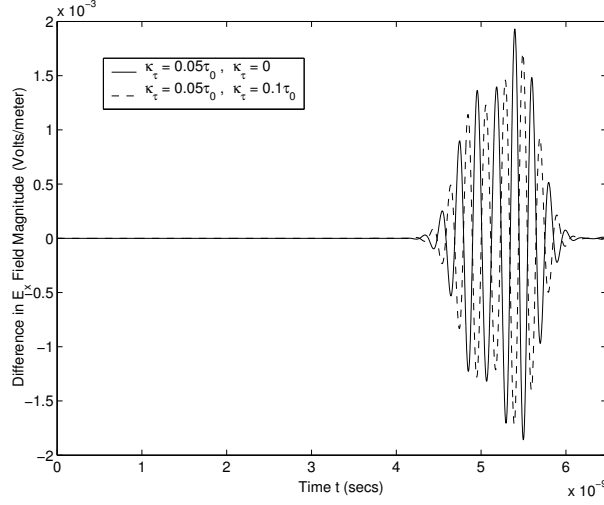
Figure 66: Difference in the E_x field magnitude measured at the center of the antenna between the simulation for parameters given in (112) and simulations with different values of κ_s.

observed in the first test problem. We note here again that as our windowed pressure wave contains only one wavelength of the sinusoid it is difficult to predict how the reflections will behave as the speed or the frequency is changed.

7.3 Simulation results for the inverse problem: The Levenberg Marquardt method

In this section we present results for the inverse problem of parameter estimation for the second test problem. We do this first with the Levenberg-Marquardt algorithm and later with the Nelder-Mead method. We first attempt to estimate the three parameters $\epsilon_{\infty,0}$, τ_0 and the pressure coefficient κ_∞, of ϵ_∞. The values of the remaining parameters are fixed at

$$
\begin{aligned}
\epsilon_{s,0}^* &= 71.09 \ \text{(relative static permittivity)}, \\
\epsilon_{\infty,0}^* &= 5.5 \ \text{(relative high frequency permittivity)}, \\
\tau_0^* &= 3.48 \times 10^{-8} \ \text{seconds}, \\
\sigma^* &= 1.5 \times 10^{-5} \ \text{(mhos/meter)},
\end{aligned}
\tag{116}
$$

90

Figure 67: Difference in the E_x field magnitude measured at the center of the antenna between the simulation for parameters given in (112) and simulations with different values of κ_τ.

$$
\begin{aligned}
\kappa_s^* &= 42.654 \quad \text{(pressure coefficient in } \epsilon_s^*), \\
\kappa_\infty^* &= 1.65 \quad \text{(pressure coefficient in } \epsilon_\infty^*), \\
\kappa_\tau^* &= 1.74 \times 10^{-9} \quad \text{(pressure coefficient in } \tau^*).
\end{aligned}
\tag{117}
$$

The results are tabulated in Tables 20 and 21 and presented in Figures 70-73. We have added constant variance noise with different values of the scale parameter ν to the data. We note from Table 20 that the estimation of $\epsilon_{\infty,0}$ is relatively stable over all values of ν that we have selected; whereas the estimation of κ_∞ becomes inaccurate as the value of ν is increased. Unlike the previous test problem, the estimation of τ_0 in this case is not good. Table 21 presents the number of function, gradient and hessian evaluations that are required for the algorithm to converge, where the convergence criteria used here is $||\nabla \mathrm{J}_k^S||/||\nabla \mathrm{J}_0^S|| < 10^{-6}$.

In Table 22 we present the confidence intervals for the three parameter estimation problem with results tabulated in Table 20. Again, we note that the confidence intervals become larger as the level of noise increases. From Table 22 we observe that the confidence level in the estimates $\hat{\epsilon}_\infty$ and $\hat{\kappa}_\infty$ is higher than the confidence level in $\hat{\tau}_0$, as is also observed from the final estimates for τ_0.

We now attempt to estimate the two parameters $\epsilon_{\infty,0}$ and its pressure coefficient κ_∞. We fix the value of the relaxation time τ_0 to be

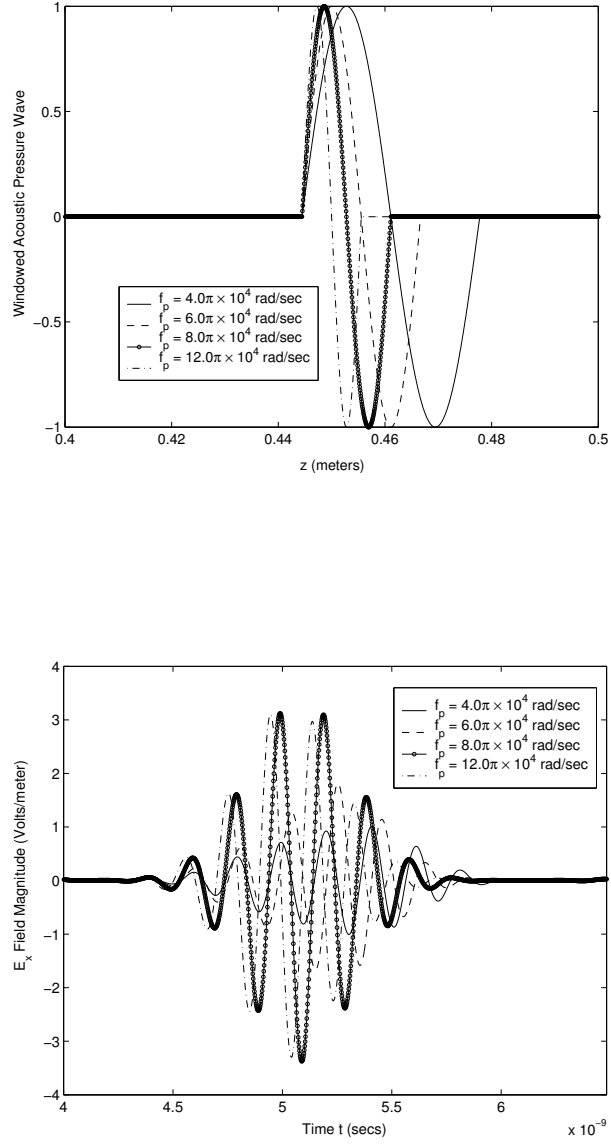$$
\tau_0 = 3.48 \times 10^{-8}.
\tag{118}
$$

91

Figure 68: Plot of the magnitude of the acoustic reflection against time for different values of the acoustic frequency. The other parameters are fixed at their true values given in (112).
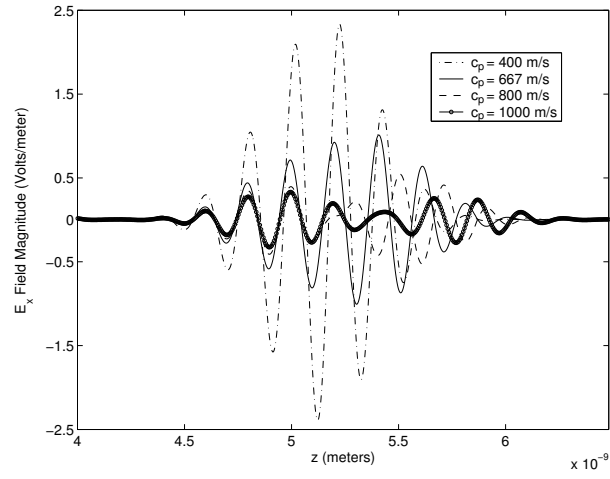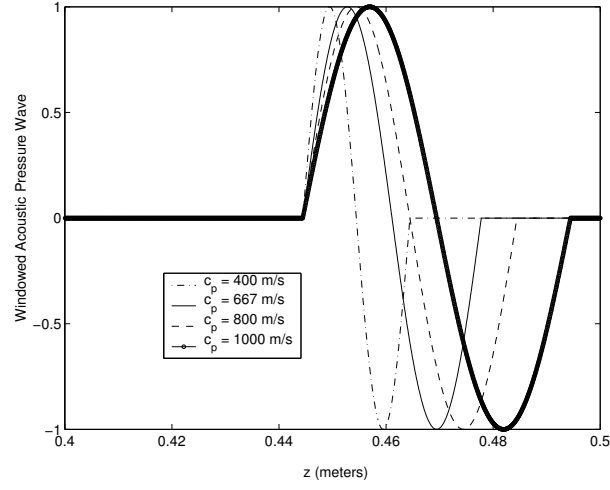
Figure 69: Plot of the magnitude of the E_x component of the electric field against time for different values of the acoustic speed. The other parameters are fixed at their true values given in (112).

Table 20: Parameter estimation of $\epsilon_{\infty,0}$, τ_0 and κ_∞ for constant variance noise, corresponding to varying levels of relative noise with the Levenberg-Marquardt algorithm.

% RN	Iter	$\hat{\epsilon}_{\infty,0}$	$\hat{\tau}_0$	$\hat{\kappa}_\infty$	J^S	$||\nabla J^S||_{L^2}$
0.0	32	5.4999	2.8522×10^{-8}	1.6496	2.1605×10^{-6}	0.0002746
0.1	32	5.4998	2.8761×10^{-8}	1.6463	0.2749	0.0002723
0.3	32	5.4996	2.9253×10^{-8}	1.6395	2.4743	0.0003417
0.5	32	5.4993	2.9764×10^{-8}	1.6328	6.8730	0.0004703
1.0	34	5.4985	3.1135×10^{-8}	1.6160	27.4921	0.0002261
3.0	39	5.4956	3.8493×10^{-8}	1.5467	247.4282	0.0002441
5.0	45	5.4926	5.1264×10^{-8}	1.4753	687.2987	0.0003073
10.0	57	5.4852	4.1950×10^{-7}	1.2957	2749.1770	0.00007404

Table 21: Parameter estimation of $\epsilon_{\infty,0}$, τ_0 and κ_∞ for constant variance noise, corresponding to varying levels of relative noise with the Levenberg-Marquardt algorithm.

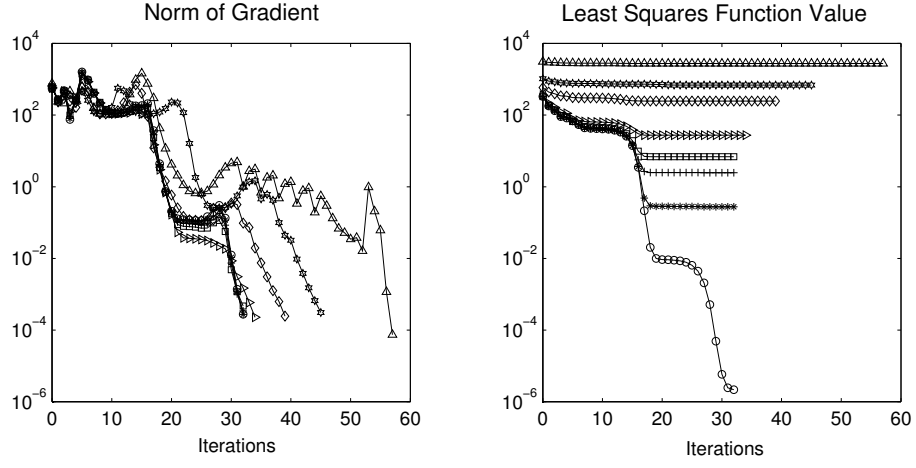| % RN	Iter	J^S	$||\nabla J^S||_{L^2}$	F	G	H
0.0	32	2.1605×10^{-6}	0.0002746	71	33	70
0.1	32	0.2749	0.0002723	71	33	70
0.3	32	2.4743	0.0003417	71	33	70
0.5	32	6.8730	0.0004703	71	33	70
1.0	34	27.4921	0.0002261	76	35	75
3.0	39	247.4282	0.0002441	86	40	85
5.0	32	687.2987	0.0003073	98	46	97
10.0	57	2749.1770	0.00007404	136	58	135

Figure 70: Parameter estimation of $\epsilon_{\infty,0}$, τ_0 and κ_∞ using the Levenberg-Marquardt algorithm with added constant variance noise for various values of ν.
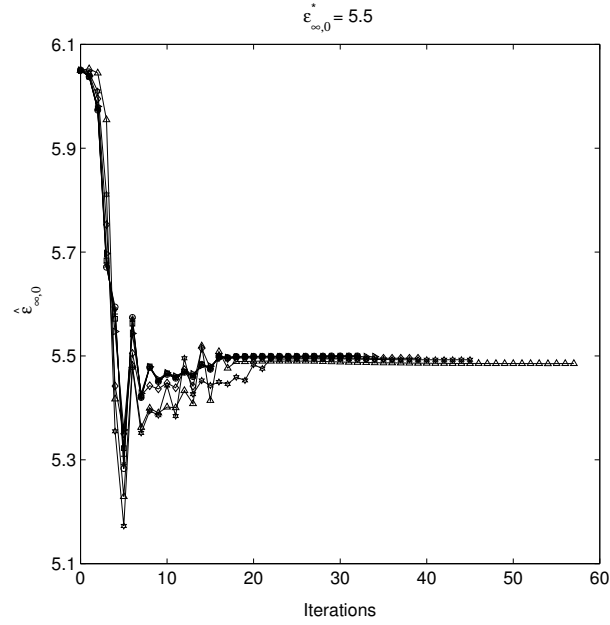

Figure 71: Levenberg-Marquardt for the three parameter estimation problem with added constant variance noise. Variation of the estimate $\hat{\epsilon}_{\infty,0}$ with the iteration count.
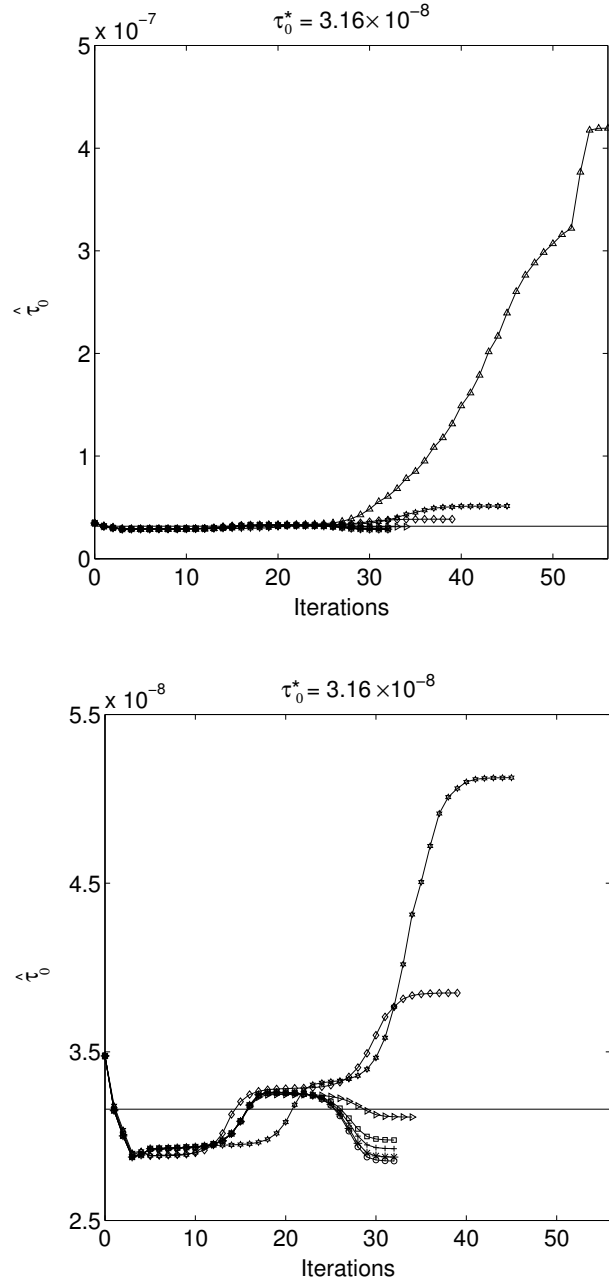
Figure 72: Levenberg-Marquardt for the three parameter estimation problem with added constant variance noise. We plot the variation of the estimate $\hat{\tau}_0$ with iteration count (top) and a magnified plot of the same (bottom).

Table 22: Confidence Intervals for the parameter estimation of $\epsilon_{\infty,0}$, τ_0 and κ_∞ with the Levenberg-Marquardt algorithm for varying levels of constant variance noise corresponding to 0%-10% relative noise.

|	RN = 0.0%
$\hat{\epsilon}_{\infty,0}$	$5.4999 \pm 9.8421 \times 10^{-7}$
$\hat{\tau}_0$	$(2.8522 \pm 1.9957 \times 10^{-4}) \times 10^{-8}$
$\hat{\kappa}_\infty$	$1.6496 \pm 2.8669 \times 10^{-5}$
	RN = 0.1%
$\hat{\epsilon}_{\infty,0}$	$5.4998 \pm 3.5104 \times 10^{-4}$
$\hat{\tau}_0$	$(2.8761 \pm 7.1807 \times 10^{-2}) \times 10^{-8}$
$\hat{\kappa}_\infty$	$1.6463 \pm 1.0238 \times 10^{-2}$
	RN = 0.3%
$\hat{\epsilon}_{\infty,0}$	$5.4996 \pm 1.0531 \times 10^{-3}$
$\hat{\tau}_0$	$(2.9253 \pm 2.1927 \times 10^{-1}) \times 10^{-8}$
$\hat{\kappa}_\infty$	$1.6395 \pm 3.0784 \times 10^{-2}$
	RN = 0.5%
$\hat{\epsilon}_{\infty,0}$	$5.4993 \pm 1.7548 \times 10^{-3}$
$\hat{\tau}_0$	$(2.9764 \pm 3.7209 \times 10^{-1}) \times 10^{-8}$
$\hat{\kappa}_\infty$	$1.6328 \pm 5.1417 \times 10^{-2}$
	RN = 1.0%
$\hat{\epsilon}_{\infty,0}$	$5.4985 \pm 3.5076 \times 10^{-3}$
$\hat{\tau}_0$	$(3.1135 \pm 7.7975 \times 10^{-1}) \times 10^{-8}$
$\hat{\kappa}_\infty$	$1.6160 \pm 1.0340 \times 10^{-1}$
	RN = 3.0%
$\hat{\epsilon}_{\infty,0}$	$5.4956 \pm 1.0504 \times 10^{-2}$
$\hat{\tau}_0$	$(3.8493 \pm 2.9130) \times 10^{-8}$
$\hat{\kappa}_\infty$	$1.5467 \pm 3.1752 \times 10^{-1}$
	RN = 5.0%
$\hat{\epsilon}_{\infty,0}$	$5.4926 \pm 1.7460 \times 10^{-2}$
$\hat{\tau}_0$	$(5.1264 \pm 6.5133) \times 10^{-8}$
$\hat{\kappa}_\infty$	$1.4753 \pm 5.4261 \times 10^{-1}$
	RN = 10.0%
$\hat{\epsilon}_{\infty,0}$	$5.4852 \pm 3.4394 \times 10^{-2}$
$\hat{\tau}_0$	$(4.1950 \pm 10.3835) \times 10^{-8}$
$\hat{\kappa}_\infty$	$1.2957 \pm 11.5944 \times 10^{-1}$
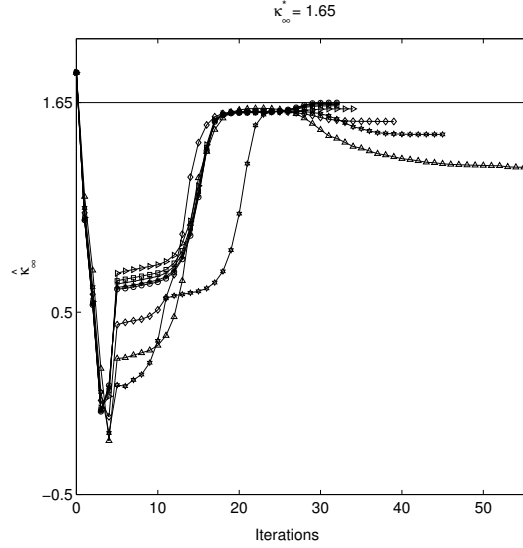
Figure 73: Levenberg-Marquardt for the three parameter estimation problem with added constant variance noise. We plot the variation of the estimate $\hat{\kappa}_\infty$ with the iteration count.

In Figures 74and 75 we plot the two parameter estimation inverse problem with no added noise to the simulated data. In Figures 76 and 77 we plot the two parameter estimation inverse problem with added constant variance noise to the simulated data. In Tables 23 and 24 we present the final estimates and details of the Levenberg-Marquardt simulations with varying levels of constant variance noise added to the data that is to be fit. In Table 25 we calculate the confidence intervals for the two parameter estimation problem of estimating $\epsilon_{\infty,0}$ and κ_∞ with added constant variance noise to the simulated data. In Figure 78 we plot the least squares objective function for different values of $\epsilon_{\infty,0}$ and κ_∞. There is no noise added to the data for these plots. The other five parameters are fixed at their true values as given in (112). We see possibilities of local minima in these plots. This test problem has many local minima whose evidence will be seen clearly in later plots. In Figure 79 we plot the least squares objective function for various values of the two parameters $\epsilon_{\infty,0}$ and κ_∞. Again we have not added any noise to the data for these plots. The other five parameters were fixed at values given in (116) and (117) except for τ_0 which was fixed at its true value as given in (112).
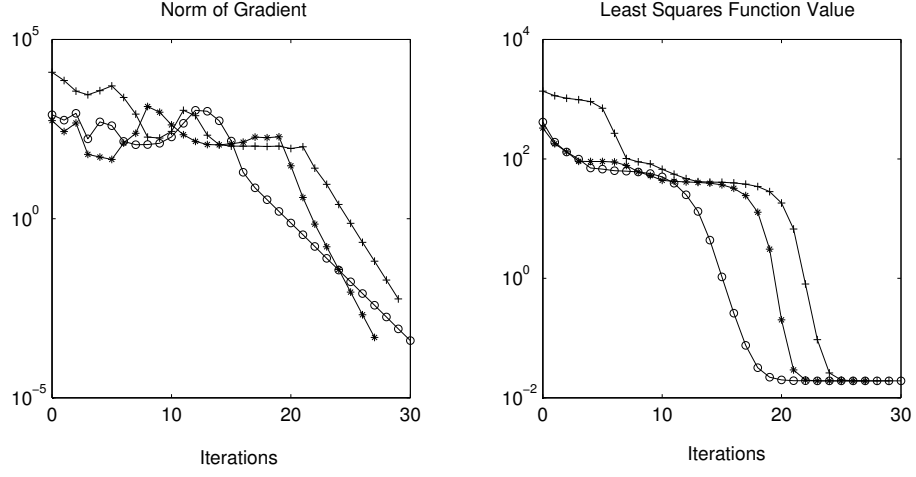
98

Figure 74: Parameter estimation of $\epsilon_{\infty,0}$ and κ_{∞} with no added noise using the Levenberg-Marquardt algorithm. The plot shows the details of the Levenberg-Marquardt algorithm.
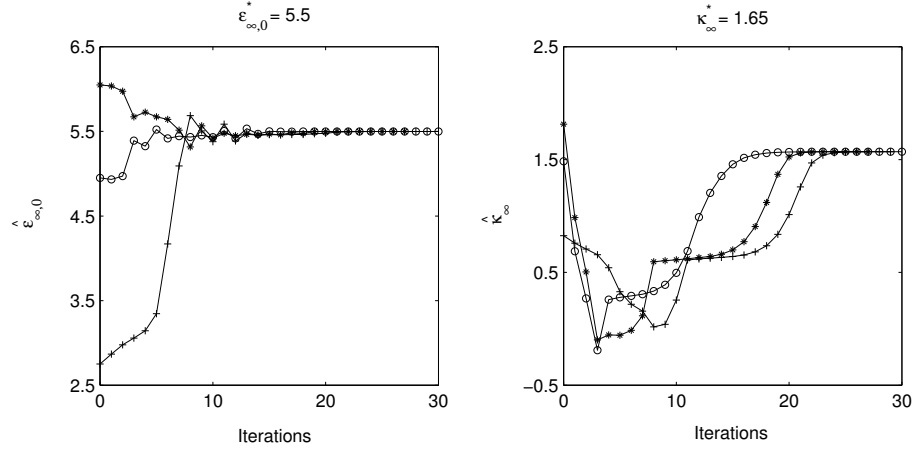

Figure 75: Levenberg-Marquardt for the two parameter estimation problem with no added noise. We plot the variation of $\hat{\epsilon}_{\infty,0}$ (left) and $\hat{\kappa}_{\infty}$ (right) versus the iteration count.
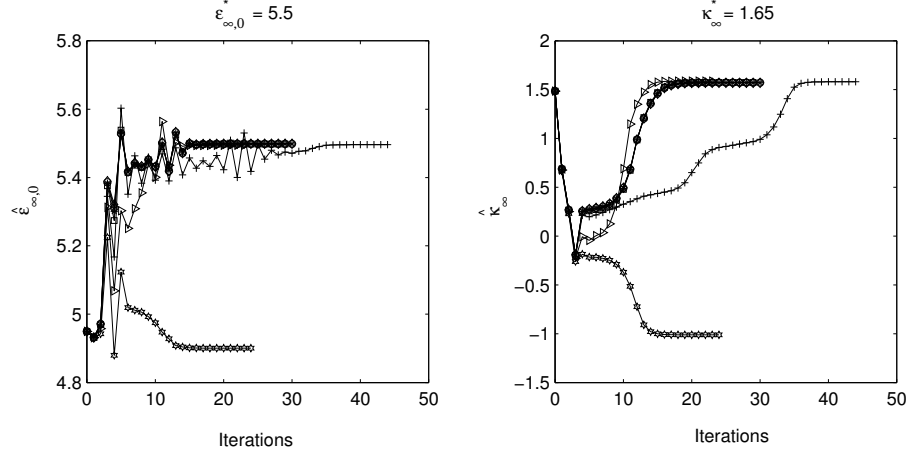
Figure 76: Parameter estimation of $\epsilon_{\infty,0}$ and κ_∞ with the Levenberg-Marquardt algorithm for varying levels of constant variance noise (ν), corresponding to 0%-10% relative noise. We plot the variation of $\hat{\epsilon}_{\infty,0}$ (left) and $\hat{\kappa}_\infty$ (right) versus the iteration count.
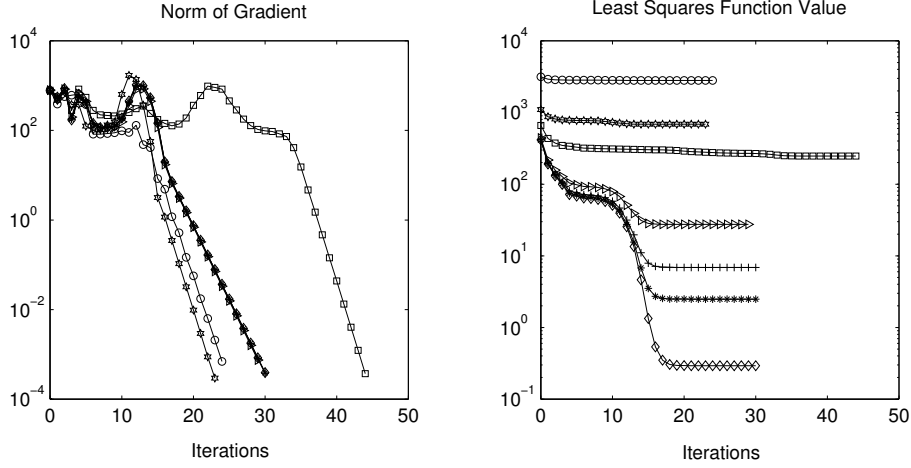

Figure 77: Details of the Levenberg-Marquardt simulations for the two parameter estimation problem with varying levels (ν) of constant variance noise added to the simulated data as tabulated in Table 23.

Table 23: Parameter estimation of $\epsilon_{\infty,0}$ and κ_∞ with the Levenberg-Marquardt algorithm for varying levels of constant variance noise, corresponding to 0%-10% relative noise.

% RN	Iter	$\hat{\epsilon}_{\infty,0}$	$\hat{\kappa}_\infty$	J^S	$||\nabla J^S||_{L^2}$
0.1	30	5.4988	1.5708	0.2924	0.0003925
0.3	30	5.4986	1.5714	2.4885	0.0003861
0.5	30	5.4984	1.5721	6.8843	0.0003768
1.0	29	5.4979	1.5738	27.4975	0.0007438
3.0	44	5.4961	1.5806	247.4317	0.0003701
5.0	23	5.4943	1.5873	687.3371	0.0002948
10.0	24	4.9006	-1.0116	2800.2627	0.0006955

Table 24: Parameter estimation of $\epsilon_{\infty,0}$ and κ_∞ with the Levenberg-Marquardt algorithm for varying levels of constant variance noise, corresponding to 0%-10% of relative noise.

% RN	Iter	J^S	$||\nabla J^S||_{L^2}$	F	G	H
0.1	30	0.2924	0.0003925	65	31	64
0.3	30	2.4885	0.0003861	65	31	64
0.5	30	6.8843	0.0003768	65	31	64
1.0	29	27.4975	0.0007438	63	30	62
3.0	44	247.4317	0.0003701	91	45	90
5.0	23	687.3371	0.0002948	49	24	48
10.0	24	2800.2627	0.0006955	52	25	51

Table 25: Confidence Intervals for the parameter estimation of $\epsilon_{\infty,0}$ and κ_{∞} with the Levenberg-Marquardt algorithm for varying levels (ν) of constant variance noise corresponding to 0%-10% relative noise.

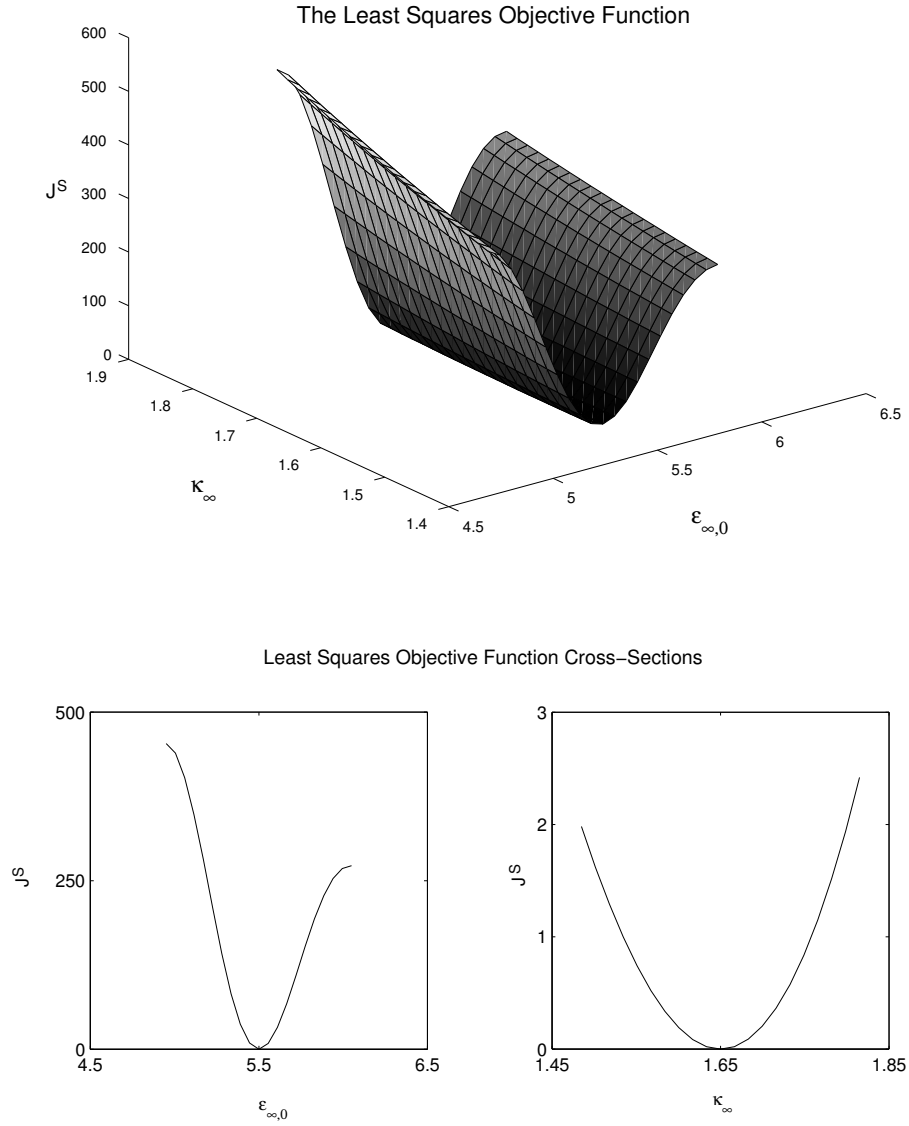|	RN = 0.1%
$\hat{\epsilon}_{\infty,0}$	$5.4988 \pm 3.3500 \times 10^{-4}$
$\hat{\kappa}_{\infty}$	$1.5708 \pm 2.0666 \times 10^{-3}$
	RN = 0.3%
$\hat{\epsilon}_{\infty,0}$	$5.4986 \pm 9.7663 \times 10^{-4}$
$\hat{\kappa}_{\infty}$	$1.5714 \pm 6.0237 \times 10^{-3}$
	RN = 0.5%
$\hat{\epsilon}_{\infty,0}$	$5.4984 \pm 1.6231 \times 10^{-3}$
$\hat{\kappa}_{\infty}$	$1.5721 \pm 1.0009 \times 10^{-2}$
	RN = 1.0%
$\hat{\epsilon}_{\infty,0}$	$5.4979 \pm 3.2375 \times 10^{-3}$
$\hat{\kappa}_{\infty}$	$1.5738 \pm 1.9955 \times 10^{-2}$
	RN = 3.0%
$\hat{\epsilon}_{\infty,0}$	$5.4961 \pm 9.6379 \times 10^{-3}$
$\hat{\kappa}_{\infty}$	$1.5806 \pm 5.9286 \times 10^{-2}$
	RN = 5.0%
$\hat{\epsilon}_{\infty,0}$	$5.4943 \pm 1.5943 \times 10^{-2}$
$\hat{\kappa}_{\infty}$	$1.587 \pm 9.7880 \times 10^{-2}$

Figure 78: (Top) The Least Squares Objective Function for different values of $\epsilon_{\infty,0}$ and κ_∞ with no noise added to the data. The other five parameters were fixed at their true values as given in (112). The minimum is located at the point $(5.5, 1.65)$, with a minimum value of 0. (Bottom) Cross Sections of the Least Squares Objective function versus κ_∞ (right) and versus $\epsilon_{\infty,0}$ (left).

In Figure 80 we plot the least squares objective function for a range of values of $\epsilon_{\infty,0}$ and κ_∞, again with no added noise. In this case we have not added any noise to the data. The other five parameters were fixed at values given in (116), and (117), and τ_0 fixed at the value given in (118) that have 10-50% relative error as compared with their true values in (112).

7.4 Simulation results for the inverse problem: The Nelder-Mead method

We first attempt to estimate the two parameters $\epsilon_{\infty,0}$ and its pressure coefficient κ_∞. We add constant variance noise to our simulated data. The other five parameters are fixed at their values given in (116), and (117) with τ_0 fixed at the value given in (118). Figures 81 and 82 plot the details of the Nelder-Mead simulations and the variation of the two parameters over all iterations. Table 26 displays the final estimates and the details of the Nelder-Mead algorithm for the two parameter estimation problem with added constant variance noise. We note that the Nelder-Mead algorithm does not converge to the optimal values of either of the two parameters. Instead it appears to converge to a possible local minimum. We demonstrate this fact by plotting the least squares objective function for the case of added constant variance noise corresponding to $\nu = 0.005$ (1% RN) in the Figure 83. This figure clearly demonstrates the presence of many local optima. The reason for the presence of local optima is the fact that we are changing $\epsilon_{\infty,0}$ inside the Debye media. This changes the speed of propagation of the electromagnetic pulse inside the Debye media as the maximum wavespeed in the dispersive dielectric is $c_0/\sqrt{\epsilon_{\infty,0}}$ [Pet94]. A similar phenomenon was observed in [BGW03] where the authors constructed a modified least squares objective function to avoid the occurence of local optima. Another option to solve this problem would be to resort to using a global optimization method to solve the inverse problem. We note that the Levenberg-Marquardt method did not seem to converge to a local minima. However, this may be a fortunate occurence in which case we can always find some initial guesses that would cause such local optimization algorithms to converge to a local minimum instead of the global minimum.

In Table 27 we calculate the confidence intervals for the two parameter estimation problem. We note that the intervals are larger as compared with the results of the Levenberg-Marquardt method. We also plot the least squares objective function for different values of $\epsilon_{\infty,0}$ and κ_∞ without adding noise to the data. Again we see the presence of local optima as seen in Figures 84. To see how the interrogating frequency relates to the presence of local minima we repeat the inverse problem by lowering the interrogating frequency to 3.0 GHz from 5.0 GHz. In Figure 85 We observe that in this case the distance between successive minima has increased. Thus by lowering the interrogating frequency we can push the local minima away from each other and thius reduce the number of local minima that would occur in an interval of interest. We next attempt to estimate the three parameters τ_0, $\epsilon_{\infty,0}$ and its pressure
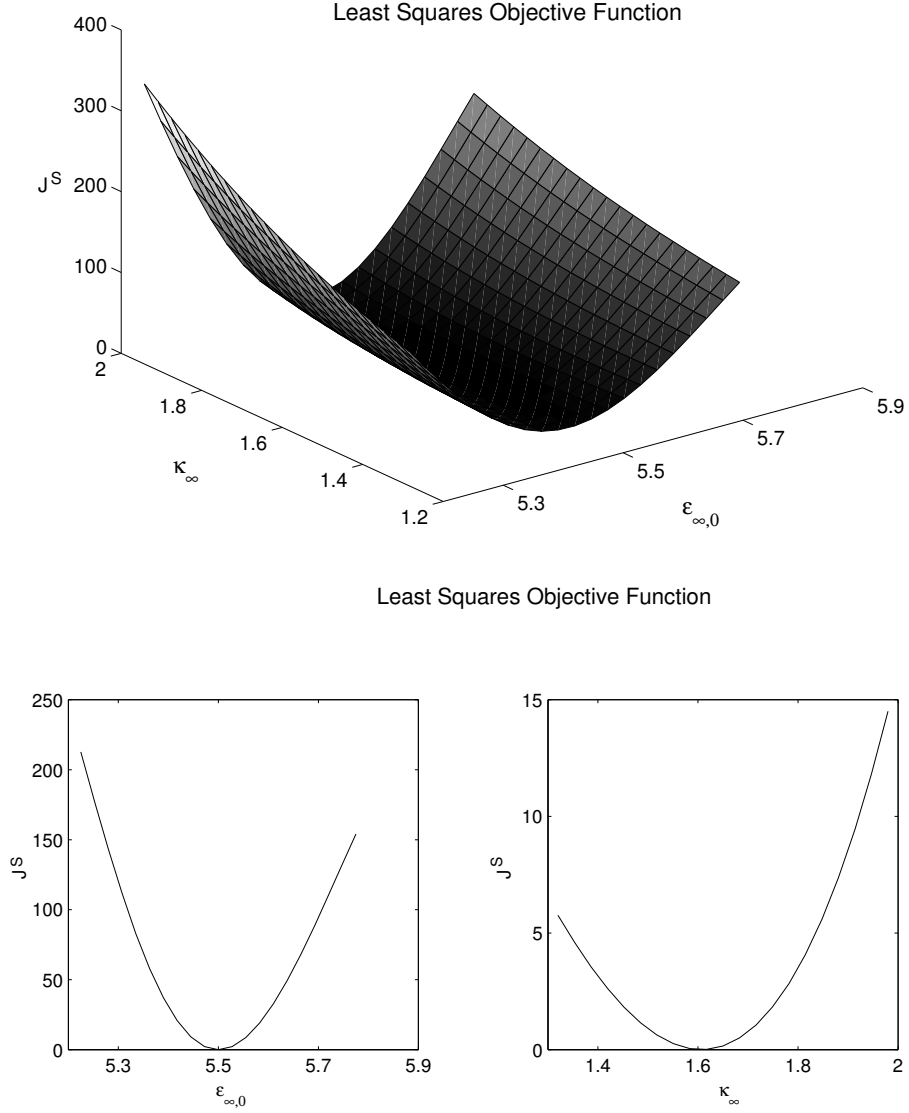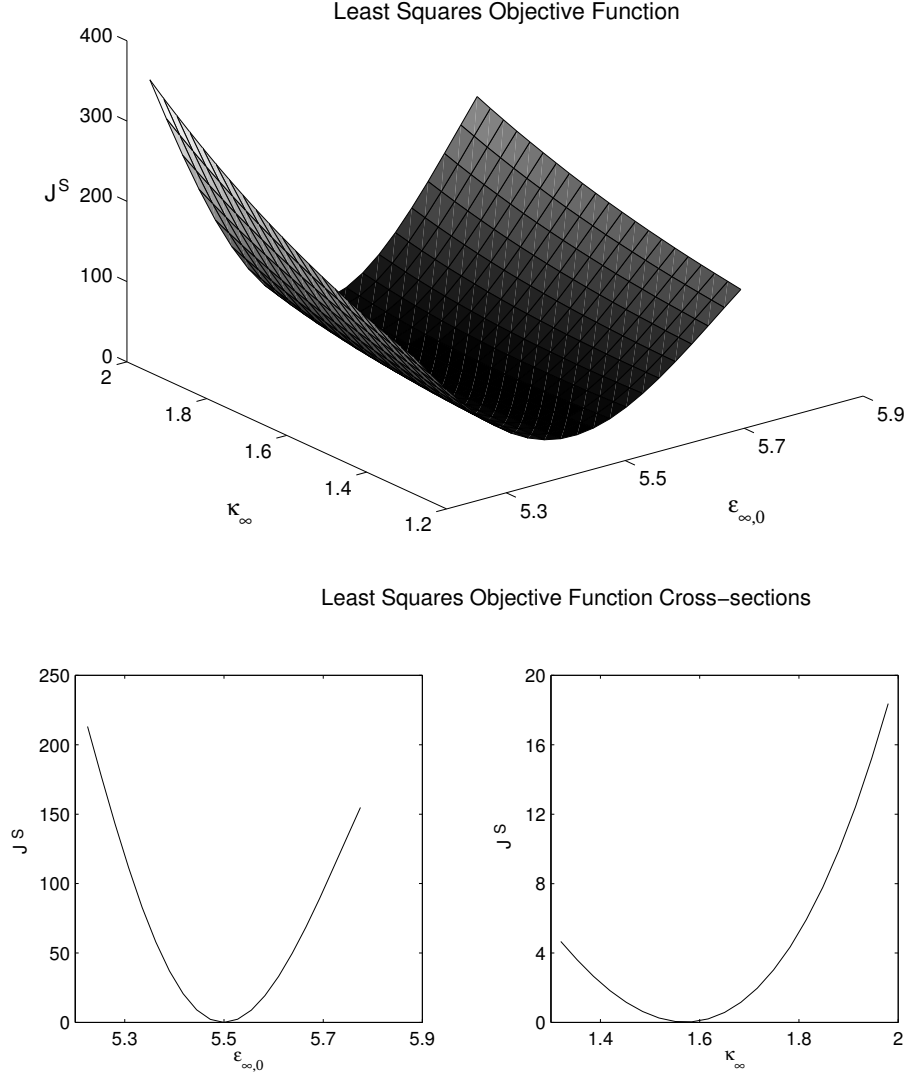
Figure 79: (Top) The Least Squares Objective Function for different values of $\epsilon_{\infty,0}$ and κ_∞ with no noise added to the data. The other five parameters were fixed at values given in (116), and (117) except for τ_0 which was fixed at its true value. The minimum is located at the point $(5.5, 1.617)$, with a minimum value of 0.0147. (Bottom) Cross Sections of the Least Squares Objective function versus κ_∞ (right) and versus $\epsilon_{\infty,0}$ (left).

Figure 80: (Top) The Least Squares Objective Function for different values of $\epsilon_{\infty,0}$ and κ_∞ with no noise added to the data. The other five parameters were fixed at values given in (116), and (117), and τ_0 fixed at the value given in (118) that have 10-50% relative error as compared with their true values. The minimum is located at the point $(5.5, 1.584)$, with a minimum value of 0.03595. (Bottom) Cross Sections of the Least Squares Objective function versus κ_∞ (right) and versus $\epsilon_{\infty,0}$ (left).
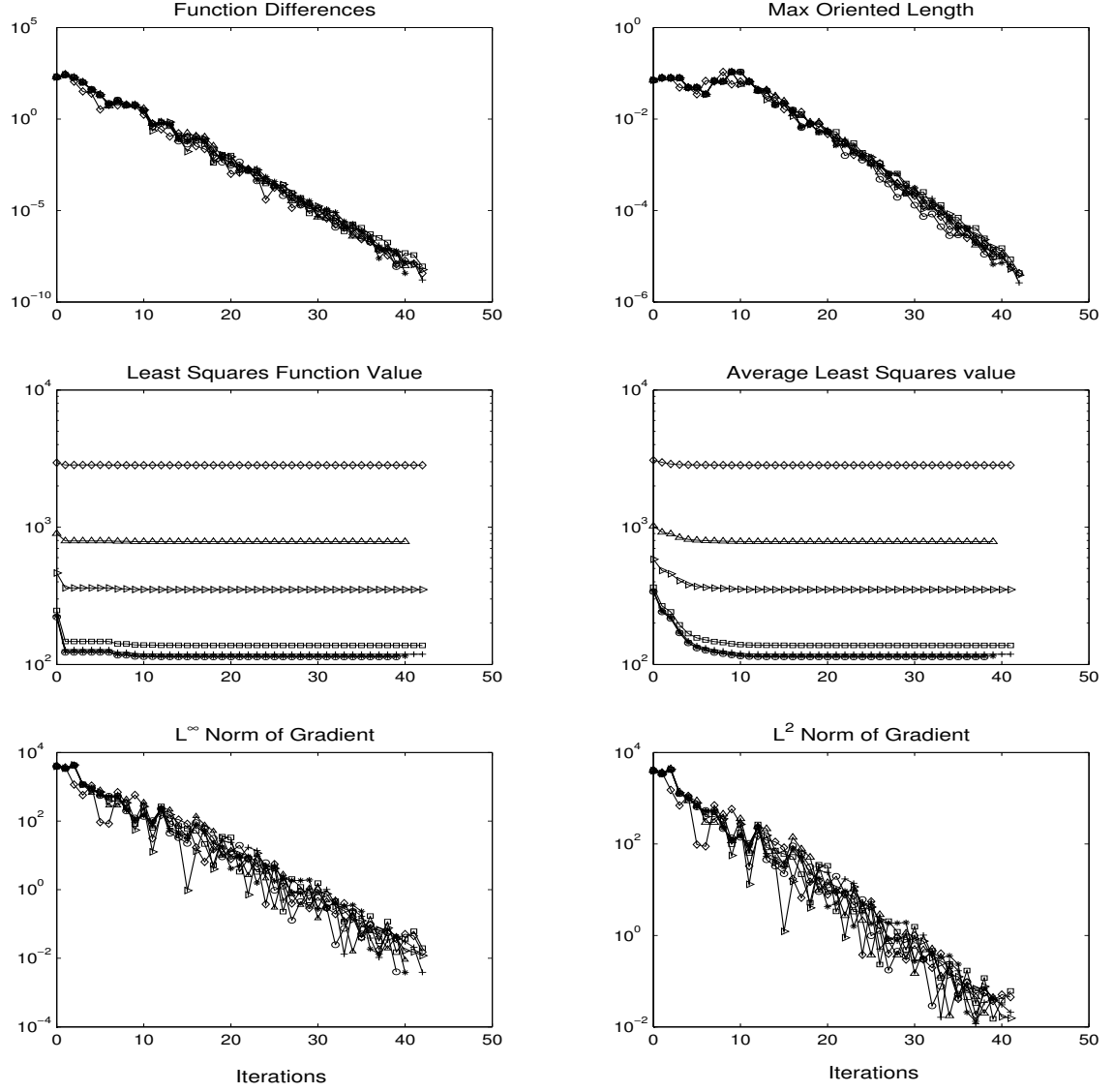
Figure 81: Details of the Nelder-Mead algorithms for the two parameter estimation of $\epsilon_{\infty,0}$ and κ_{∞} for varying levels (ν) of constant variance noise added to the data as tabulated in Table 26.
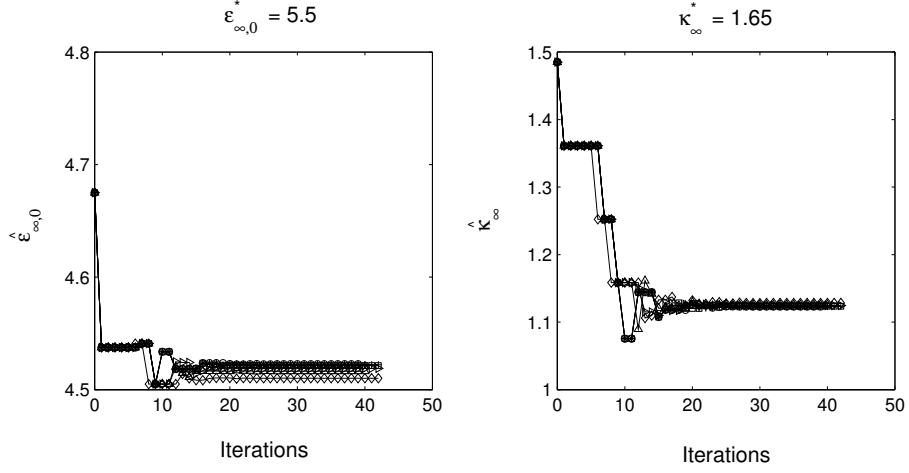
Figure 82: Variation in the estimates $\hat{\epsilon}_{\infty,0}$ (left) and $\hat{\kappa}_{\infty}$ (right) over all iterations in the Nelder-Mead algorithm for varying levels (ν) of constant variance noise added to the data as tabulated in Table 26.

Table 26: Parameter estimation of $\epsilon_{\infty,0}$ and κ_{∞} for varying levels of constant variance noise corresponding to 0%-10% relative noise.

% RN	Iter	$\hat{\epsilon}_{\infty,0}$	$\hat{\kappa}_{\infty}$	$|J_{n+1}^S - J_0^S|$	J^S	$||\nabla J^S||_{L^2}$	FC
0.1	39	4.5226	1.1231	8.5551×10^{-9}	113.3545	0.0551	79
0.3	40	4.5224	1.1232	3.6791×10^{-9}	114.9105	0.0440	81
0.5	42	4.5221	1.1233	1.6051×10^{-9}	118.6662	0.0209	85
1.0	42	4.5215	1.1236	8.8755×10^{-9}	137.6788	0.0610	83
3.0	42	4.5189	1.1246	5.7953×10^{-9}	351.2076	0.0154	83
5.0	40	4.5164	1.1257	9.4709×10^{-9}	784.7016	0.0439	79
10.0	42	4.5102	1.1284	3.7162×10^{-9}	2830.7864	0.0448	86

108

Table 27: Confidence Intervals for the parameter estimation of $\epsilon_{\infty,0}$ and κ_∞ with the Nelder-Mead algorithm for varying levels of constant variance noise corresponding to 0%-10% relative noise.

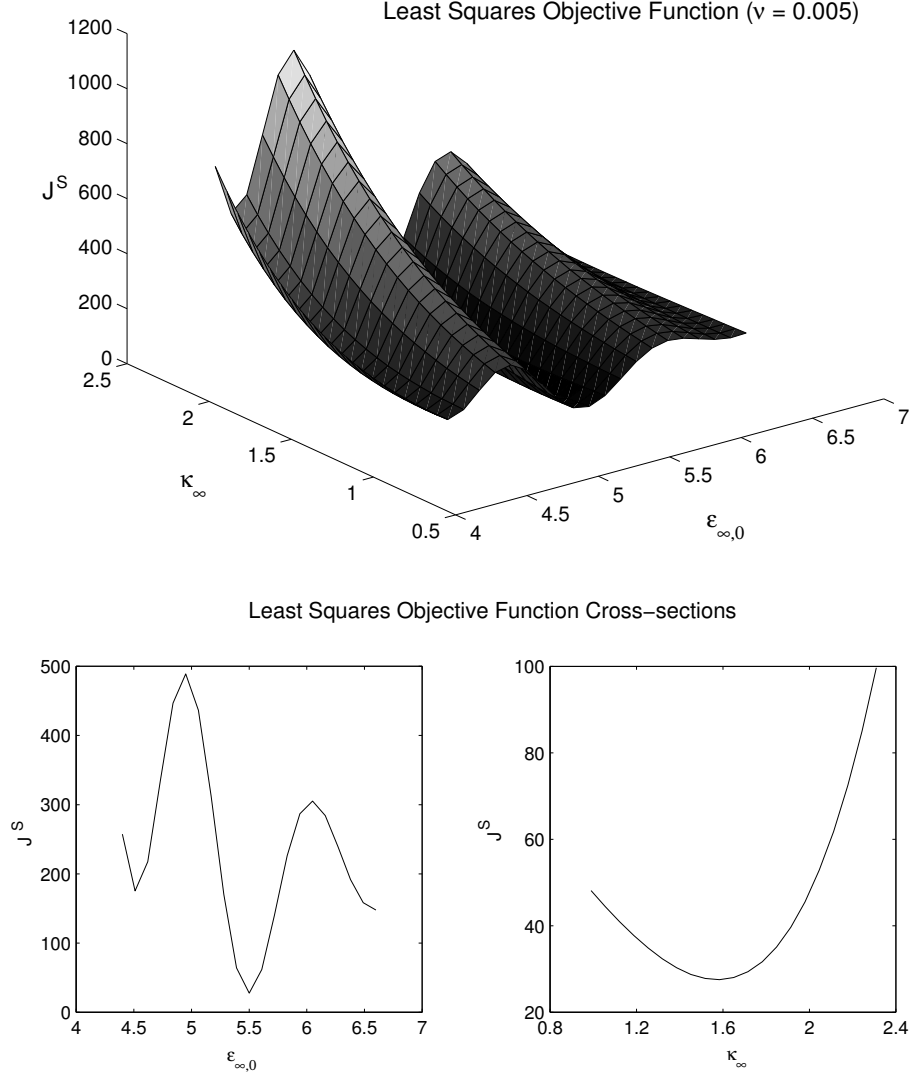|	RN = 0.1%
$\hat{\epsilon}_{\infty,0}$	$4.5226 \pm 7.6273 \times 10^{-3}$
$\hat{\kappa}_\infty$	$1.1231 \pm 4.7312 \times 10^{-2}$
	RN = 0.3%
$\hat{\epsilon}_{\infty,0}$	$4.5224 \pm 7.6781 \times 10^{-3}$
$\hat{\kappa}_\infty$	$1.1232 \pm 4.7624 \times 10^{-2}$
	RN = 0.5%
$\hat{\epsilon}_{\infty,0}$	$4.5221 \pm 7.8008 \times 10^{-3}$
$\hat{\kappa}_\infty$	$1.1233 \pm 4.8383 \times 10^{-2}$
	RN = 1.0%
$\hat{\epsilon}_{\infty,0}$	$4.5215 \pm 8.3986 \times 10^{-3}$
$\hat{\kappa}_\infty$	$1.1236 \pm 5.2073 \times 10^{-2}$
	RN = 3.0%
$\hat{\epsilon}_{\infty,0}$	$4.5189 \pm 1.3385 \times 10^{-2}$
$\hat{\kappa}_\infty$	$1.1246 \pm 8.2935 \times 10^{-2}$
	RN = 5.0%
$\hat{\epsilon}_{\infty,0}$	$4.5164 \pm 1.9965 \times 10^{-2}$
$\hat{\kappa}_\infty$	$1.1257 \pm 1.2361 \times 10^{-1}$
	RN = 10.0%
$\hat{\epsilon}_{\infty,0}$	$4.5102 \pm 3.7722 \times 10^{-2}$
$\hat{\kappa}_\infty$	$1.1284 \pm 2.3306 \times 10^{-1}$

Figure 83: (Top) The Least Squares Objective Function for different values of $\epsilon_{\infty,0}$ and κ_∞ for constant variance noise with $\nu = 0.005$ (1% RN)added to the data. The other five parameters were fixed at values given in (116), and (117). The minimum is located at the point $(5.5, 1.584)$, with a minimum value of 27.5152. However, we note the presence of a local minimum at the point $(4.51, 1.122)$ with a minimum least squares value of 138.0849. (Bottom) Cross sections of the Least Squares Objective function versus κ_∞ (right) and versus $\epsilon_{\infty,0}$ (left).
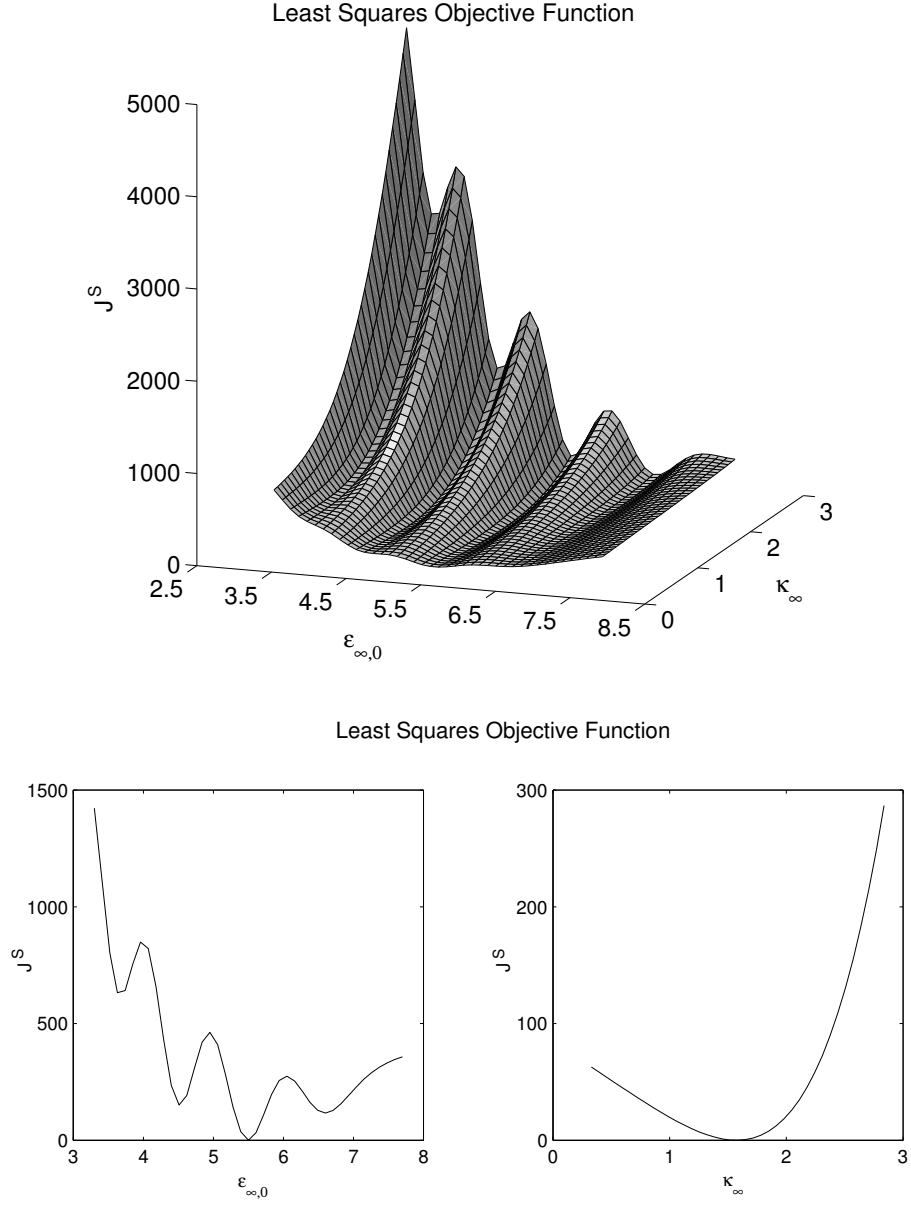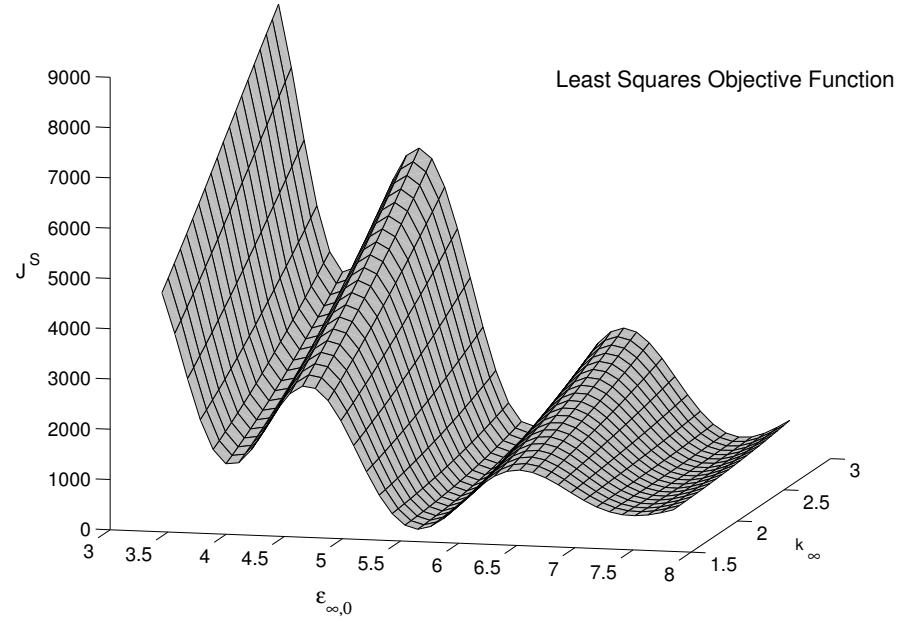
Figure 84: (Top) The Least Squares Objective Function for different values of $\epsilon_{\infty,0}$ and κ_∞ with no noise added to the data. The other five parameters were fixed at values given in (116), and (117), and τ_0 fixed at the value in (118). The minimum is located at the point $(5.5, 1.58)$, with a minimum value of 0.036. However, we note the presence of many local minimum. (Bottom) Cross Sections of the Least Squares Objective function versus κ_∞ (right) and versus $\epsilon_{\infty,0}$ (left).
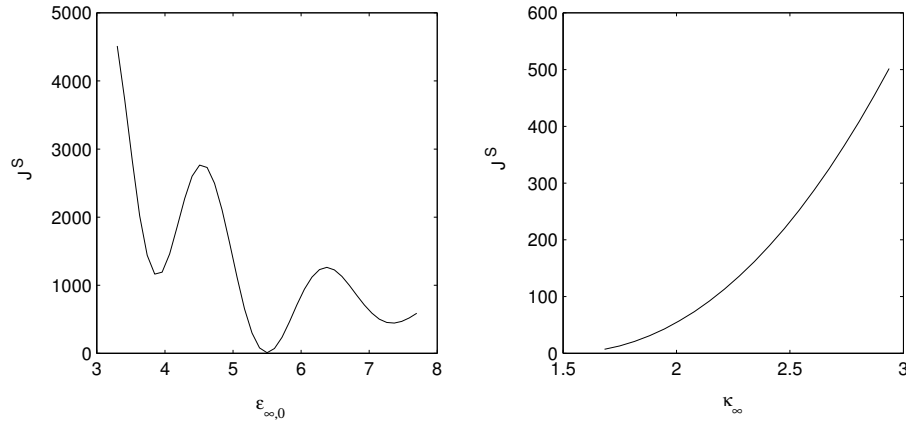
Figure 85: (Top) The Least Squares Objective Function for different values of $\epsilon_{\infty,0}$ and κ_∞ with no noise added to the data. The other five parameters were fixed at values given in (116), and (117). However the electromagnetic input source had a center frequency of 3.0 GHz as opposed to 5.0 GHz. The minimum is located at the point $(5.5, 1.683)$, with a minimum value of 6.91. We again note the presence of local minimum. (Bottom) Cross sections of the Least Squares Objective function versus κ_∞ (right) and versus $\epsilon_{\infty,0}$ (left).

Table 28: Parameter estimation of $\epsilon_{s,0}$, τ_0, and κ_s for 0%, 1%, 3% and 5% constant variance noise (test 2).

% RN	Iter	$\hat{\epsilon}_{\infty,0}$	$\hat{\tau}_0(\times 10^{-8})$	$\hat{\kappa}_\infty$
0.0	135	4.5306	1.3561	1.6470
0.1	120	4.5306	1.3475	1.6559
0.3	124	4.5301	1.3574	1.6479
0.5	122	4.5300	1.3875	1.6267
1.0	126	4.5283	1.4698	1.5787
3.0	118	4.5234	1.7950	1.4231
5.0	125	4.5185	2.4188	1.2588

Table 29: Parameter estimation of $\epsilon_{s,0}$, τ_0, and κ_s for 0%, 1%, 3% and 5% constant variance noise (test 2).

% RN	Iter	$|J_{n+1}^S - J_0^S|$	J^S	$||\nabla J^S||_{L^2}$	FC
0.0	135	7.3419×10^{-9}	112.2835	0.0281	244
0.1	120	5.7082×10^{-9}	112.2681	0.0355	216
0.3	124	6.8767×10^{-9}	113.8858	0.0023	226
0.5	122	2.4453×10^{-9}	117.7016	0.0287	217
1.0	126	8.1947×10^{-9}	136.8571	0.0159	225
3.0	118	9.0603×10^{-9}	350.8494	0.0205	206
5.0	125	4.3675×10^{-9}	784.6225	0.0296	231

coefficient κ_∞ again by adding constant variance noise to our data. The other four parameters are fixed at the values given in (116), and (117). Table 28 displays the results of the inverse problem. Again we note that the Nelder-Mead converges to a local minima.Figures 86, 87, 88 and 89 plot the details of the Nelder-Mead algorithm and the variation of the parameters with the iteration count. In Table 30 we calculate the confidence intervals for the three parameter estimation problem. Again we observe that the intervals are larger as compared with the results of the Levenberg-Marquardt method.

8   Conclusions and future directions

In this report we have presented an electromagnetic interrogation technique for identifying dielectric parameters of a Debye medium by using acoustic pressure waves

Table 30: Confidence Intervals for the parameter estimation of $\epsilon_{\infty,0}$, τ_0 and κ_∞ for constant variance noise with the Nelder-Mead algorithm.

|	RN = 0.0%
$\hat{\epsilon}_{\infty,0}$	$4.5306 \pm 8.2512 \times 10^{-3}$
$\hat{\tau}_0$	$(1.3561 \pm 5.9711 \times 10^{-1}) \times 10^{-8}$
$\hat{\kappa}_\infty$	$1.6470 \pm 1.9556 \times 10^{-1}$
	RN = 0.1%
$\hat{\epsilon}_{\infty,0}$	$4.5306 \pm 8.2283 \times 10^{-3}$
$\hat{\tau}_0$	$(1.3475 \pm 5.9323 \times 10^{-1}) \times 10^{-8}$
$\hat{\kappa}_\infty$	$1.6559 \pm 1.9523 \times 10^{-1}$
	RN = 0.3%
$\hat{\epsilon}_{\infty,0}$	$4.5301 \pm 8.2937 \times 10^{-3}$
$\hat{\tau}_0$	$(1.3574 \pm 6.0170 \times 10^{-1}) \times 10^{-8}$
$\hat{\kappa}_\infty$	$1.6479 \pm 1.9682 \times 10^{-1}$
	RN = 0.5%
$\hat{\epsilon}_{\infty,0}$	$4.5300 \pm 8.4345 \times 10^{-3}$
$\hat{\tau}_0$	$(1.3875 \pm 6.2477 \times 10^{-1}) \times 10^{-8}$
$\hat{\kappa}_\infty$	$1.6267 \pm 2.0063 \times 10^{-1}$
	RN = 1.0%
$\hat{\epsilon}_{\infty,0}$	$4.5283 \pm 9.0550 \times 10^{-3}$
$\hat{\tau}_0$	$(1.4698 \pm 7.1148 \times 10^{-8}) \times 10^{-8}$
$\hat{\kappa}_\infty$	$1.5787 \pm 2.1736 \times 10^{-1}$
	RN = 3.0%
$\hat{\epsilon}_{\infty,0}$	$4.5234 \pm 1.4519 \times 10^{-2}$
$\hat{\tau}_0$	$(1.7950 \pm 1.3804) \times 10^{-8}$
$\hat{\kappa}_\infty$	$1.4231 \pm 3.5550 \times 10^{-1}$
	RN = 5.0%
$\hat{\epsilon}_{\infty,0}$	$4.5185 \pm 2.1562 \times 10^{-2}$
$\hat{\tau}_0$	$(2.4188 \pm 2.7552) \times 10^{-8}$
$\hat{\kappa}_\infty$	$1.2588 \pm 5.4570 \times 10^{-1}$
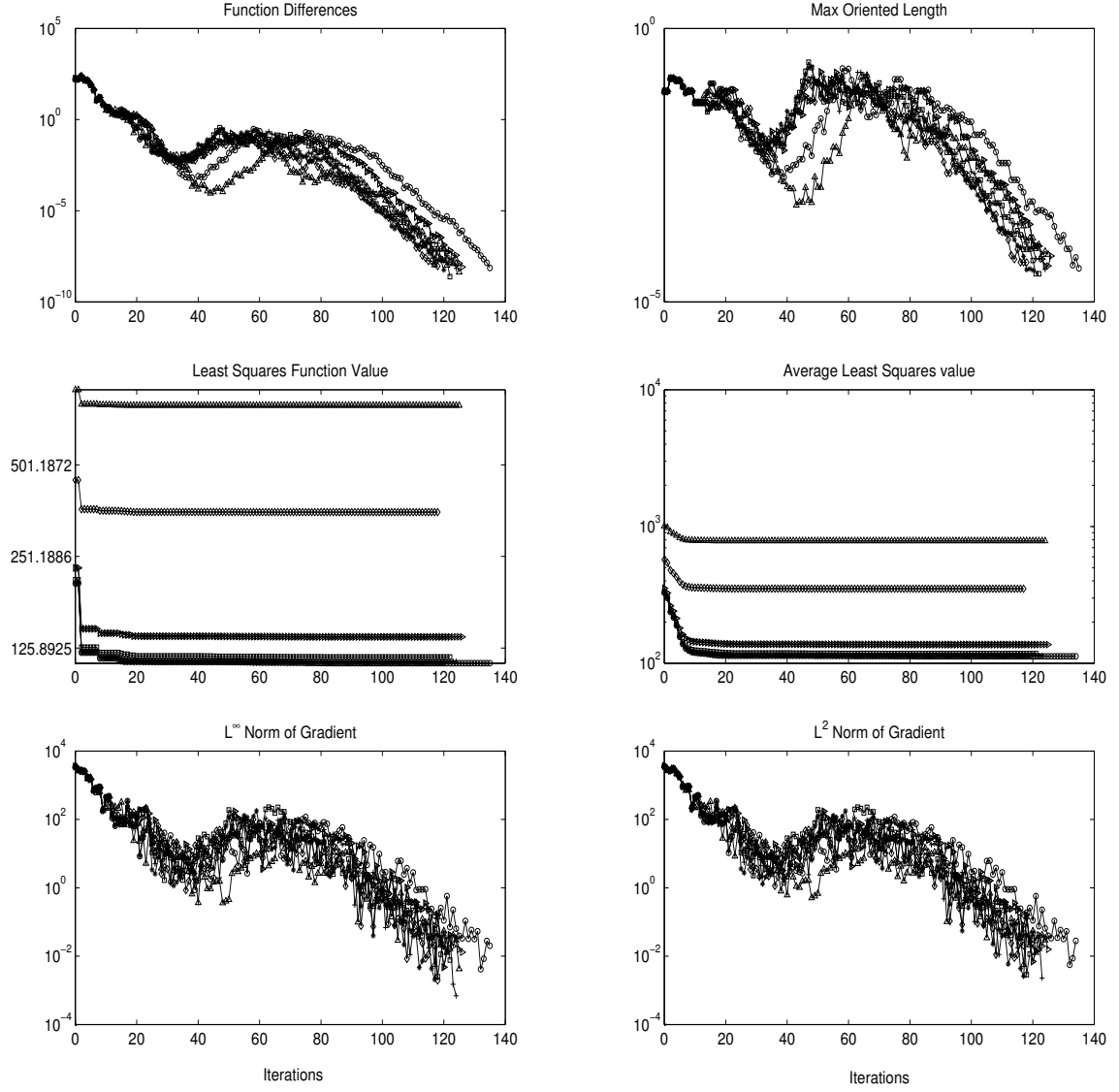
Figure 86: Details of the Nelder-Mead algorithms for the three parameter estimation of $\epsilon_{\infty,0}$, τ_0 and κ_∞ with varying levels (ν) of constant variance noise added to the data as tabulated in Table 28, and 29.
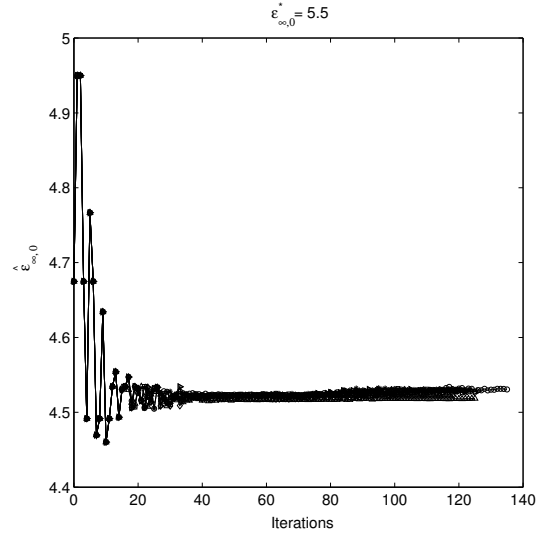
Figure 87: Variation in the estimate $\hat{\epsilon}_{\infty,0}$ over all iterations in the Nelder-Mead algorithm for varying levels (ν) of constant variance noise added to the data as tabulated in Table 28, and 29.
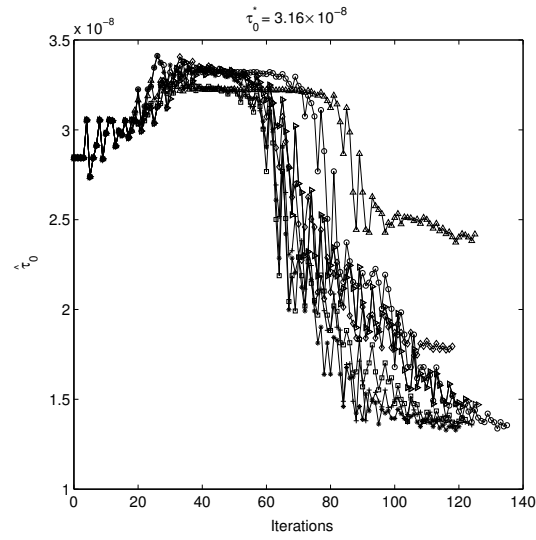

Figure 88: Variation in the estimate $\hat{\tau}_0$ over all iterations in the Nelder-Mead algorithm for varying levels (ν) of constant variance noise added to the data as tabulated in Table 28, and 29.

Figure 89: Variation in the estimate $\hat{\kappa}_\infty$ over all iterations in the Nelder-Mead algorithm for varying levels (ν) of constant variance noise added to the data as tabulated in Table 28, and 29.
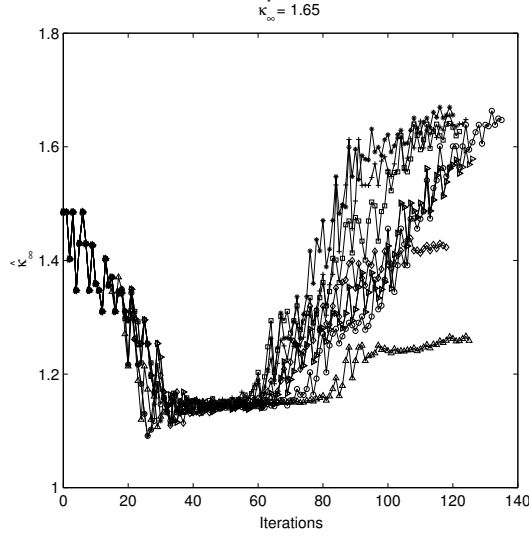
as virtual reflectors for the incident electromagnetic pulse. We considered the two dimensional TE mode of Maxwell's equations which incorporates the pressure dependence in the Debye medium via a model for orientational polarization. As a first approximation we assumed that the dielectric parameters $\epsilon_{s,0}$, $\epsilon_{\infty,0}$ and the relaxation τ_0 are affine functions of pressure. We have used the finite difference time domain scheme to discretize our electromagnetic/acoustic model and to compute simulated data to be used in a parameter identification problem.

We formulated an inverse problem for the identification of the material parameters as well as the coefficients of pressure in the Debye model, based on the method of least squares. We used two different methods to solve the inverse problem; namely Levenberg-Marquardt and Nelder-Mead. The inverse problem indicates that the coefficients that can be identified depend on the order of magnitude of $\omega\tau_0$. Thus in the first test problem we were able to identify $\epsilon_{s,0}$ and the corresponding pressure coefficient κ_s, and in the second test problem we were able to identify $\epsilon_{\infty,0}$ and the corresponding pressure coefficient κ_∞. It is not possible to accurately identify all the seven parameters that describe the Debye medium coupled with the model for pressure dependence in either of the examples that we have considered in this report.

We have also computed confidence intervals for all the estimates obtained using statistical error analysis based on the assumption of constant variance noise. We showed that the intervals become larger as the level of added noise is increased.

117

There are many questions that still need to be answered. We have used a simple linear model for the pressure term in Maxwell's equations. Also we have assumed that the effect of the electromagnetic field on the acoustic wave is negligible. A dynamic coupled model of the electromagnetic/acoustic interaction is the topic of a future paper. We will also consider the dielectric parameters to be nonlinear functions of pressure in a future paper to determine if the dynamics of the problem change with the dependence of the dielectric parameters on the pressure.

9   Acknowledgements

References

[ABK04]   R. Albanese, H. T. Banks, and G. M. Kepler. Experimental results involving acousto-optical interactions. Technical Report In preparation, CRSC, North Carolina State University, 2004.

[ABR02]   R. A. Albanese, H. T. Banks, and J. K. Raye. Nondestructive evaluation of materials usig pulsed microwave interrogating signals and acoustic wave induced reflections. *Inverse Problems*, 18:1935–1958, 2002.

[AMP94]   R. A. Albanese, R. L. Medina, and J. W. Penn. Mathematics, medicine and microwaves. *Inverse Problems*, 10:995–1007, 1994.

[And67]   J. C. Anderson. *Dielectrics*. Chapman and Hall LTD and Science Paperbacks, 1967.

[APM89]   R. A. Albanese, J. W. Penn, and R. L. Medina. Short-rise-time microwave pulse propagation through dispersive biological media. *J. Optical Society of America A*, 6:1441–1446, 1989.

[BB99]   H. T. Banks and K. L. Bihari. Modeling and estimating uncertainty in parameter estimation. Technical Report CRSC-TR99-40, CRSC, North Carolina State University; Inverse Problems 17: 95-111, 2001, December 1999.

[BB03]   H. T. Banks and J. M. Bardsley. Parameter identification for a dispersive dielectric in 2d electromagnetics: Forward and inverse methodology with

statistical considerations. *CRSC-TR03-48, December 2003; Intl. J. Comp. and Num. Anal. and Applic., to appear*, 2003.

[BBL00] H. T. Banks, M. W. Buksas, and T. Lin. *Electromagnetic Material Interrogation Using Conductive Interfaces and Acoustic Wavefronts*. Frontiers in Applied Mathematics. SIAM, Philadelphia, PA, 2000.

[Ber94] J. P. Berenger. A perfectly matched layer for the absorption of electromagnetic waves. *J. Comput. Phys.*, 114(2):185–200, 1994.

[BF95] J. G. Blaschak and J. Franzen. Precursor propagation in dispersive media from short-rise-time pulses at oblique incidence. *J. Optical Society of America A*, 12:1501–1512, 1995.

[BG04] H. T. Banks and N. L. Gibson. Well-posedness in maxwell systems with distributions of polarization relaxation parameters. Technical Report CRSC-TR04-01, CRSC, North Carolina State University; Applied Math. Letters, to appear, 2004.

[BGW03] H. T. Banks, N. L. Gibson, and W. P. Winfree. Electromagnetic crack detection inverse problems using terahertz interrogating propagating signals. Technical Report CRSC-TR03-40, CRSC, North Carolina State University, October 2003.

[BK89] H. T. Banks and K. Kunisch. *Estimation Techniques for Distributed Parameter Systems*. Birkhauser, Boston, 1989.

[Bri60] L. Brillouin. *Wave Propagation and Group Velocity*. Pure Appl. Phys. Academic Press, New York and London, 1960.

[DG95] M. Davidian and D. M. Giltinan. *Nonlinear Models for Repeated Measurement Data*, volume 62 of *Monographs on Statistics and Applied probability*. Chapman and Hall, New York, 1995.

[FMS03] E. C. Fear, P. M. Meaney, and M. A. Stuchly. Microwaves for breast cancer detection. *IEEE Potentials*, pages 12–18, 2003.

[Ged96] S. D. Gedney. An anisotropic perfectly matched layer absorbing media for the truncation of FDTD lattices. *IEEE Trans. Antennas Propagat.*, 44(12):1630–1639, 1996.

[Jac99] J. D. Jackson. *Classical Electromagnetics*. John Wiley and Sons, 1999.

[JN84] N. S. Jayant and P. Noll. *Digital Coding of Waveforms*. Prentice Hall, Englewoods Cliffs, 1984.

[Kel99]   C. T. Kelley. *Iterative Methods for Optimization.* Frontiers in Applied Mathematics. SIAM, Philadelphia, PA, 1999.

[Kor97]   A. Korpel. *Acosto-Optics.* Marcel-Dekker, New York, 2nd edition, 1997.

[MI68]   P. Morse and K. Ingard. *Theoretical Acoustics.* McGraw-Hill, 1968.

[MP95]   R. Mittra and U. Pekel. A new look at the perfectly matched layer (PML) concept for the reflectionless absorption of electromagnetic waves. *IEEE Microwave Guided Wave Lett.*, 5(3):84–86, 1995.

[Pet94]   P. Petropoulos. Stability and phase error analysis of FD-TD in dispersive dielectrics. *IEEE Trans. Antennas Propagat.*, 42(1):62–69, 1994.

[Rap95]   C. M. Rappaport. Perfectly matched absorbing boundary conditions based on anisotropic lossy mapping of space. *IEEE Microwave Guided Wave Lett.*, 5(3):90–92, 1995.

[SKLL95]   Z. S. Sacks, D. M. Kinsland, R. Lee, and J. F. Lee. A perfectly matched anisotropic absorber for use as an absorbing boundary condition. *IEEE Trans. Antennas Propagat.*, 43:1460–1463, 1995.

[Taf95]   A. Taflove. *Computational Electrodynamics: The Finite-Difference Time-Domain method.* Artech House, Norwood, MA, 1995.

[Taf98]   A. Taflove. *Advances in Computational Electrodynamics: The Finite-Difference Time-Domain method.* Artech House, Norwood, MA, 1998.